

Battery Management and Battery Modeling Considerations for Application in a Neighborhood Electric Vehicle

By

Matthew Choate
B.Sc., University of Kansas, 2014

Submitted to the graduate degree program in the Department of Mechanical Engineering and the
Graduate Faculty of the University of Kansas in partial fulfillment of the requirements for the
degree of Master of Science.

Chair: Dr. Christopher Depcik

Member: Dr. Huazhen Fang

Member: Dr. Lin Liu

Date Defended: September 24, 2019

The thesis committee for Matthew Choate certifies that this is the approved version of the
following thesis:

**Battery Management and Battery Modeling Considerations for
Application in a Neighborhood Electric Vehicle**

Chair: Dr. Christopher Depcik

Date Approved: September 27, 2019

Abstract

Transitioning from internal combustion engine vehicles (ICEVs) to electric vehicles (EVs) consolidates and relocates emissions, endeavoring to improve air quality, particularly in high traffic urban areas. Unfortunately, many obstacles to widespread EV use remain, broadly related to user familiarity, convenience, and effectiveness. However, EVs are better suited for some opportunities. Following the introduction, this thesis covers the process of upgrading a neighborhood electric vehicle (NEV) from lead-acid batteries to a swappable battery pack consisting of lithium iron phosphate (LiFePO_4), or LFP, cells. Although LFP cells are considered safer than other lithium-ion cells, a new battery charger and battery management system (BMS) were installed to ensure proper function and maintenance. While the new electronics appeared to be successfully integrated during initial testing, several cells within the battery pack were over-discharged—or underwent voltage reversal—while outside during winter. Thus, prompted a reassessment of battery management practices and implementation, resulting in the construction of a new battery pack and redesign of the charge and discharge controls.

The ensuing chapter pertains to battery management practices employed in the vehicle—and battery management in general. This chapter begins with background, wherein discusses fundamentals of cell function, modes of failure, and lastly, methods of obviating failure and protracting cell longevity. Finally, chapter four describes battery modeling from the perspective of a tool to maintain cells in EVs. Determination of immeasurable states that are important to battery management and consumer comfort are deliberated. Mathematical models and equivalent circuit models of cell behavior are of particular interest. Common equivalent circuit models are parameterized for several cells and voltage estimation capabilities are compared.

Acknowledgments

Thank you to my family and friends who supported me along the way; you are my everything. Thank you to Dr. Christopher Depcik for your guidance, patience, and all the help you have provided. Similarly, thank you to my professors and colleagues at KU. Khalaf and Shah, your help and advice have been crucial. Additionally, I would like to thank KU Facility Services for their hard work and KU Center for Sustainability for providing this opportunity. Finally, thank you to my doctor and my therapist.

Table of Contents

Abstract	iii
Acknowledgments.....	iv
Table of Contents	v
Table of Figures	x
Table of Tables:	xix
Nomenclature:.....	xxi
1 Introduction.....	1
1.1 Background	1
1.2 Similar/Previous Work.....	3
1.3 Brief Look at Chapters	3
2 Updating and Fixing the GEM.....	6
2.1 Abstract	6
2.2 Introduction	7
2.3 Vehicle History and Purpose.....	9
2.4 Electric Vehicle Modeling	11

2.5	Initial Upgrade of GEM to LFP Battery Pack.....	14
2.5.1	Initial 40 Ah Lithium-Ion Battery Pack.....	14
2.5.2	Physical Changes to GEM/Construction	18
2.5.3	Extant Electrical System.....	22
2.5.4	System Specifications	24
2.5.5	Electrical Components	25
2.5.6	Battery Management System	32
2.5.7	Choosing a Charger.....	37
2.5.8	BMS Controls and Communications	39
2.6	Repairs and Battery Management Round Two	45
2.6.1	Discerning Problem	45
2.6.2	Second 60 Ah Lithium-Ion Battery Pack.....	46
2.6.3	Troubleshooting	57
2.6.4	BMS Vehicle Control	72
2.6.5	BMS Charger Control	75
2.7	Recommendations & Discussion	77

2.8	Conclusion.....	77
3	Battery Management.....	79
3.1	Abstract	79
3.2	Introduction	80
3.3	Getting to Know Batteries.....	81
3.3.1	Parts of a Battery.....	81
3.3.2	Simplified Battery Function.....	86
3.3.3	Battery Issues	91
3.3.4	Basics of Battery Care	96
3.4	GEM BMS.....	109
3.4.1	Programming the BMS	111
3.5	Discussion	133
3.6	Conclusion.....	134
4	Battery Modeling for Electric Vehicles	136
4.1	Abstract	136
4.2	Introduction	138

4.3	Battery Evaluation Considerations	139
4.3.1	Illustrating Dynamic Behavior.....	141
4.4	Battery Modeling.....	150
4.4.1	Coulomb Counting.....	150
4.4.2	Data-Based Empirical Methods	152
4.4.3	Peukert's Law	153
4.4.4	OCV-SOC Relationships	154
4.4.5	Equivalent Circuit Models (ECMs)	158
4.5	Continuing Mathematical Models.....	170
4.5.1	Voltage Hysteresis	170
4.5.2	Determination of Other States	172
4.5.3	Methods.....	173
4.5.4	Linear Least Squares Regression of R_{int} with Combined OCV-SOC Relationship	
	175	
4.5.5	Iterative Parameterization Using MATLAB function <i>fmincon</i>	176
4.5.6	Modeling Results	177

4.6	Conclusion.....	186
5	Conclusion	188
	Appendix.....	192
	References.....	198

Table of Figures

Figure 1: Battery box for the 40 Ah batteries.	17
Figure 2: Frame weldment for 2007 GEM 2 passenger vehicles [12]. Highlighted regions in yellow show where the lead-acid batteries were originally placed. The arrow points towards the front of the vehicle.	19
Figure 3: Small utility bed assembly drawing for the 2007 GEM eS [12]. Visible regions of the two C-channel supports are shaded yellow. An object supported by the two C-channels cannot extend any further under the vehicle than the two hex bolts, circled in red. Forward direction of the vehicle is signified by the large black triangle.....	20
Figure 4: Simplified CAD portrayal of the cargo carrier and features significant to mounting the battery drawer [14]. Aluminum L-beams, highlighted in yellow, were added to the vehicle. Red arrows point towards the three bolts that prevent mounting the sliders on the C-channels.....	21
Figure 5: PSDM connector locations [22].	25
Figure 6: Beige colored version of the motor controller installed in the 2007 GEM eS [13].	27
Figure 7: Instrument pod with features enumerated and labeled [11].	29
Figure 8: LCD indicators are itemized and shown where they appear when the vehicle is in use [11]......	30
Figure 9: : Original Orion BMS [29].	32
Figure 10: Orion BMS Main I/O Connector pinout with wire color and function indicated [29].	33

Figure 11: BMS cell group connector diagram with pins labeled according to the associated battery terminals [29].	34
Figure 12: Pinout of the pack voltage sensor connector that links to the BMS [29].	35
Figure 13: BMS current sensor and thermistor connector [29].	36
Figure 14: Diagram depicting 120 Ω resistors terminating the CAN bus and how multiple devices on the bus act as nodes [29].	40
Figure 15: Wiring the BMS CAN1 to a DB9 connector to enable proper function of the CANdapter [29].	41
Figure 16: Modified start switch circuit shown. By pulling the Discharge Enable signal to ground, the BMS can close the start switch circuit, thus, when the accelerator is pressed, the EMC receives power for the electric motor.	43
Figure 17: Revised start switch circuit installed in the GEM by Patrick Collins [7].	44
Figure 18: Four 60 Ah GBS batteries strapped together with aluminum plates at either end and three aluminum straps on either side. Purple caps impede the ingress of dust and water droplets, but also prevent foreign objects from falling between terminals and causing a short circuit.	47
Figure 19: Two cell configurations considered for the steel battery box. Left configuration was ultimately chosen. Busbar connections are represented by the dotted rectangles. Connector between cells 11 and 12 on the left, and 10 and 11 on the right would need to be fabricated in-house.	49

Figure 20: Steel battery box for the 60 Ah batteries.	50
Figure 21: Prototype diagonal busbar cut from aluminum.	52
Figure 22: Aluminum battery box.....	53
Figure 23: Cell configuration for the aluminum battery box. Busbar connections are again represented by the dotted rectangles.	54
Figure 24: Third iteration of the 60 Ah battery box, constructed of wood. Batteries were not yet connected for this photo.	55
Figure 25: Cell configuration for the wood battery box. Each column (i.e., cells 1, 22, 23, and 24) are pressed together by aluminum plates and straps. Thus, no individual cell can be removed, but must instead be removed as part of a four-cell unit.	56
Figure 26: Heavy duty power connectors and circular connector attached to the battery pack. Uncoupled heavy duty power connector is for the charger while the coupled heavy-duty power connector links the battery pack to the vehicle. The black connector in the bottom left is the circular connector for the BMS cell voltage taps.....	57
Figure 27: Standard drawing for original motor controller connections in NEV applications. [13]	62
Figure 28: Photo juxtaposing the BATT- PSDM post to the remaining segment of the 72 GND post after snapping.	63

Figure 29: Photograph from within the PSDM of the 72 GND (left) and BATT- (right) posts after installing the new 72 GND post. Neither post may be safely removed from the PSDM, though, the extant zinc base was sufficiently wide enough to support a new zinc rod.....	65
Figure 30: External view of the 72 GND post after repairs were made. The bolt is a different size than the original. Damage to the plastic resulting from attempts to solder the coupling nut are visible around the post. Marks from clipping the metal extend radially from the post.	66
Figure 31: Layout and labels of pins on the bottom of the RECOM DC/DC converter [34]	74
Figure 32: Crydom SSR suggested wiring diagram including diode suppression of the load [35].	74
Figure 33: Terminal arrangement of the Omron DPDT relay.	76
Figure 34: Molecular structure of two contrasting negative electrode materials in lithium-ion batteries [17].	83
Figure 35: Crystal structures of different lithium-ion positive electrodes. LiCoO_2 (LCO) is the layered structure in (a). The spinel structure in (b) is that of LiMn_2O_4 . LFP in (c) is an example of an olivine crystal structure. Lastly, (d) is a favorite structure belonging to LiFeSO_4F (LFSF) [17]......	85
Figure 36: Reduction of operating voltage from open-circuit voltage due to ohmic, activation, and concentration polarizations [15]......	88

Figure 37: An example of a battery comprised of three parallel strings of three cells in series. The top and bottom series are limited to 1 Ah while the middle discharges 2 Ah for a total of 4 Ah from the battery.....	101
Figure 38: A battery configured as a series of three sets of three cells in parallel. Two of the parallel sets can only discharge 5 Ah; thus, the pack can only discharge 5 Ah.....	102
Figure 39: Photo of Elithion cell boards installed in a vehicle electrical conversion project [7].	103
Figure 40: Profile Setup Wizard pop-up. The selection of “Battery Type” does not include GBS 60Ahr so GBS 40Ahr was chosen and settings were corrected [48].	112
Figure 41: The “Profile Setup Wizard” includes a simplified setup of thermistors and relay outputs for controlling loads [48].	113
Figure 42: “Profile Setup Wizard” pop-up inquiring CANBUS settings and which third-party devices are enabled on the CANBUS [48].	114
Figure 43: “General Settings” tab of the “Battery Profile” page [48].	115
Figure 44: “Voltage Settings” are set in the “Cell Settings” tab. Voltage limits are enforced during charge and discharge to avoid damaging the cells but are not the only conditions influencing these decisions [48].....	117
Figure 45: BMS cell resistance settings tab with values used in the GEM profile [48].	120
Figure 46: SOC settings and SOC drift points used in the GEM profile [48].	121

Figure 47: CANBUS Settings tab of the BMS GEM profile [48].	123
Figure 48: GEM BMS profile Addon Settings tab and selections [48].	124
Figure 49: GEM BMS Charge Limits profile showing the Basic Limit Settings [48].	125
Figure 50: Default GEM BMS profile Charge Limits Failsafe settings after completing “Profile Setup Wizard [48].”	127
Figure 51: Basic discharge current limit (DCL) settings in the GEM BMS profile [48].	129
Figure 52: GEM BMS DCL Failsafe settings entered by the Profile Setup Wizard [48].	130
Figure 53: Charger Safety relay settings in the Orion BMS GEM profile [48].	132
Figure 54: Orion BMS Discharge Enable relay settings for the GEM [48].	133
Figure 55: Discharge curve of the GBS 60 Ah LFMP cells provided by AA Portable Power Corp [31]. The red line, which remains at a higher voltage for the majority of the discharge event, is at 0.5 C-rate. The black line, right below red, is at 1 C-rate. Lastly, the blue line is at 3 C-rate. ..	143
Figure 56: Discharge characteristics of a Panasonic 3200 mAh battery, model NCR18650B, at different temperatures [55]. The voltage decreases as the temperature decreases.	144
Figure 57: General procedure of an HPPC test [52].	145
Figure 58: HPPC discharge current sharing a plot with the SOC and terminal voltage response [56]. Voltage response is fin-shaped where the curves represent time-dependent cell processes.	146

Figure 59: The difference in OCV while charging and discharging is from hysteresis effects [57]. Since this is a complete cycle, this is a major hysteresis loop.	147
Figure 60: EIS Nyquist plot of a LFP cell at 20 °C and 50% SOC [62].....	148
Figure 61: Left—Nyquist plot of EIS measurements of a cell at 50% SOC and across a range of temperatures [63]. Right—Nyquist plot of EIS measurements of a cell at 10 °C and at various SOC.....	149
Figure 62: EIS plots of a discharged cell (top) and charged cell (bottom) at different cycles [64].	150
Figure 63: Ideal Battery ECM comprised of only a voltage source.	159
Figure 64: Internal resistance (R_{int}) ECM.	160
Figure 65: LFP cell voltage after single pulse discharge [76].	162
Figure 66: Voltage response to a discharge pulse. The LFP cell measured here is the same as in Figure 60. Typically, behavior occurring at frequencies lower than one hertz are mass transfer through diffusion [62].	163
Figure 67: Thévenin ECM highlighting the inclusion of a capacitor into the model.	164
Figure 68: Generalized Randles' ECM with one RC pair [66, 79].....	165
Figure 69: Randles equivalent circuit for electrode reactions [80].....	166
Figure 70: Example equivalent circuit for battery EIS data [82].....	166

Figure 71: Dual Polarization ECM showing the inclusion of a second resistor/capacitor pair [50, 83].	167
Figure 72: This resistance-capacitance (RC) ECM, developed by Saft and revised by NREL, uses capacitors to store charge in the cell [78, 83, 86].	169
Figure 73: Plot of battery data and model results for the A123 APR18650M1A cell when parameterized for the R_{int} and Combined OCV-SOC models using LLSR.	178
Figure 74: Battery data alongside R_{int} and combined OCV-SOC model results plot for the A123 M1B cell with an overall R_{SQ} of 4.71.	182
Figure 75: Battery data plotted alongside Thévenin and combined OCV-SOC model results for the A123 M1B cell with an overall R_{SQ} of 4.13.	183
Figure 76: Dual polarization and combined OCV-SOC with an R_{SQ} of 4.71 for the A123 M1B cell.....	183
Figure 77: Parking brake circuit diagram in the 2010 GEM Service Manual that better matches the GEM parking brake wiring than the service manual donated by KU Facilities Services.....	192
Figure 78: “Charger Safety Functional Flowchart” provided in the Orion BMS Utility Manual [29]. These are the steps taken to determine if the Charger Safety relay is engaged or disengaged.	193
Figure 79: “Discharge Enable Functional Flowchart” outlining the conditions that determine whether the BMS allows discharge [29].....	194

Figure 80: Original Randles equivalent circuit battery model representing electrode reactions. Resistance and capacitance of the electrode reaction are R_R and C_R , respectively. Resistance of the electrolyte is R_C and capacitance of double layer effect at the electrode surface is C_{DL} [80].	195
Figure 81 Equivalent circuit model utilized by the Partnership for a New Generation of Vehicles (PNGV) to predict terminal voltage [89]. Model parameters are to be found through Hybrid Pulse Power Characterization (HPPC) tests. The RC pair models polarizations, hence the subscripts.....	195
Figure 82 One variation of the PNGV ECM. The RC pair and other circuit components are in a different order compared to the original PNGV EMC in Figure 81 [83, 90].	196
Figure 83 This equivalent circuit model is named the General Non-Linear (GNL) model or otherwise known as an improved PNGV model [90, 91].	196

Table of Tables:

Table 1: List of wire color abbreviations and their corresponding colors.	23
Table 2: List of wire harness and their abbreviated names.....	23
Table 3: PSDM fuse description.	26
Table 4: SX Transistorized EMC NEV Application I/O List [13]. Pin 13 is N/A until changes made in Section 2.6.3.6.....	28
Table 5: Description of indicators itemized in Figure 8.	31
Table 6: ElCon PFC charger flashing sequence description.....	38
Table 7: ElCon PFC charger communications circular connector pinout.	38
Table 8: Cell models and corresponding characteristics [69].	175
Table 9: Parameters for R_{int} and combined models solved through linear least squares regression.	178
Table 10: Parameters for the R_{int} and combined models solved with MATLAB function fmincon.	179
Table 11: Cell parameters and coefficient of determination for the Thévenin and combined OCV- SOC.....	180
Table 12: Cell parameters and coefficient of determination for the DP and combined OCV-SOC.	180

Table 13: Total voltage error for each cell and model.....	184
--	-----

Table 14: Calibration results for the ANR M1B cell. The notation in the second row indicates if the parameters were constrained to be positive or if positive and negative values were allowed.	
---	--

.....	197
-------	-----

Nomenclature:

Abbreviation	Description
A	Ampere
AC	Alternating Current
Ah	Ampere Hour
AWG	American Wire Gauge
BATT	Battery
BDI	Battery Discharge Indicator
BEV	Battery Electric Vehicle
BFLS	Brake Fluid Level Switch
BK	Black
BMS	Battery Management System
BPS	Brake Pressure Switch
BR	Brown
BTS	Battery Temperature Sensor
CAD	Computer-Aided Design
CALB	China Aviation Lithium Battery
CAN	Controller Area Network
CCL	Charge Current Limit
CFR	Code of Federal Regulations
CH	Motor Controller Harness
CHMSL	Center High-Mount Stop Light
CSV	Comma Separated Value
DB	Dark Blue
DC	Direct Current
DCCH	DC/DC Converter Harness
DCL	Discharge Current Limit
DG	Dark Green
DH	Drive High
DL	Drive Low
DPST	Double Pole Single Throw
DTC	Diagnostic Trouble Code
ECM	Equivalent Circuit Model
ECU	Electronic Control Unit
EIS	Electrochemical Impedance Spectroscopy
EMC	Electric Motor Controller
EOL	End of Life
EV	Electric Vehicle

FAS	Fused and Switched
FH	Front Harness
FMVSS	Federal Motor Vehicle Safety Standards
GE	General Electric
GEM	Global Electric Motorcar
GFCI	Ground-Fault Circuit Interrupter
GND	Ground
GVWR	Gross Vehicle Weight Rating
GY	Gray
HEV	Hybrid Electric Vehicle
HH	Headlight Harness
hp	Horsepower
HV	High Voltage
Hz	Hertz
I/O	Input/Output
ICEV	Internal Combustine Engine Vehicle
ID	Identification number
IP	Instrument Panel
IP46	Ingress Protection against wires/screws and water jets
IPH	Instrument Panel Harness
IR	Current-Resistance, voltage drop due to resistance
kbps	Kilobits Per Second
kg	Kilogram
KU	University of Kansas
LB	Light Blue
lbs.	Pounds
LCD	Liquid Crystal Display
LCO	Lithium Cobalt Oxide
LFMP	Lithium Iron Manganese Phosphate
LFP	Lithium Iron Phosphate
LG	Light Green
LiCoO ₂	Lithium Cobalt Oxide
LiFeMnPO ₄	Lithium Iron Manganese Phosphate
LiFePO ₄	Lithium Iron Phosphate
Li-ion	Lithium ion
LiNiCoAlO ₂	Lithium Nickel Cobalt Aluminum Oxide
LSV	Low-Speed Vehicle
MDS	Master Disconnect Switch

mm	Millimeter
mph	Miles Per Hour
MPI	Multi-Purpose Input
MPO	Multi-Purpose Output
MTS	Motor Temperature Switch
NC	Normally Closed
NCA	Lithium Nickel Cobalt Aluminum Oxide
NEG	Negative
NEV	Neighborhood Electric Vehicle
NHTSA	National Highway Traffic Safety Administration
NiCd	Nickel-Cadmium
NiMH	Nickel-Metal Hydride
NO	Normally Open
OBD2	On-Board Diagnostics II
OCV	Open Circuit Voltage
OR	Orange
P/N	Part Number
PC	Propylene Carbonate
PCB	Printed Circuit Board
PFC	Power Factor Controlled
PHEV	Parallel Hybrid Electric Vehicle
PK	Pink
PNGV	Partnership for a New Generation of Vehicles
POS	Positive
Pot	Potentiometer
PSDM	Power Signal Distribution Module
PWM	Pulse-Width Modulated
RC	Resistance-Capacitance
RD	Red
Redox	Reduction/Oxidation
RH	Rear Harness
R_{int}	Internal Resistance
RPM	Revolutions Per Minute
SEI	Solid-Electrolyte Interface
SHE	Standard Hydrogen Electrode
SOC	State of Charge
SOF	State of Function
SOH	State of Health

SOP	State of Power
SPST	Single Pole Single Throw
TN	Tan
USB	Universal Serial Bus
VAC	Alternating Current Voltage
VDC	Direct Current Voltage
VIN	Vehicle Identification Number
VOC	Open Circuit Voltage
VRLA	Valve Regulated Lead-Acid
VT	Violet
Wh	Watt-hour
WT	White
YL	Yellow

1 Introduction

1.1 Background

Battery-powered electronics are ubiquitous; diverse modes of electricity production and versatile application of electricity promote global electrification. Storing electricity is necessary, lest the energy be wasted, whether still connected to the grid or off the grid. Electrical storage devices are requisite for mobile applications, like electronics, but also utilized in larger applications like electric vehicles (EVs). Electric vehicles are reemerging in prominence as a result of mounting fears of exhausting fossil fuels and the growing public consciousness of the numerous health and environmental issues associated with emissions. Reduced air quality and smog, resulting from heavy use of internal combustion engine vehicles (ICEVs)—and often worsened by low efficiency standards—has pressured some cities and regions to greatly limit the use of such vehicles [1]. Historically, when necessitated either by federal legislation calling for lower vehicle emissions or increasing market pressure from growing environmental awareness and rising fuel costs, the automotive industry has reengaged in efforts to improve efficiency and reduce emissions [2]. Besides prohibiting ICEVs, some governments, such as the United States federal government, have offered financial incentives in an attempt to increase EV sales and develop alternatives [3]. Consumers cite a number of factors that make EVs less appealing: upfront cost, lack of familiarity with EVs, inadequate infrastructure, and reduced range [3]. The majority of issues with EVs concerns their batteries.

Development in the promotion of EVs has included changing marketing strategies. Meanwhile, charging stations are slowly being installed nationwide and fast charging options have become

available for homes [4]. While the majority of driving trips in the United States are well within the range of many prominent EVs and many people seldom need access to vehicles with extensive range, the possibility that a vehicle owner may need that extended range also keeps people from buying EVs [3]. Technological developments revolve around the battery pack: increasing specific energy [Wh/kg] and energy density [Wh/L], cycle life, calendar life, and safety while decreasing associated costs. Lithium-ion batteries have improved upon specific energy, energy density, and capacity retention but cannot safely be used in all environments now expected, resulting from a century of ICEV improvements. Several strategies for saving costs, improving effective range, and reducing pressure on the electrical grid have been suggested and some have been attempted.

Particularly, there is the concern that too many EVs charging simultaneously during peak energy hours will exceed the power production capabilities, causing blackouts. In such scenarios, it is preferred to charge the vehicle at night, when energy demand is lower. In situations where more electricity is needed on the grid, EVs that are connected to the grid and not in immediate need of charge could serve as an immediate supply. As an alternative to plug-in charging, the battery pack can be exchanged when depleted for a fully charged battery pack [5]. The depleted battery pack can be charged, and the vehicle can be driven once the replacement battery pack is installed [5]. Swappable battery packs remove a large portion of the initial cost from the consumer; instead, the upfront cost falls on the company owning the battery packs, which is a hard sell. For large automotive companies, it is a far safer investment to produce hybrid electric vehicles (HEVs).

1.2 Similar/Previous Work

To meet these new goals, hybrid and electric vehicles need greater attention. Preceding the work that is the subject matter of this text, students under the guidance of Dr. Christopher Depcik, Professor in the department of Mechanical Engineering at the University of Kansas (KU), converted one conventional ICEV to a plug-in series hybrid electric vehicle (PHEV) and converted another ICEV to a full electric vehicle. Concluding the conversion of the 1974 Volkswagen Super Beetle (Beetle), the Beetle had an electric drivetrain with a biodiesel combustion-powered generator and attained a maximum fuel economy of 106.1 miles per gallon equivalent (mpge) [6]. The full electric vehicle, named the JimmE-V, is a second generation vehicle, wherein it underwent extensive modifications [7]. Not only do these vehicle projects give hands on experience, they can be tested to demonstrate concepts learned in the classroom. Both vehicles were tested in development of a vehicle model based on Newton's Second Law of Motion. The following work looks at a different class of electric vehicles than previous works. Here, the focus is on a Neighborhood Electric Vehicle (NEV) and many of the issues affecting conventional EVs are applicable to this class of vehicle.

1.3 Brief Look at Chapters

Chapter 2 begins with initial efforts to transition a Global Electric Motorcar (GEM) eS from lead-acid batteries to lithium-ion batteries which entailed installing a new battery charger and battery management system (BMS). Using a Newton's second law vehicle model, requisite battery capacity is determined for a specified route and different vehicle weights. The considerations of selecting a suitable battery are further discussed, followed by the process of constructing a battery pack and modifying the vehicle to facilitate the swappable battery pack.

Since the original lead-acid batteries were relatively inexpensive and robust, the GEM eS was manufactured without a designated BMS. Hence, integrating a new BMS with the extant GEM electronics proved onerous; details of troubleshooting and merging the new electronics within the vehicle outlined.

Battery management and protection are necessary because lithium-ion batteries are expensive and can be volatile if damaged. Since the new electronics were primarily to protect the battery, Chapter 3 covers battery management. Before discussing battery management in application, battery behavior is briefly reviewed, and common battery issues are described. Since electrochemistry is foundational to battery function, understanding it is prudent when maintaining battery health. With battery limitations covered, battery management practices become logical, not habitual. Lastly, the battery management strategies used in the GEM are covered. Finally, battery management practices in the GEM are outlined.

For battery management and typical vehicle use there are a few important states; in Chapter 4, the battery models used to estimate the condition of batteries are discussed. While fundamentally battery behavior is electrochemical, commercial cells are sealed and opening would destroy them. Thus, the internal state must be understood indirectly through measurable attributes such as terminal voltage, current, and temperature. Various different testing methods are presented, which also demonstrates particular interesting aspects of battery discharge behavior that may require special attention. Keeping in mind the goal of modeling and which measures are available, different mathematical models frequently found in the literature are introduced. Each model attempts to describe battery behavior without becoming exceedingly complicated. Simple models can be quite accurate but require much more data to train them, while more complicated

models may provide an adequate estimation with less effort in parameterization. To demonstrate model accuracy and suitability when used for certain cell chemistries, a few models are combined and parameterized for a variety of cells.

Lastly, Chapter 5 summarizes the previous chapters and offers ways to restore GEM functionality, improve GEM battery management, and diversify battery modeling efforts.

2 Updating and Fixing the GEM

2.1 Abstract

The subject research vehicle, a 2007 GEM eS, was purchased by the University of Kansas (KU) for campus safety patrol and then was donated to KU Center for Sustainability. After the GEM began experiencing electrical issues, it was lent to students in KU EcoHawks as an opportunity to learn about electric vehicles (EVs) through repairing and retrofitting the GEM with a lithium-ion battery pack. A GEM conservation of momentum vehicle model was developed, demonstrating reduced significantly. Thus, a swappable battery pack was implemented to increase utility. While briefly functional, the GEM was returned for repairs after an unforeseen battery management system (BMS) programming error resulted in irreparable damage to several cells in the battery pack. Where upon returning, a new higher capacity lithium iron manganese phosphate (LFMP) battery pack was constructed. BMS settings were revised and the discharge control methodology was modified. Errors imputed to the original GEM remain, preventing verifying proper BMS function.

Nomenclature

Variable	Description	Units
A_f	Frontal Area	$[m^2]$
C_D	Coefficient of Drag	$[-]$
E_{batt}	Battery Energy Output	$[J]$
F_{AD}	Aerodynamic Drag Force	$[N]$
F_{GR}	Gradation Force	$[N]$
F_{LA}	Linear Acceleration Force	$[N]$
F_{RR}	Rolling Resistance Force	$[N]$
F_{TE}	Tractive Force	$[N]$
P_{batt}	Battery Power Output	$[W]$
P_{req}	Required Power	$[W]$
U_i	Average Voltage	$[VDC]$
\bar{V}	Average Velocity	$[m/s]$
t_f	Final Time	$[s]$
η_{motor}	Motor Efficiency	$[-]$
η_{trans}	Transmission Efficiency	$[-]$
μ_{RR}	Coefficient of Rolling Resistance	$[-]$
h	Road Elevation	$[m]$
Q	Battery Capacity	$[Ah]$
V	Velocity	$[m/s]$
Z	Normal Force	$[N]$
g	Gravitational Acceleration	$[m/s^2]$
m	Mass	$[kg]$
t	Time	$[s]$
θ	Road Grade	$[rad]$
ρ	Air Density	$[kg/m^3]$
τ	Variable of Integration	$[-]$

2.2 Introduction

Global Electric Motorcars (GEM), eponymous with the starting company, are four-wheeled utility and passenger cars classified by the National Highway Traffic Safety Administration (NHTSA) as low-speed vehicles (LSVs) [8, 9]. Specifically, an electric LSV with a greater superstructure than a conventional golf cart is known as a neighborhood electric vehicle (NEV) [8, 9]. GEM started in 1998 and was sold to DaimlerChrysler in 2000. Under DaimlerChrysler,

the brand greatly expanded the number of models available, growing into the passenger vehicle and utility vehicle markets. Since 2011, Polaris Industries has owned the GEM brand.

Generally, vehicles capable of exceeding 20 miles per hour (mph) are considered motor vehicles by the Federal Motor Vehicle Safety Standard (FMVSS) [9]. However, before the introduction of the LSV class (shortly after GEM's beginning) motor vehicles capable of carrying ten or fewer passengers were defined as passenger vehicles. As such, GEMs would have been required to meet far stricter and pricier standards than as LSVs. As a result, the LSV ruling rectifies conflicting state and federal standards, while improving vehicle safety by limiting maximum vehicle speed and ensuring that the vehicles remain somewhat inexpensive.

Overall, the advancement of the NEV industry hinged on the introduction of the LSV class since it allows the vehicles to operate on certain public roads given specific characteristics. To comply with the federal standards, the maximum vehicle speed must be greater than 20 mph but not exceed 25 mph, subsequently allowing it to travel on roads where the speed limit is a maximum of 35 mph. Moreover, it must be equipped with a vehicle identification number (VIN), headlamps, stop lamps, turn indicators, tail lamps, reflex reflectors, rearview mirrors, parking brakes, windshields, and seat belts [9]. Further information regarding the FMVSS may be found in Title 49 of the Code of Federal Regulations (CFR), part 571 [9].

The GEM eS is one of the earliest models, having been originally introduced in 1998 and is the subject of this study [8]. This NEV has front wheel drive, hydraulic brakes on all four wheels, and comes standard with regenerative braking for coast down and over speed control [10]. This model is meant for utility applications; thus, it is only capable of carrying two passengers. Moreover, the payload of the vehicle, including passenger and driver, is limited such that the

gross vehicle weight rating (GVWR) does not exceed 1850 lbs. [11]. More specifically, the payload capacity is cited at approximately 690 lbs., but vehicle options might decrease this amount. Furthermore, the battery pack is a significant portion of this weight with each of the six 8G31 Deka gel lead-acid batteries weighing 70 lbs. These batteries have a nominal capacity of 98 ampere hours (Ah) and are nominally 12 volts direct current (VDC) for a total nominal pack voltage of 72 VDC [10, 12]. In operation, a direct current-to-direct current (DC/DC) converter steps down the battery voltage to approximately 12 VDC for the accessory systems. Powering the vehicle is a 5 hp General Electric (GE) heavy duty, shunt DC electric motor that is controlled by a separately excited transistorized electric motor controller (EMC) [11, 13]. An on-board Delta-Q charger converts 120 volts alternating current (AC) at 60 hertz (Hz) outlet power to suitable DC voltages to charge the lead-acid battery pack. All accessories necessitated by federal standards are included, as well as a horn, heater, windshield wipers, and light bar. Finally, radio and power outlets are available options from the vendor, but not installed in the particular vehicle under study.

2.3 Vehicle History and Purpose

A 2007 GEM eS with a cargo carrier and hard doors originally belonged to the University of Kansas (KU) campus safety patrol before it was given to the KU Center for Sustainability. While owned by the Center for Sustainability, the vehicle began experiencing electrical issues that halted the usage of the vehicle. Given the general simplicity of an NEV, it provides an excellent opportunity for students to understand and improve the functioning of an Electric Vehicle (EV). Hence, in 2013 the GEM was provided to the KU EcoHawks by the KU Center for Sustainability to update its battery pack to newer batteries while integrating a battery management system

(BMS) [14]. During the August 2013 to May 2014 period, function was the primary objective followed by increased utility while maintaining simplicity and ease of use. Because the original lead-acid batteries had been over-discharged and were at their end of life (EOL), they were delivered to a recycling company. This provided an opportunity to revisit the use of the relatively heavy lead-acid batteries in this vehicle.

By decreasing the weight of the vehicle, provided the battery capacity remains the same, vehicle range can be extended. Lead-acid batteries, on average, have a specific energy of about 35 watt-hours per kilogram (Wh/kg); thus, for a battery pack to contain more energy per weight, it must have a higher specific energy. One consideration was nickel-metal hydride (NiMH) batteries, which commercially have specific energies between 63 and 75 Wh/kg [15]. However, since lithium-ion batteries have greater specific energies than lead-acid batteries (and generally higher than all other commercially available secondary batteries), the new battery pack would utilize a type of lithium-ion battery [15]. Despite the lower specific energy of lithium iron phosphate (LiFePO_4 or LFP) batteries (est. between 90 and 120 Wh/kg) as compared to higher capacity lithium-ion cells like lithium nickel cobalt aluminum oxide (LiNiCoAlO_2 or NCA; est. between 200 and 260 Wh/kg), LFP cells were chosen because of their thermal stability, low memory effect, and high power producing capabilities [16-18].

Decreasing the weight of the batteries could have the additional effect of making it easier to remove the batteries. Although the new batteries could be situated where the lead-acid batteries were originally, this would not improve access. Bearing in mind public qualms with EVs, particularly range anxiety and fast charging demands, equipping the vehicle with a swappable battery pack may assuage such concerns [3, 14]. Thus, the vehicle could be retrofitted with a

battery drawer or tray that could hold the battery pack. The subsequent access to the battery pack simplifies maintenance and facilitates interchangeable battery packs. This only became a feasible option since the total weight of the battery pack will be reduced from 420 pounds (lbs.) to 82 lbs. (note: battery pack sizing is indicated in the next section). Hence, two individuals can reasonably lift the battery pack. This is in opposition to disconnecting the batteries and removing them individually, which was the requirement of the lead-acid batteries. When applied to full-scale electric vehicles, machinery is often employed to facilitate battery pack removal [1].

2.4 Electric Vehicle Modeling

The desired battery capacity (i.e., amp-hours or Ah) was determined based on a route established by conferring with the Center for Sustainability while including the additional target of minimizing the cost of the battery pack [14]. Using vehicle specifications and a profile of the route, the energy requirements were estimated by applying Newton's second law and the conservation of momentum. In this model, the tractive force (F_{TE}) that the vehicle must apply to obtain a certain velocity profile is equal to the sum of four forces:

$F_{TE} = F_{GR} + F_{AD} + F_{RR} + F_{LA}$	(1)
--	-----

The gradation force (F_{GR}) accounts for the road grade (θ). Here, a vehicle going downhill is assisted by gravity (g); whereas, a vehicle driving uphill must overcome gravity. A steeper grade and increasing the vehicle mass (m), can result in greater magnitudes of gradation forces.

$F_{GR} = mg \sin \theta$	(2)
---------------------------	-----

Grade can be determined based on the height of the road (h) and the displacement, which is the product of average velocity (\bar{V}) and time (t). Explicit differentiation, denoted by Δ , is used because the data sampling rate is assumed to be sufficiently high so the difference between two points is small [14].

$\theta = \tan^{-1} \left(\frac{\Delta h}{\frac{1}{2} \bar{V} \Delta t} \right)$	(3)
---	-----

The second force considers aerodynamic drag (F_{AD}). Since the GEM is limited to 25 mph, the following approximation is reasonable:

$F_{AD} = \frac{1}{2} \rho A_f C_D V^2$	(4)
---	-----

Frontal area of the vehicle (A_f) can be approximated as 84% of the product of the height and width, which is sufficient given that only a rough estimate is needed in this case [6, 19]. Also vehicle dependent is the coefficient of drag (C_D), which can be approximated based on other vehicles or calculated through coast-down and wind tunnel tests. Though the GEM cab has rounded features, features such as the side mirrors, protruding front bumper, cargo carrier, and light bar all disrupt the flow of air around the vehicle. For typical passenger vehicles, C_D generally ranges between 0.3-0.6 [20]. Therefore, a coefficient of drag of 0.6 was assumed as this will increase the expected energy demand and should the actual coefficient be lower, the GEM will go farther on a full charge. Air density (ρ) at testing conditions is the final variable and determined through the ideal gas law.

The force due to rolling resistance (F_{RR}) acts against the movement of the vehicle. Since the vehicle is moving slow enough to disregard the effects of lift, the vehicle weight and the road grade are the only factors contributing to the load perpendicular to the road surface (Z):

$Z = mg \cos \theta$	(5)
----------------------	-----

Rolling resistance describes the energy lost as the tires interact with the ground. Energy from the vehicle system is spent as the tire deforms on contact with the road, but as the tire is not perfectly elastic, not all of the energy is returned to the system in what is known as hysteresis. For vehicles capable of a larger range of speeds, the contact area between the tire and the ground will vary, behooving consideration. Moreover, tire pressure, the normal force of the vehicle, and the velocity all factor into the force of rolling resistance. However, provided that the vehicle remains at low speed, the rolling resistance can be simplified. Here, the coefficient of rolling resistance (μ_{RR}) is a generalized value depicting what portion of the normal load opposes motion. Using this simplified view of rolling resistance:

$F_{RR} = \mu_{RR}Z$	(6)
----------------------	-----

The final force considered is the linear acceleration term (F_{LA}). Traction must incorporate the force acting to change the velocity of the vehicle. Again, assuming a high sampling rate of velocity and using explicit differentiation:

$F_{LA} = m \frac{\Delta V}{\Delta t}$	(7)
--	-----

Once the tractive force is calculated for each moment, the power requirement can be determined:

$P_{req}(t) = F_{TE}V(t)$	(8)
---------------------------	-----

Required power (P_{req}) is lower than the actual power provided by the battery pack because there are mechanical and electrical losses within the system. The losses considered in the GEM are attributed to the transmission efficiency (η_{trans}) and motor efficiency (η_{motor}). As a result, battery power output (P_{batt}) is given by:

$P_{batt}(t) = \frac{P_{req}(t)}{\eta_{trans}\eta_{motor}}$	(9)
---	-----

By integrating the battery power over the duration of the test, using Simpson's rule, the battery energy (E_{batt}) over the driving profile is determined [14].

$E_{batt} = \int_0^{t_f} P_{batt}(\tau) d\tau$	(10)
--	------

Finally, the total charge capacity of the battery (Q) is calculated using an average voltage value (U_i) and converted to ampere-hours (Ah) as opposed to coulombs (C).

$Q = \frac{E_{batt}}{U_i * 3600}$	(11)
-----------------------------------	------

2.5 Initial Upgrade of GEM to LFP Battery Pack

2.5.1 Initial 40 Ah Lithium-Ion Battery Pack

For a single route, the batteries were required to meet a minimum capacity of 22 Ah as determined from the model and based on approximations of vehicle characteristics [14].

However, considering the vehicle might not always be used as the route suggests and may not be at full capacity, 40 Ah was determined to be sufficient with a safety factor of nearly two. The batteries chosen were CA40 (CA is the series label and 40 is the capacity) manufactured by the China Aviation Lithium Battery (CALB) Co. and concerning cell geometry, there were three available options: pouch, cylindrical, and prismatic.

Generally, pouch cells are less prone to internal heating because they have a higher surface area to volume ratio. Furthermore, pouch cells weigh less at the same capacity as prismatic cells because they lack the larger terminals and protective shell. However, this can become an issue as they become more prone to puncture and deformation. In addition, in the event of gas formation in the cell, the pouch will expand. Subsequently, this expansion may lead to instances where positive and negative electrodes are displaced enough to make contact, resulting in an internal short circuit. Then, in the presence of the high heat generated by a short circuit, some of these released gases are combustible, consequently leading to catastrophic failure of the cell.

Comparatively, the shell of prismatic cells reduces the degree of expansion, and in some situations, external pressure is applied to suppress material phase changes and contact loss through delamination [21]. Finally, terminals on pouch cells are more prone to damage through physical means. In turn, repeated connecting and disconnecting becomes more onerous.

Cylindrical cells, when arranged in straight lines, have ample room between them for air to move, allowing for better temperature control. Even when this option is more tightly spaced, there is still more room for air to move than with prismatic cells. In addition, a few cylindrical cell designs (and many prismatic cells) include vents in response to potentially dangerous gas formation of certain battery chemistries to relieve pressure buildup. Prismatic cells are more

resistant to puncturing and pack together more tightly. The decision to use prismatic cells was also predicated on simplicity of establishing electrical connections. Connecting and disconnecting cells using bus bars is far easier than tab welds on cylindrical cells.

Unlike lead-acid batteries, which supplied approximately 12 VDC apiece, the lithium-ion batteries considered each contributed approximately 3.3 VDC. This level of modularity was chosen to decrease potential repair costs, should a cell fail. Not only could individual batteries be replaced, configuration of the pack could be changed to suit design needs. Assuming that the core components of the vehicle would remain the same, the voltage of the battery pack would need to stay within a certain range. The repair manual suggests not to exceed 86 VDC, which is confirmed by the motor controller operation manual [11, 13, 22]. Additionally, pack voltage should not fall below 68.3 VDC as this will cause an error status in the vehicle [13].

Shut off voltage for the original lead-acid batteries was 10.5 VDC and below this voltage, the cell would need to be individually charged. Maximum voltage for the lead-acid batteries was approximately 12.7 VDC. The lithium iron phosphate batteries chosen were produced by CALB and are suggested to remain between 3.6 VDC and 3.0 VDC, according to the 2009 version of the installation and maintenance manual [23]. This means that the upper voltage limit of the pack using 24 fully charged batteries (i.e., 86.4 VDC) will slightly exceed the upper threshold expected by the motor controller; thus, a high voltage error will be shown on the vehicle display. However, battery health can be better preserved by reducing the maximum voltage and increasing the minimum voltage allowed for the batteries [24-26]. In EV applications, batteries are often not discharged past 80% or rarely 90% of their total capacity [20, 24]. Here, LFP

batteries should also not be overcharged because it will cause irreparable damage to the cathode and increase heat generation within the cell [18].

Each LiFePO_4 cell weighs 1.5 kg, for a total weight of 36 kg or roughly 80 lbs.; whereas, the original lead-acid batteries contributed 420 lbs. to the weight of the GEM. The lithium cells were connected in series using copper bus bars, spanning two rows so that the first and twenty-fourth batteries were at the same end.



Figure 1: Battery box for the 40 Ah batteries.

The battery box, shown in Figure 1, was constructed using half-inch thick nylon sheets that are bolted together at the corners using corner brackets. Four edge brackets were attached near the top of the box to brace the sides while four wide edge brackets ensured that the bottom of the box was secured. Overall, the box was 23.5" long, 10.5" wide, and 9" tall and nylon was chosen because it is electrically insulating. A drawer liner was laid underneath the batteries and on all internal sides to act as a cushion against shock when driving. Two drawer handles were bolted to the most distal sides of the box, then the box was spray painted black for aesthetic purposes. Despite using heavier prismatic cells, the battery pack can be lifted by two people using these

drawer handles. An eighth inch sheet of clear plastic was used as a cover for the top of the battery pack to increase protection from dust and wear while being kept in place by four hook-and-loop fasteners. Overall, clearance between the battery pack and the underside of the vehicle is respectively small.

2.5.2 Physical Changes to GEM/Construction

Before the 40 Ah batteries could be purchased, their placement within the vehicle was deliberated. Originally, four lead-acid batteries were accessible by removing the bench seat in the cab while the remaining two were located behind the first four and could be accessed through a hatch in the bottom of the cargo carrier. The lead-acid batteries, each having a base area of $12.9'' \times 6.7''$, resided on approximately 520 square inches (in^2) of surface. The trays holding the lead-acid batteries were not contiguous; each was separated by sections of the vehicle frame, as seen in Figure 2 [12].

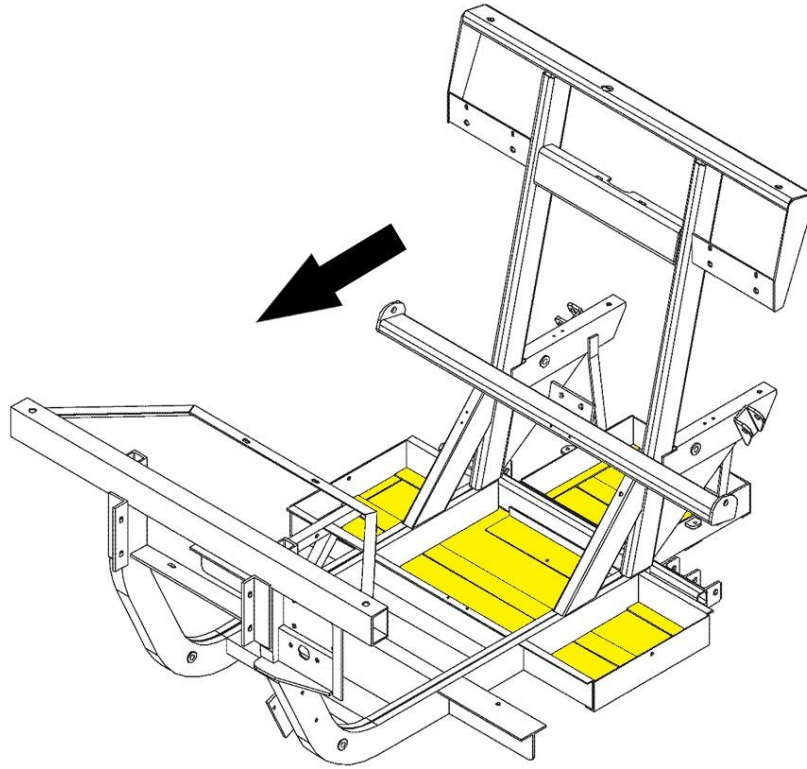


Figure 2: Frame weldment for 2007 GEM 2 passenger vehicles [12]. Highlighted regions in yellow show where the lead-acid batteries were originally placed. The arrow points towards the front of the vehicle.

The overall area required for the 40 Ah lithium-ion batteries is less than half of the area covered by the lead-acid batteries. However, this does not consider the BMS that is required for properly maintaining these batteries nor does it include a new charger, since the Delta-Q charger is meant for lead-acid batteries only.

Depending on the location of the battery pack while connected to the vehicle, its removal may entail an extending drawer, a lifting mechanism, or a lowering mechanism. Of these three options, the extending drawer made the most sense since both the lifting and lowering mechanisms would have required refabricating the GEM's chassis. There were a few options for the location of the battery drawer on the vehicle with most EVs allocating space for the pack on

the underbody [27]. Furthermore, at the request of the project sponsor, the battery pack should not interfere with the capability of the vehicle to carry passengers nor cargo. Thus, the battery pack could not be placed in the cargo carrier. Moreover, storing the batteries higher on the vehicle will raise the center of gravity and increase the risk of rollover. In addition, disproportionally augmenting the weight at either the front or rear of the vehicle will impinge vehicle handling. Originally, the GEM weight was distributed nearly equally between the front and rear [28]. Placing the battery drawer under the bench would complicate the procedure of removing the battery pack from the vehicle and could entail removing parts of the vehicle frame and doorframe. The only remaining available space is under the cargo carrier, between the C-channels seen in Figure 3. This would increase weight at the rear of the vehicle; however, by utilizing a sliding drawer, the pack can be closer to the center of the vehicle—and the original location of the batteries—while in use. When removing the battery pack, the drawer can be extended from the rear of the vehicle.

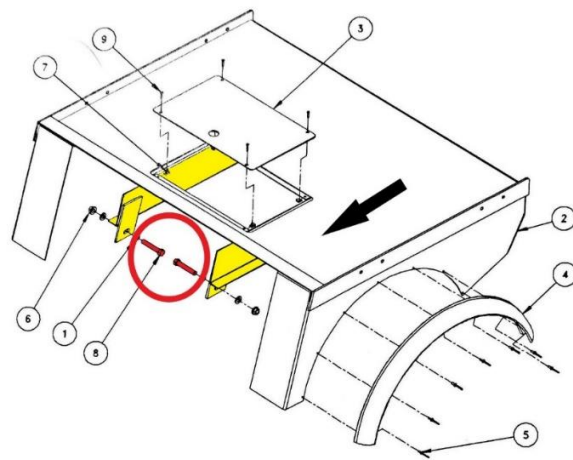


Figure 3: Small utility bed assembly drawing for the 2007 GEM eS [12]. Visible regions of the two C-channel supports are shaded yellow. An object supported by the two C-channels cannot extend any further under the vehicle than the two hex bolts, circled in red. Forward direction of the vehicle is signified by the large black triangle.

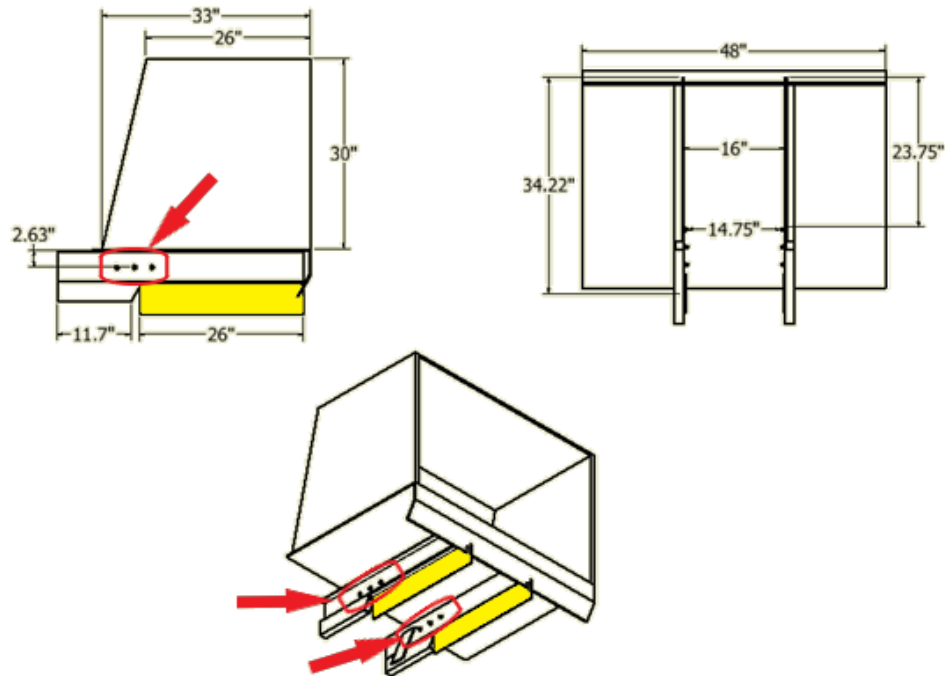


Figure 4: Simplified CAD portrayal of the cargo carrier and features significant to mounting the battery drawer [14]. Aluminum L-beams, highlighted in yellow, were added to the vehicle. Red arrows point towards the three bolts that prevent mounting the sliders on the C-channels.

Since the lead-acid batteries are being replaced, the rear battery tray can be removed. However, should the vehicle transition back to lead-acid batteries, the battery drawer ought to be built robust enough to support the weight of the original batteries while fully extended and large enough to fit all six lead-acid batteries. The width between the two C-channels shown in Figure 4 is 16" while the length between the rear bumper and the red hex bolt in Figure 3 is 36". It would not be prudent to remove the C-channels because they support the base of the cargo carrier and prevent it from warping or giving way while loaded. The red hex bolt in Figure 3 connects the small utility bed assembly to the frame weldment seen in Figure 2; thus, this should not be damaged in any way. The three bolts seen in Figure 4 require that the drawer slides are shorter than 24" while reducing the available width to less than 15". This space limitation was avoided

by bolting an L-beam to the bottom of the C-channel so that the drawer slides are positioned lower than the three bolts. Still, by having the drawer extend beyond the rear bumper, the section of the rear bumper on which the license plate and light rested needed to be removed. As a result, the license plate was relocated to the upper right area of the cargo carrier door.

When the battery pack is in use, the drawer should not extend up to, or past, the bumper to minimize the likelihood of an object striking it. Furthermore, the drawer slides must be narrow to increase the room available for the battery drawer and battery pack. Heavy duty, 32" full extension drawer slides from Hettich were chosen for their high repeatable loading weight and thin profile. Together, their width is 1.5", with 14.5" remaining for the battery pack. Full extension of the drawer slides is important so that the battery pack can be extended its full length from the vehicle. The battery drawer that was designed to carry the first lithium-ion battery pack was constructed of 1/8" thick aluminum, welded along the inside seams to form a box 32" in length, 14.5" wide, and 10" deep. As the battery pack must be removable, the pack must be small enough to fit within the battery drawer and large enough to hold the lithium-ion batteries.

2.5.3 Extant Electrical System

Sections of the vehicle wiring were modified or altogether removed with the introduction of new components. Since the license plate was moved, the license plate lamp and its associated wiring was removed. Furthermore, malfunctioning systems or purportedly broken items were replaced. In the transition to the 40 Ah LFP battery pack, the entire heater unit and its associated wiring were replaced because the system itself was reportedly dysfunctional and a few of its wires were damaged. Moreover, the original GEM charger was disconnected; however, it remained in the vehicle. Finally, cables connecting the lead-acid batteries were removed, concomitantly with the

battery fuse and battery temperature sensor. Before the details of wiring changes are discussed, the wiring and functions of several key components will be established.

Original vehicle wiring can be found in the GEM owner's manuals with the color of each wire abbreviated according to Table 1. Since there are a substantial number of wires in the vehicle, wires moving collectively between two sections of the vehicle are bundled together into harnesses. Most of the original vehicle wiring is represented by the harnesses, which are listed in Table 2.

Table 1: List of wire color abbreviations and their corresponding colors.

Color Acronym	Color
BK	Black
BR	Brown
DB	Dark Blue
DG	Dark Green
GY	Gray
LB	Light Blue
LG	Light Green
OR	Orange
PK	Pink
RD	Red
TN	Tan
VT	Violet
WT	White
YL	Yellow

Table 2: List of wire harness and their abbreviated names.

Harness Name	Abbreviated Name
Front Harness	FH
Rear Harness	RH
DC/DC Converter Harness	DCCH
Instrument Panel Harness	IPH
Headlight Harness	HH
Motor Controller Harness	CH

2.5.4 System Specifications

Any electronic additions to the vehicle must work well with the original vehicle components.

Methods of ensuring battery safety and longevity also need to be introduced. With the addition of the new battery packs came the need to limit battery discharge and charge rates. In specific, discharging at excessive rates will immediately, though temporarily, decrease available battery capacity and expedite the ageing process. In terms of vehicle power requirements, the electric motor is rated to use 56 A to generate its electric field. Besides main driving functions, the accessories can draw a significant amount of power. Particularly, the cabin heater coil can draw a maximum of 30 A and the 12 VDC accessory systems can draw power at a maximum of 9.5 A, which is limited by the DC/DC converter. For the battery packs, drawing 90 A continuously will deplete the batteries too quickly and decrease the overall lifespan of the cells. Therefore, applying reasonable limitations to the charge and discharge rate will increase the life of the batteries. As a result, a battery management system (BMS) is meant to discern and report the state of the battery and then based on conditions and demands, subsequently act to limit harm. For instance, when too much current is being drawn from the battery too quickly, the BMS should reduce the current. Overall, the BMS will keep track of the state of charge of the battery so that it can decide when to stop all discharge events or to allow charging. Furthermore, many BMSs derate the current available based on temperature conditions, limiting discharge and charge if the batteries are too hot or too cold.

2.5.5 Electrical Components

2.5.5.1 Power Signal Distribution Module

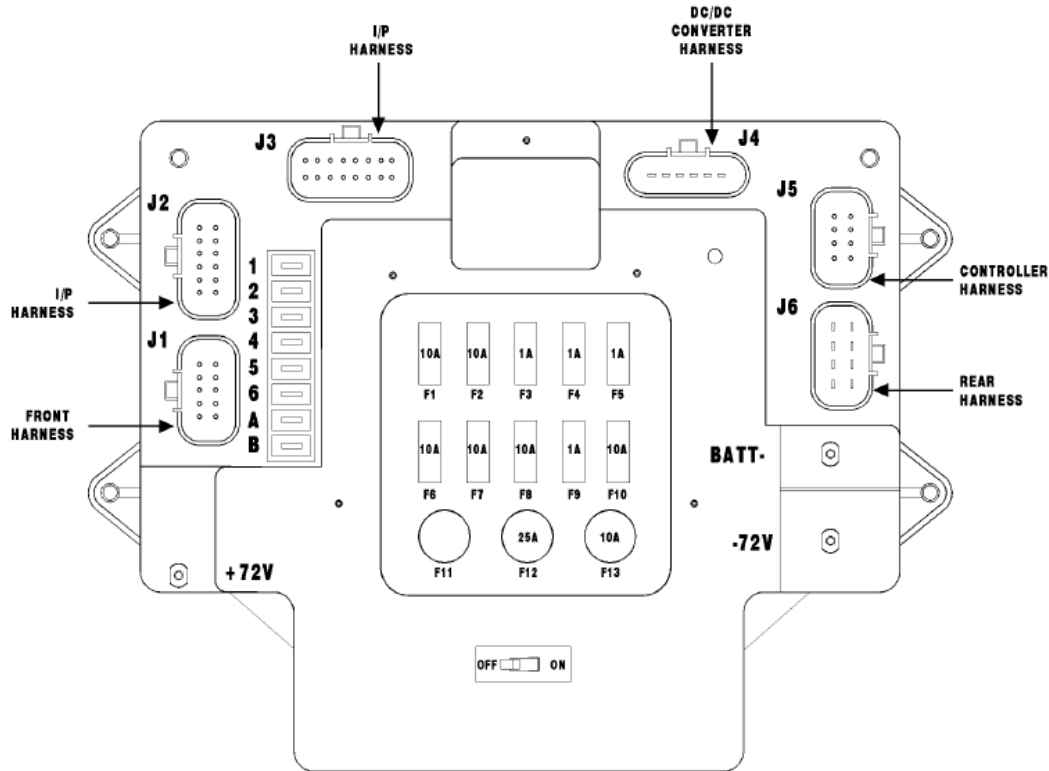


Figure 5: PSDM connector locations [22].

The GEM has several important discrete components assisting its functionality. Specifically, all current entering or drawn from the battery pack goes through the power signal distribution module (PSDM). Partially behind the PSDM is the master disconnect switch (MDS) with the MDS on/off toggle seen in the lower section of the PSDM shown in Figure 5. The high potential from the positive terminal of the battery pack connects to the MDS on the passenger side, while the MDS is connected to the +72 VDC post on the PSDM, also seen in Figure 5. When off, the MDS is open; thus, preventing the flow of current. However, when on the MDS is closed, subsequently allowing current flow through the circuit. Here, the low potential from the negative

terminal of the battery pack connects to the BATT- post on the PSDM. The role of the PSDM is exactly as its name suggests: this component facilitates the majority of communications and power supply within the vehicle. Moreover, all vehicle fuses, except for the battery safety fuse next to the battery pack, are connected to the PSDM. This centralized location allows maintenance to be accomplished quicker and more readily. There are ten automotive blade fuses and three slots for cylindrical glass fuses, all listed in Table 3; however, only two of the cylindrical fuses are ever in use.

Slots 1-6, A, and B supply power to accessories, and as seen in Figure 5, they are just to the right of connectors J1 and J2. These connection points are labeled as S1, S2, etc. The top slot, S1, provides fused and switched (FAS) 12 VDC; whereas, S2 supplies FAS 12 VDC to the heater switch that powers the heater blower motor and the heater contactor coil. The next slot, S3, supplies 12 VDC to both the power outlet and the light bar. When the heater contactor switch is closed, SA supplies 72 VDC power (the required battery pack voltage) to the heater element. Electrical components throughout the vehicle are connected to the PSDM with wires and cables sorted by region and harnessed together. The pins of each connector are labeled alphabetically (i.e., the first pin is pin A), but skip the letters I, O, and Q likely because they are more difficult to differentiate. Connectors J1-J6 on the PSDM hold the pins while the connectors J1-J6 on the harness side, are sockets. The top right socket of connector J1, socket side and clasp upwards, is J1A. The sockets proceed right to left then top to bottom.

Table 3: PSDM fuse description.

Fuse Number	Rated Amperage and Fuse Type	System
1	10A – Blade Fuse	Headlights and Taillights
2	10A – Blade Fuse	Heater Switch (Coil Power)
3	10A – Blade Fuse	Radio Switch

4	1A – Blade Fuse	Odometer Switch
5	1A – Blade Fuse	Display
6	10A – Blade Fuse	Blinkers and Brake Level Switch
7	10A – Blade Fuse	Wiper
8	10A – Blade Fuse	Power Outlet and Light Bar
9	1A – Blade Fuse	Key Switch to Charger Interlock and Display
10	1A – Blade Fuse	Radio Memory/Power
11	-	Spare
12	30A – Cylindrical Glass Fuse	Heater Contactor Power
13	10A – Cylindrical Glass Fuse	72 VDC System Power

2.5.5.2 Module Motor Controller



Figure 6: Beige colored version of the motor controller installed in the 2007 GEM eS [13].

Installed in the vehicle is a separately excited (SX) transistorized motor controller from General Electric, model IC3645SR7A353T3, like the one shown in Figure 6. This module controls many of the vehicle's primary functions. This electric motor controller (EMC) modulates the power going to the shunt DC motor, determines if the vehicle is safe to operate, and sends error codes to the instrument pod display. Before the addition of the BMS, the EMC was responsible for the wellbeing of the batteries. The vehicle would not drive if the batteries were above or below the acceptable voltage range. Additionally, the vehicle would shut down, prohibiting driving or further battery pack discharge, when the batteries were too hot, or the emergency brake was

engaged. In addition, the motor controller inhibits the vehicle from exceeding speeds of 25 mph, even when going downhill.

Table 4: SX Transistorized EMC NEV Application I/O List [13]. Pin 13 is N/A until changes made in Section 2.6.3.6.

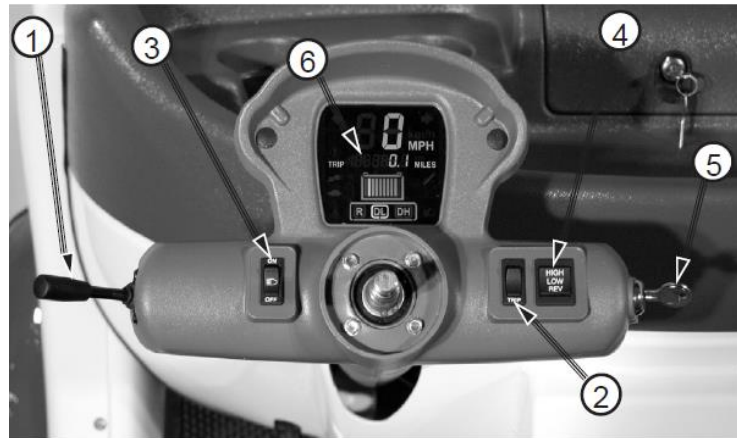
Pin	Main Input/Output (I/O) Description
1	Positive Battery Voltage (Key Input)
2	Positive Battery Voltage (Key Input)
3	Negative Battery Voltage (Accelerator Start Switch)
4	Positive Battery Voltage (Forward Switch)
5	Positive Battery Voltage (Reverse Switch)
6	Positive Battery Voltage (Turf Speed Limit Switch)
7	Accelerator Input Voltage Signal
8	Accelerator Negative
9	Accelerator Potentiometer +5 VDC Supply (3 Wire Potentiometer)
10	Reverse Alarm
11	N/A
12	Negative Battery Voltage (Regenerative Braking Switch)
13	Negative Battery Voltage (Parking Brake Relays)
14	Tachometer Input Signal
15	Tachometer 12 VDC Output
16	Tachometer Negative Voltage
17	Main Contactor Coil Driver
18	N/A
19	N/A
20	Negative (DP9)
21	Positive Battery Voltage (Motor Thermal Switch)
22	Serial Receive (DP9)
23	Serial Transmit (DP9)

2.5.5.3 DC/DC Converter

Accessory systems are provided an approximate 12 VDC by the DC/DC converter (Sure Power 71030i from Eaton). Its nominal input voltage can range from 72 to 96 VDC and continuous current draw should remain below 9 A with a maximum current output of 30 A. All 12 VDC systems are grounded to the vehicle chassis, which must remain isolated from the high voltage

(HV) system. The DC/DC converter is located under the hood on the driver's side, adjacent to the motor controller.

2.5.5.4 Instrument Pod/Display



1. Turn Signal/Windshield Wiper/Horn Lever
2. Trip/Odometer Switch
3. Headlight Switch
4. Forward/Reverse Switch
5. Key Switch
6. LCD Display

Figure 7: Instrument pod with features enumerated and labeled [11].

Accessory systems critical to vehicle operation are located on the steering column, which are enumerated in Figure 7. The key switch is on the right side of the instrument pod and a multi-function switch located on the left has the appearance of a joystick. By pressing the black knob inward towards the display, the horn is activated. Moreover, tilting the lever downward from horizontal triggers the left directional indicator, while tilting the lever upward from horizontal triggers the right directional indicator. Pushing the lever away from the driver will activate the windshield washer fluid pump and spray the windshield; whereas, tilting the lever towards the driver switches on the windshield wipers.

There are three rocker switches on the instrument pod. The furthest left rocker switch controls the lights; its neutral position is off. Rocking the switch forward turns on the lights, backward will additionally turn on the high beams. The furthest right rocker switch controls the drive mode. Neutral position starts the vehicle in low, which limits the maximum speed to 15 mph. The forward position initiates high mode, which allows the vehicle to reach a maximum of 25 mph. As a safety precaution and as part of vehicle regulation, even on hills the vehicle will slow itself to avoid surpassing its maximum speed. Tilting the drive mode rocker switch backward turns on reverse mode and actuates a back-up beeper to alert the driver and other proximal people. Just left of the drive mode switch is the trip switch. While the vehicle is on, notifications about active accessories and vehicle status are shown on the LCD Display as seen in Figure 8 and described in Table 5.

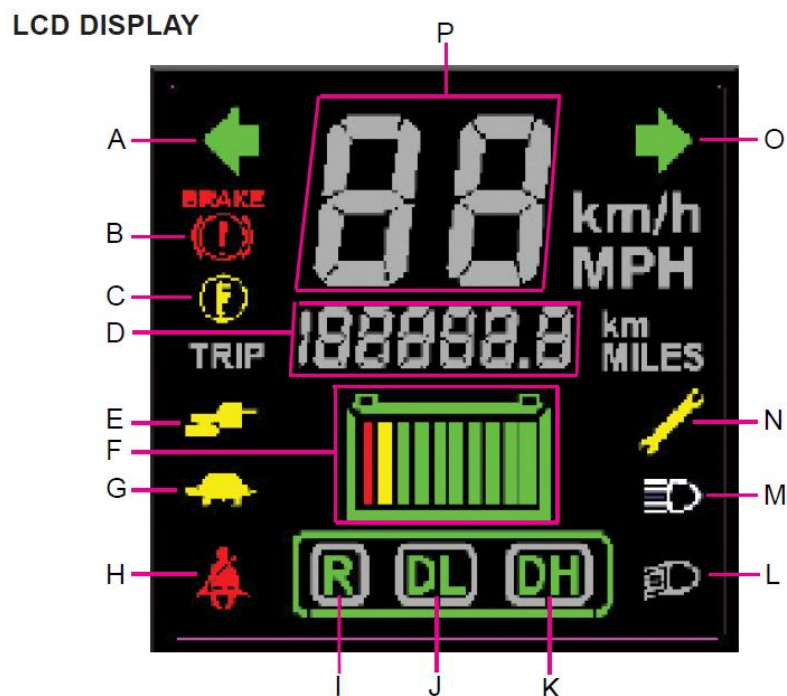


Figure 8: LCD indicators are itemized and shown where they appear when the vehicle is in use [11].

Table 5: Description of indicators itemized in Figure 8.

Item A	Left Turn Indicator
Item B	Low Brake Fluid Level/Parking Brake On
Item C	High Motor Temperature
Item D	Odometer/Trip Meter
Item E	Charger Connected
Item F	State of Charge Indicator
Item G	Turtle Mode—Current Limiting Mode
Item H	Safety Belt Warning
Item I	Drive Mode Reverse
Item J	Drive Mode Low
Item K	Drive Mode High
Item L	High-Beam Lights On
Item M	Headlights On
Item N	Service Required
Item O	Right Turn Indicator
Item P	Speedometer/Error Code Display

2.5.5.5 Lights

When installing the battery drawer, a section of the rear bumper was removed to allow unimpeded movement of the drawer. This entailed moving the license plate onto the door of the enclosed cargo carrier and removing the section of wire dedicated to the license plate light. Both positive and negative wires for the license plate lamp were disconnected from the rear harness, but no changes were made to the taillights.

Secondly, there is an inconsistency between how the manuals describe the wiring of the headlights and the actual wiring. Redrawing the wiring diagrams is a significant undertaking, especially considering the diagrams may be used to convey different information. Some wire diagrams show the exact wiring, while other diagrams serve to show how the diagram fulfills its purpose. While the LCD display in Figure 8 includes high beams, the past wiring diagrams

completely omit the wires and connectors for this purpose. Lastly, regarding the vehicle lights, the GEM dome light is optional and is not included in this model. However, this vehicle does include a light bar on the roof.

2.5.6 Battery Management System

Based on previous experiences with BMSs, it was recommended to use a centralized BMS rather than a distributed system. Specifically, the task of fitting a battery pack with cell boards on each cell and maintaining their operation is decidedly far too tedious as illustrated by a significant number of cell board malfunctions for prior projects [7]. In addition, for mobile applications, cell board connections become worn down and cease functioning. Moreover, the BMS needed to meet a few stipulations. It had to be capable of handling 24 lithium ion cells, voltages ranging from 87 VDC to as low as 60 VDC, not harmed by damp conditions, and preferably programmable. Reviewing available options, the Orion BMS met all the provisions required.



Figure 9: : Original Orion BMS [29].

The Orion BMS, seen in Figure 9, is a programmable device used to ensure that the batteries are used safely. In addition, this device measures and records data on the cells, communicates with other devices, and plays a significant role in the functioning of the vehicle. Communication with other devices and power supplied to the BMS are all part of the main I/O connector, seen in Figure 10. Each wire is labeled and color-coded corresponding to the aforementioned Figure 10. For now, it suffices to describe how the BMS is wired and discussion of the wiring methodology is provided in the subsequent chapter.

When the vehicle is in use, the BMS is powered through Ready Power, pin 2 of the Main I/O Connector. While the vehicle is connected to an external power source to charge the battery pack, the BMS is powered through Charge Power. Ground wires referred to in Figure 10 are connected to the vehicle chassis, which is the 12 VDC GND. BMS controls and communications in the GEM utilize Charge Safety, Discharge Enable, CAN1_L, CAN1_H, and CAN1_SHIELD. All remaining Main I/O wires remain disconnected.

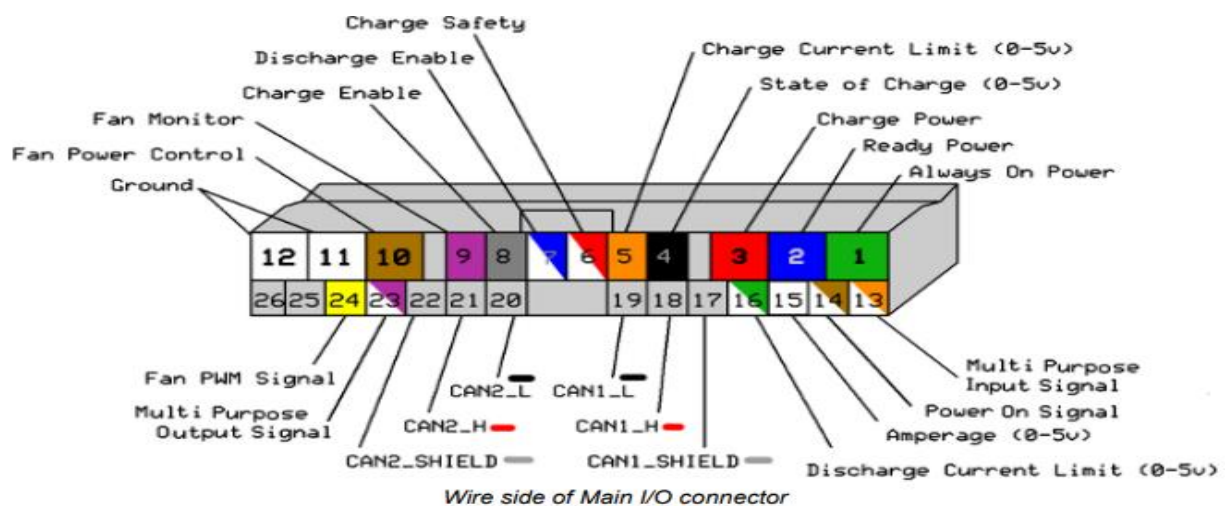


Figure 10: Orion BMS Main I/O Connector pinout with wire color and function indicated [29].

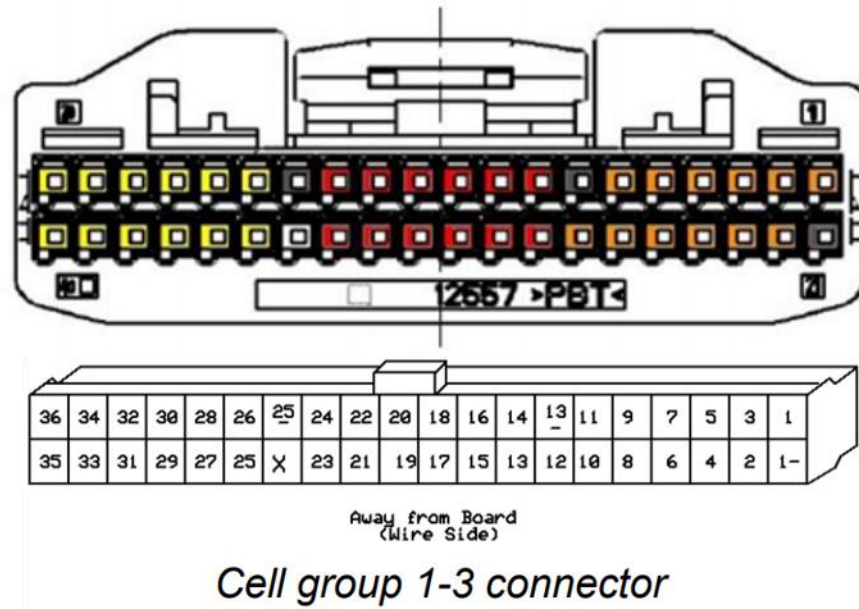


Figure 11: BMS cell group connector diagram with pins labeled according to the associated battery terminals [29].

Only one cell group connector is needed because there are 24 cells in the battery pack. Wires from the cell group connector, which are labeled as seen in Figure 11, connect to terminals of the same number; i.e., wire 1- connects to the negative terminal of cell 1. The wires from the cell group connector are called cell voltage taps, of which there is one for every positive cell terminal and one for the first and thirteenth negative terminals. In order to disconnect the battery pack quickly from the vehicle, a circular connector is used to connect the wires from the battery side to the vehicle side. Ring connectors are used on the battery side to make connections. While it is not the case in the GEM, was there a fuse or some other safety disconnect placed between cells within the pack, the BMS would require the disconnect fall between two cell group connectors. Though there is some benefit to having a fuse or safety disconnect between cells 12 and 13 (i.e., when the fuse is blown, each half of the battery pack encounters a maximum voltage half that of the original pack voltage with the voltage between the terminals becoming approximately 0

VDC), the isolation between adjacent cells within the Orion BMS is not sufficient to prevent current flow. Though the voltage across the pack ought to be decreased when the fuse is blown, the electrical isolation within the BMS may not be enough to prevent current flow through the BMS; thus, damaging the BMS. Stray inductance produced when a fuse is blown due to over-current may also produce large transient voltages that can damage the BMS. Isolation between pins of a cell group may only withstand 5 VDC difference before the internal fuse is blown. Here, BMS revision E can withstand ± 24 VDC for short periods, but may still incur damage, either damaging the BMS or draining the improperly connected battery. As a result, a 100 A fuse was installed in series after cell 24. This fuse can withstand voltages greater than the potential of the battery pack and has a current rating slightly higher than allowable by the BMS. Therefore, if the BMS fails to limit the current, the fuse will break and prevent further discharge.

Similarly, it is mandatory to disconnect the cell group and main I/O connectors when conducting modifications to battery pack wiring. Furthermore, Orion BMS offers a cell tap validator to verify that wiring has been done correctly. While more tedious, it was more economical to validate cell taps manually by ensuring continuity between each pin of the cell group connector and its corresponding cell voltage tap.

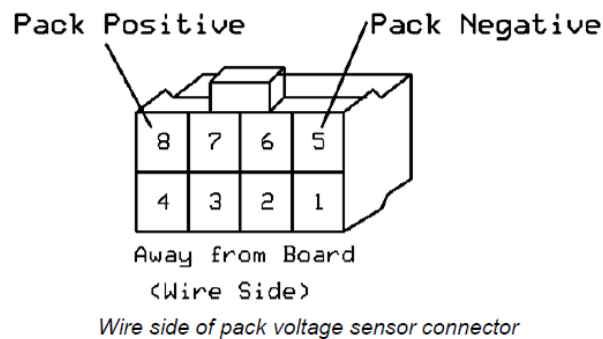


Figure 12: Pinout of the pack voltage sensor connector that links to the BMS [29].

While the total pack voltage is determined by the voltage taps, the pack voltage sensor seen in Figure 12 provides a redundant voltage monitor while also checking for isolation faults. Two wires share the same pins on the BMS side of the circular connector; specifically, the wire leading to the negative terminal of the first battery shares a pin on the BMS side with the pack negative wire from the pack voltage sensor connector. Similarly, the wire connected to the positive terminal of the twenty-fourth battery shares a pin on the BMS side of the circular connector with the pack positive wire from the pack voltage sensor connector.

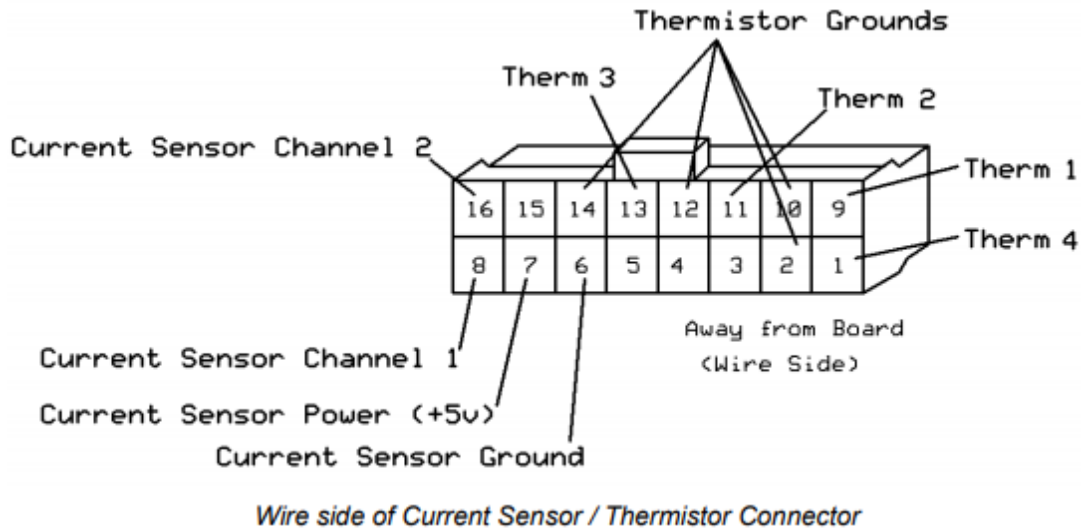


Figure 13: BMS current sensor and thermistor connector [29].

The final BMS connector is the current sensor and thermistor connector, which is labeled in Figure 13. There are four thermistors available to collect temperature data about the battery pack. Current flow through both the positive discharge and charging cables is measured using a 200 A Hall Effect Dual Range current sensor from Ewert Energy.

2.5.7 Choosing a Charger

Originally, the GEM used a Delta-Q QuiQ charger (model 912-7200-01) for its lead-acid batteries. This model has six dissimilar charging profiles for different lead-acid battery brands and for when the batteries had been severely discharged. Profile number 14 best suited for the GEM DEKA 8G31 Gel batteries that were initially in the vehicle [30]. Even though the lead-acid batteries were removed, the charger remains in the vehicle should the owner want to revert to using lead-acid batteries once again.

Since the Orion BMS can communicate over a Controller Area Network (CAN) bus, finding a CAN-enabled battery charger that also meets the battery pack specifications was preferred. Therefore, an Electric Conversions (ElCon) power factor controlled (PFC) 1500 battery charger was chosen (model TCCH-72-16). In addition, the Orion BMS manual recommends having redundant control over charge and discharge events, subsequently allowing it to cut power immediately should a safety concern or risk of battery pack damage arise.

When connected to an AC source within the range of 85 VAC to 265 VAC and a frequency between 45 and 65 Hz, the charger will turn on and begin communicating over CAN with the BMS to determine if and how the batteries should be charged. For this charger, there are ten different charging programs available, which may be selected by powering the charger and holding the black button. By counting the number of green LED flashes, the user can determine which method has been selected. When active, the charger will indicate issues through a pattern of green and red LED flashes, which are described in Table 6. It will cycle through these issues while including one-second stops as part of the cycle, repeating until power is removed or the issue has been corrected.

Table 6: ElCon PFC charger flashing sequence description.

	LED Flashing Sequence	Description
1	R G _ _ _ _ _	Wrong Battery
2	R G R _ _ _ _	Overcharged Battery
3	R G R G _ _ _	Overheated Battery
4	R G R G R _ _	Charger AC Voltage Input Incorrect
5	R G R G R G _	External Thermal Sensor Fault
6	R G R G R G R _	Communication Interface Fault
7	G R _ _ _ _ _	Charger Overheated
8	G R G _ _ _ _	Repair Charger Relay Fault
9	G R G R _ _ _	Repair Charger Fault

Charger controls are accomplished through a circular connector that has seven pins, described in Table 7. Moreover, a CAN module with two outputs (CAN_H and CAN_L) is provided with the charger, which is the only device connected to the circular connector.

Table 7: ElCon PFC charger communications circular connector pinout.

Pin	Name	Function/Notes
1	Enable	Enable charging when connected to Pin 3. Disable charging when closed.
2	GND	Communication Ground. Common
3	V+	11 VDC when powered on. Maximum of 50mA.
4	Red LED	Cathode of Red LED connects to Common.
5	Green LED	Cathode of Green LED connects to Common.
6	RX	Serial in for factory setup.
7	TX	Serial out for factory setup.

Finally, Orion recommends having an analog shutoff for the charger in addition to digital communication through the CAN bus. In most cases, the BMS will use CAN signals to start and stop charging; however, if there are errors or the bus locks up, the BMS controls a relay that can remove power from the charger.

2.5.8 BMS Controls and Communications

2.5.8.1 *Controller Area Network*

There are numerous systems available that foster communication between discrete electronics, subsequently allowing for streamlined operation. The Controller Area Network (CAN) is a bus standard used in vehicles by which devices can communicate without a host computer. For its application in the GEM, there will be four interconnected CAN devices: Orion BMS, ElCon Charger, Orion Basic Display, and a CAN bus to Universal Serial Bus (USB) adapter also manufactured by Ewert Energy Systems. In regards to the two devices not discussed prior, the Orion Basic Display module receives information regarding the state of charge of the battery, if the BMS is reporting an error, and if power output is being reduced. The CAN bus to USB adapter, or CANdapter, provides a link to a computer so that the Orion BMS can be programmed and data can be retrieved. The BMS can communicate across two CAN buses, labeled CAN1 and CAN2, but can only be programmed using CAN1. Any devices connected to the BMS by CAN must share the same ground, which is the 12 VDC chassis ground. All messages on one CAN must use the same baud rate, which is the speed at which messages are sent. However, the baud rate of CAN1 can be different from CAN2. Unlike the BMS, the charger may only connect to one CAN and the baud rate must be set to 250 kilobits per second (kbps). This also happens to be an automotive standard and the rate recommended for the CANdapter.

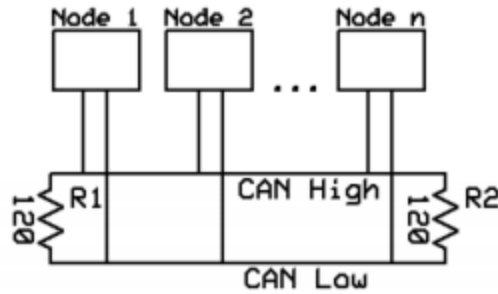


Figure 14: Diagram depicting 120 Ω resistors terminating the CAN bus and how multiple devices on the bus act as nodes [29].

Each CAN connection consists of an insulated twisted pair of wires with one wire representing CAN high and the other representing CAN low. Both ends are terminated with a 120 Ω resistor connecting the high to the low, as depicted in Figure 14. However, CAN1 is terminated within the BMS so only one resistor is needed for that network while CAN2 requires two external resistors. CAN1 originates at the BMS Main I/O connector as shown in Figure 11; pins 17-19 are connected to the CAN1 Shield, CAN1 high, and CAN1 low in that order. Each device on the network comprises a node and has a physical connection between its CAN high (CAN_H) and CAN low (CAN_L) pins and the respective high and low wires of the CAN. If the twisted pair remains insulated and correct terminations are used, the twisted pair can be up to 100 m long. However, the distance between the twisted pair and the device should be as short as possible (i.e., less than 1 m) to minimize interference that could distort the signal.

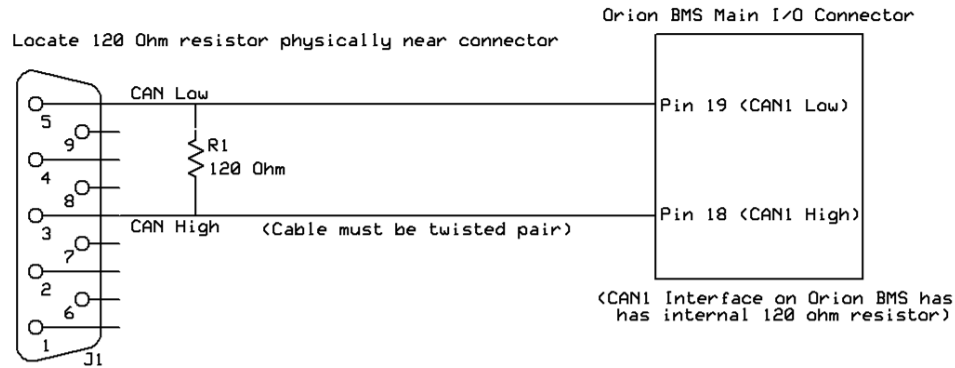


Figure 15: Wiring the BMS CAN1 to a DB9 connector to enable proper function of the CANdapter [29].

Termination of CAN1 with a 120 Ω resistor is recommended to be in propinquity to the connector for the CANdapter. This connector is a D-subminiature connector with a size B shell and has nine pins; hence, the term DB9. The CANdapter has a male DB9 that connects with the female DB9 connector, shown in Figure 15, on which the CAN1_L and CAN1_H taps are soldered on pins 5 and 3, respectively.

2.5.8.2 BMS Digital Controls Round 1

Unfortunately, the EMC used by the GEM is not CAN enabled, meaning alternate methods of limiting discharge current required exploration. Besides CAN, the BMS has a 5 VDC analog voltage output that could be used to scale the discharge limits. For this application, a 5 VDC voltage signal would correspond to maximum discharge current available while 0 VDC corresponds to no discharge allowed. Originally, this analog output was applied to the accelerator of the GEM since it uses a 5 VDC potentiometer to determine the rate of acceleration. However, this method did not work and resulted in error code 05. This error refers to the traction status code -05 in the EMC manual and is displayed on the LCD screen—item “P” in Figure 8 and Table 5—when the voltage at pin 7 of the accelerator is greater than 1.4 VDC

while the voltage at the start switch (pin 3) is greater than 2.5 VDC [13]. Here, the motor controller is programmed to supply the pedal 4.3 VDC and it determines current output to the motor based on the voltage drop over the variable resistance in the accelerator. Therefore, any reduction in voltage from the 4.3 VDC supply expected by the accelerator would be further lowered as the voltage drops on the potentiometer. In combination, the motor controller would not be able to determine how to accelerate properly. Moreover, the accelerator pedal ground was not shared with the BMS ground; thus, the voltage could not be accurately calculated.

Since neither of the methods of limiting current worked, the BMS would need to control the discharge rate through an on/off signal, like the redundant control the BMS has on the charger. One approach would avoid cutting off power to the entire vehicle by adding a BMS-controlled normally open (NO) relay in series with the switch of the main contactor. Aside, the term contactor is generally used in place of relay when the current being switched is large.

Unfortunately, cutting off the power resulted in the same error code as before because it was seen as a start switch error. The EMC recognized the accelerator was depressed and the coil of the main contactor was powered, but the switch of the main contactor remained open and the EMC did not see the switched HV as expected. Therefore, the EMC cannot detect if the main contactor coil is powered, but since the accelerator pedal is down, the vehicle expects that the start switch is defective. Instead of interrupting the switch of the main contactor, the start switch wire connected to ground was interrupted. When the accelerator is depressed, a switch inside the accelerator is closed, connecting pin 3 from the EMC to the HV ground.

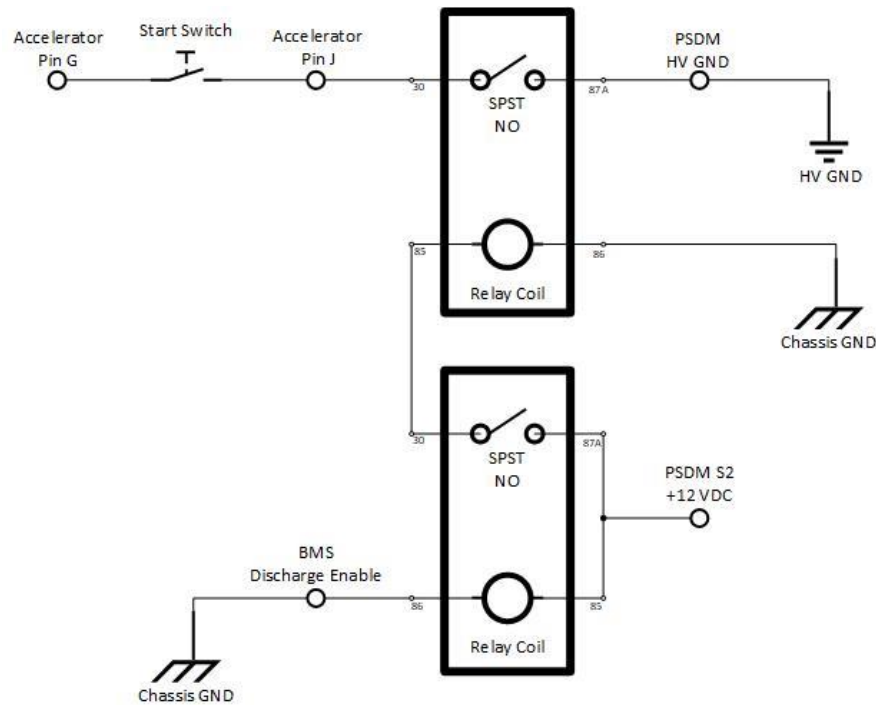


Figure 16: Modified start switch circuit shown. By pulling the Discharge Enable signal to ground, the BMS can close the start switch circuit, thus, when the accelerator is pressed, the EMC receives power for the electric motor.

The start switch circuit used as shown in Figure 16 is different from the circuit recommended and installed by Patrick Collins before originally returning ownership of the GEM to the Center for Sustainability. Using two of the same relays in series can increase the line voltage, but only with AC relays in AC applications. It is possible that one of the relays was intended to control heater usage based on whether the BMS is allowing discharge because the heater can be a significant power draw. When the circuit was recorded, the 12 VDC supply originated at PSDM S2, which should power the heater switch. However, the purpose of the circuit is conjecture because it is not mentioned in any records.

Overall, interrupting the start switch as it went to ground was temporarily successful. However, if the discharge enable signal broke the circuit, then it would not reengage until BMS power had

been cycled. Here, the BMS was not originally intended control a vehicle in this manner, but after communicating with the BMS manufacturer, Ewert Energy Systems, the BMS program was revised to reset the discharge enable signal after a desired delay period. As a result, the GEM could be driven and the BMS acted to limit the discharge current using the configuration shown in Figure 17. While temporarily functional, once the vehicle was returned (see next section) there was another error affecting the accelerator and start switch circuit. This error likely happened because of the change from the circuit presented in Figure 17 to Figure 16.

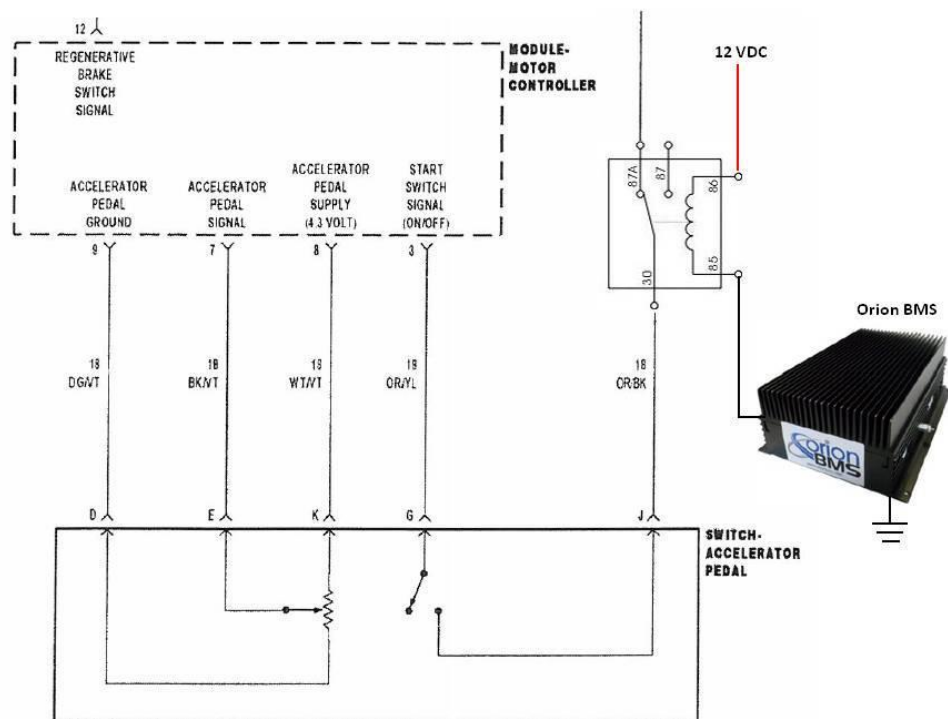


Figure 17: Revised start switch circuit installed in the GEM by Patrick Collins [7].

Once the GEM had ceased to function any longer, the GEM was offered back to engineering students to repair and revise the upgrades with the intent to return the GEM to the Center for Sustainability in working order.

2.6 Repairs and Battery Management Round Two

2.6.1 Discerning Problem

Repairs and improved functionality were again sought regarding the 2007 GEM eS. While back in the ownership of the KU Center for Sustainability, the vehicle stopped functioning. Inspection of the battery voltage made it apparent that the batteries were the inhibiting factor. It was not clear how the batteries were damaged. However, regardless of whether it was environmental conditions or if it was poor battery management, the focus was ensuring that once the vehicle became operational again that there would be safeguards preventing a similar failure from occurring.

Based on verbal account of the vehicle usage and conditions leading to failure, the cause of battery failure could be theorized. Since the vehicle was left outside during the Kansas winter, it seems plausible that the batteries were damaged beyond repair due to the cold. Unbeknownst during construction of the first battery pack, LFP batteries can be critically damaged by charging in below freezing conditions [18, 31]. Given that a few batteries were perfectly healthy while others were completely discharged, this suggests that the cells used could have been mismatched, unbalanced, or that there were large temperature gradients within the battery pack. Specifically, since temperature can have a significant impact on the health of the cell, when cells are at different temperatures, they will age differently [32]. Therefore, if the BMS allowed the cells to be charged at below freezing temperatures, settings would need to be revised and the mode of enforcing BMS regulations would be changed. Additionally, it is feasible that BMS settings could have allowed the batteries to be drained inadvertently.

While the main premise during the second round of vehicle repairs was improved battery management, assembling a new battery pack and troubleshooting miscellaneous vehicle errors was a prerequisite to testing the functionality of a new battery management method.

Unfortunately, the manufacturer of the 40 Ah cells, CALB, had discontinued that product; hence, replacement batteries for the original battery pack could not be procured. In addition, mixing old and new batteries would have created a greater challenge for the BMS since the batteries would be at different stages in their lives. Specifically, while many of the original cells maintained their voltage and seemed reasonably healthy, they would have not been matched to within the desirable 3% variance in capacity [15]. As a result, 24 of the 60 Ah batteries manufactured by GBS were purchased and this required a new pack to be built while additionally changing the BMS settings.

2.6.2 Second 60 Ah Lithium-Ion Battery Pack

The GBS cells have a slightly different cathode material, lithium iron manganese phosphate (LiFeMnPO_4 or LFMP). Since the voltages of the 60 Ah GBS cells are similar to the CALB cells, this new pack would again contain 24 cells. Unlike the CALB cells, which have one hex cap screw per terminal, the GBS cells have four screws per terminal that are tightened using a 2.5 mm hex key. Specifically, eight M4 10×0.7-4 mm body diameter, 10 mm length, and 0.7 thread pitch-button head socket screws were provided per cell. Accounting for the increased size of the GBS cells, a new case would need to be constructed. Standing upright, the 60 Ah cells have a base 126 mm long × 65 mm wide, or approximately 12.7 in² and 7.1” tall. However, to minimize outgassing and associated expansion of the cells, the batteries are strapped together in groups of four, as shown in Figure 18. Two interconnected aluminum plates are included on each

5" × 7.1" face with aluminum straps screwed into each plate, subsequently holding the batteries together. Originally, the groups of four cells each had a pair of white holding cords while manually moving the group (Figure 18); however, these cords were removed before constructing the battery pack.

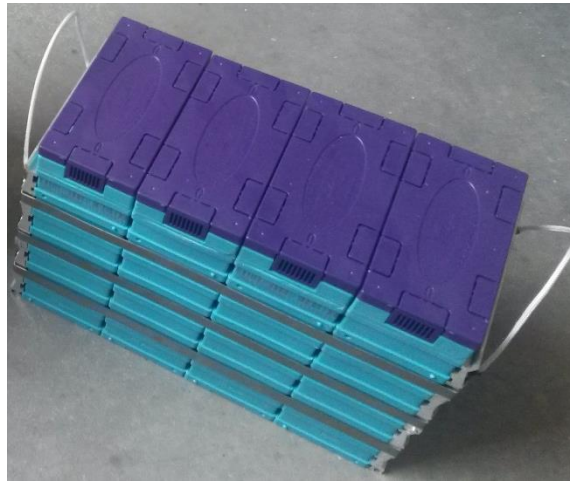


Figure 18: Four 60 Ah GBS batteries strapped together with aluminum plates at either end and three aluminum straps on either side. Purple caps impede the ingress of dust and water droplets, but also prevent foreign objects from falling between terminals and causing a short circuit.

Expectedly, the larger 60 Ah batteries weigh more than the 40 Ah batteries. At an average 2.1 kg per 60 Ah cell, the combined weight of the 60 Ah cells is 50.4 kg, or about 111 lbs., which is roughly a 40% increase in weight over the CALB battery pack. Overall, three boxes were made for the 60 Ah pack as the battery layout shifted. Neither of the first two box designs incorporated enough space for the aluminum plates; here, it was incorrectly believed that the box itself would prevent expansion of the cells.

2.6.2.1 Steel Battery Box

Originally, eighth inch scrap steel (donated by Fleet Paint Specialties) was used to construct the box; however, this material was nearly as heavy as the batteries themselves. Thus, the steel box was, in retrospect, prohibitively heavy. This design iteration functioned insofar as it provided a means of transporting the batteries between the workbench and the vehicle. Five steel sheets were welded on the inside seams to form the box. Another issue with the metal battery packs was the need for electrical insulation between the batteries and the pack. Should anything fall between an electrode and the battery box, the box should resist against harmful electric shock. Therefore, a rubberized coating was applied to electrically isolate the batteries from the vehicle and anyone handling the pack. Despite sanding the metal before applying a rubberized coating to the metal battery boxes, abrasive or sharp contact easily removed sections of the coating.

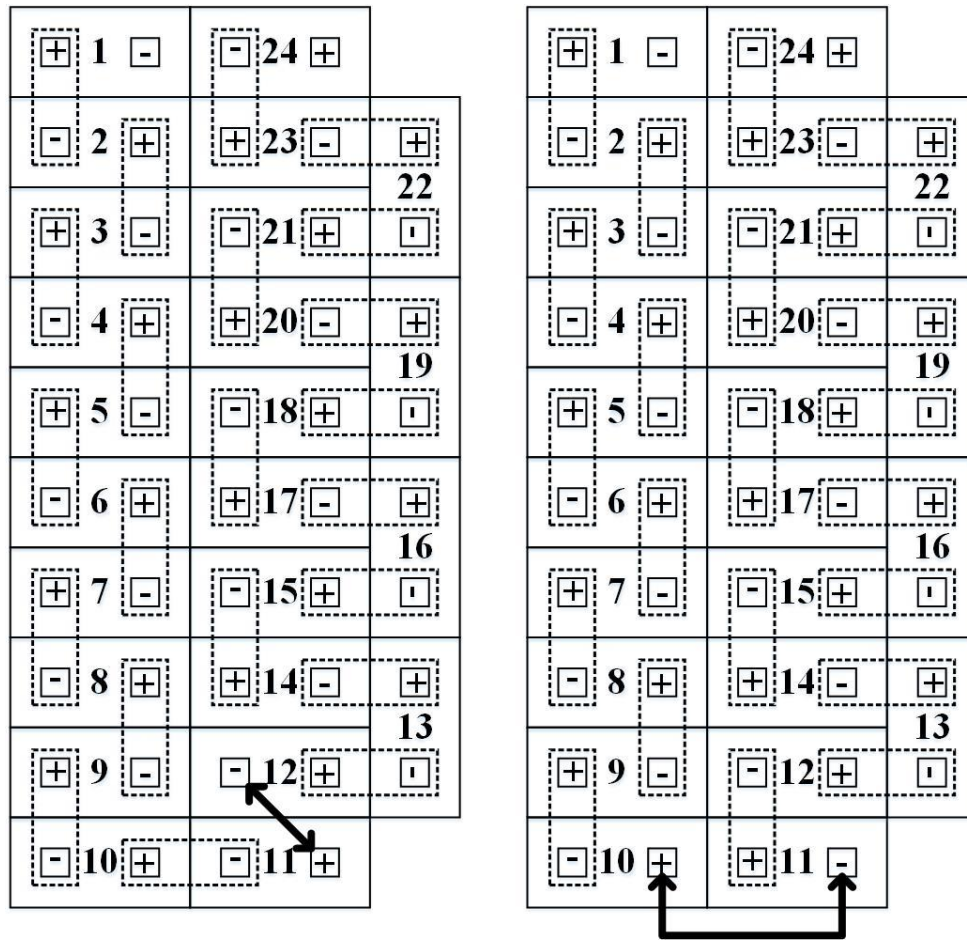


Figure 19: Two cell configurations considered for the steel battery box. Left configuration was ultimately chosen. Busbar connections are represented by the dotted rectangles. Connector between cells 11 and 12 on the left, and 10 and 11 on the right would need to be fabricated in-house.

Anticipating clearance issues when removing the 60 Ah battery pack, the two cell configurations in Figure 19 were proposed to maximize the width of the battery pack to reduce its length. In addition, maintaining the position of the battery box handles on the leading and trailing faces was intended to make the battery pack removal procedure the same as the original 40 Ah battery pack. Consequently, the first 60 Ah box was too wide to accommodate handles on the sides. For this box, a handle on the leading face would be displaced by the rectangular section removed, shown in Figure 20, to provide room for battery connections. Connectors in contact with the

battery terminal are parallel to one another and fastened into place to prevent breaking contact. The top edge of the battery box ought to be above the cells and their connections to inhibit contact between the underside of the vehicle and the batteries. Hence, removing the rectangular section is warranted. Per Figure 19, the battery pack negative and positive terminals are on the leading face of the battery pack and are located roughly in the middle. In order to move the battery pack, towing straps were used instead of rigid handles.



Figure 20: Steel battery box for the 60 Ah batteries.

Four slots were cut out of the box on both the front and rear, mirroring one another. These slots were placed approximately one inch from the top and bottom on both left and right sides.

Towing straps were drawn through the slots on each side, along the bottom, and through the slots on the rear face with enough excess at the front and rear to extend above the pack and be knotted, subsequently forming two loops. An added benefit to the towing straps is the lessened drag

between the straps and the aluminum drawer as opposed to plastic-coated steel against aluminum. The battery box with towing straps installed is seen in Figure 20.

Unfortunately, the steel battery box was nearly the length of the battery drawer and the drawer cannot extend its full length past the vehicle due to the C-channel ending before the bumper. Thus, the steel box could not be lifted straight out of the battery drawer. Therefore, to withdraw the original 60 Ah pack without tilting it, the rear wall of the battery drawer was removed, cutting along the weld seam. Afterwards, the wall was reattached with two hinges on the bottom edge, allowing the aluminum plate to swing downwards so that the battery pack could be scooted backwards and then hoisted up. Furthermore, two locks were installed onto the rear wall of the battery drawer—one on each side—to keep the wall vertical and to prevent the battery pack from sliding out the rear of the vehicle.

Just as with the 40 Ah pack, the cells are all in series although the arrangement is different. Each cell has a cell tap on its positive terminal, while cells 1 and 13 have additional cell taps on the negative terminals. Besides the connection between cells 11 and 12, copper busbars provided with the cells were used to connect the battery in series, as shown in Figure 19. However, rather than use a cable to jump from cells 10 to 11, a busbar was made as shown in Figure 21. This busbar has a low profile, as opposed to the cable, and has a similar resistance as the copper busbars.

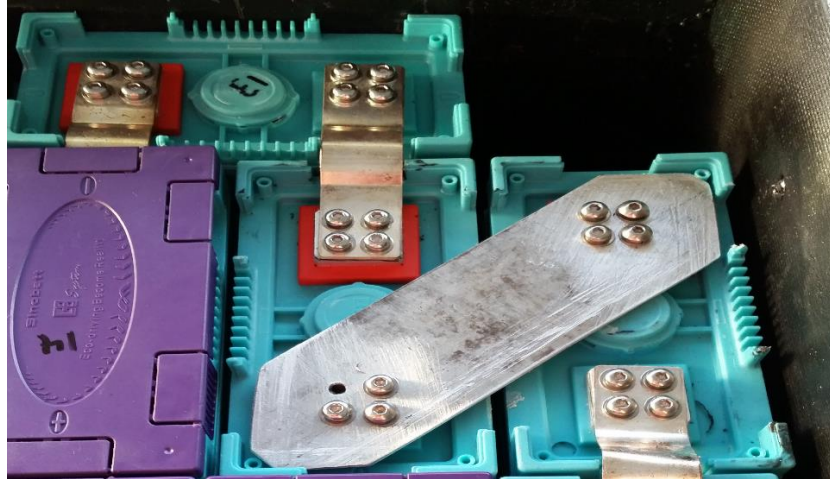


Figure 21: Prototype diagonal busbar cut from aluminum.

2.6.2.2 Aluminum Battery Box

While rewiring the BMS cell taps, the steel battery box was taken out of the vehicle so that the cell taps could be disconnected. Since a lighter battery box was desired, removing the steel battery pack represented an opportunity to construct a new battery box. Additionally, the new design was intended to incorporate sturdier handles on either side of the battery pack. Once enough eighth inch scrap aluminum was located (also donated by Fleet Paint Specialties), a second box was built that required two individuals to carry it. One sheet of eighth inch aluminum was bent to form the bottom, sides, and upper flanges, as shown in Figure 22. A second aluminum plate was welded onto the body of the battery box, sealing the distal face. Since the cell configuration for the aluminum battery box, shown in Figure 23, was slimmer than in the steel battery box, there was room between the aluminum battery box and the walls of the battery drawer for battery box handles. However, the available room for handles would not accommodate the style of handles used on the 40 Ah battery box (i.e., drawer pull shown in

Figure 1). Alternatively, hanging drawer pulls were installed, two on each side and one inch from the top of the battery box.

While lighter than the steel box, the aluminum box was still too heavy to be comfortably lifted using the two handles installed on either side of the box. Unfortunately, given the weight of the aluminum box and batteries, pressure along the thin handles was painful. Moreover, while the handles of the battery box may fit within the allowed space, there was oversight regarding the clearance necessary to accommodate hands to grasp and remove the box. Again, bearing the weight in mind, each hand will likely need to make a fist to achieve adequate grip on the handle. Thus, it can be expected that the minimum clearance required on either side is the length between the dorsal side of the hand and the second finger joints. Realistically, however, the minimum clearance would not be sufficient because interference between the hand and the battery drawer ought to be avoided outright. Similar to the steel battery box, towing straps were drawn through the handles to increase and soften the surface area in contact with hands.

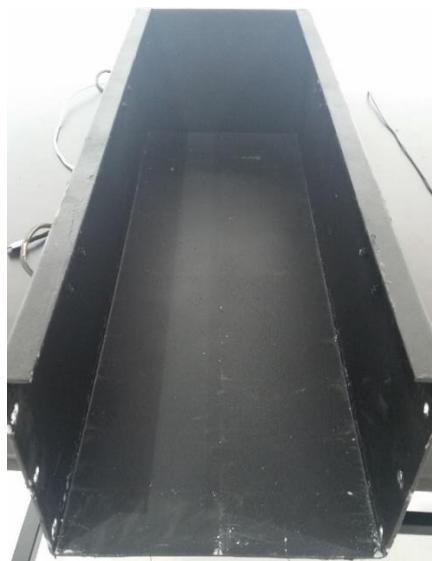


Figure 22: Aluminum battery box.

Furthermore, additional issues became apparent while placing the cells into the box and connecting them. The flange element of the design, while functioning as intended by inhibiting vertical movement of the batteries, made installation and maintenance of individual cells more onerous. To remove the cell in question, every cell before it must be detached. Moreover, the flange extended too close to the cell terminals. In addition, while all sections of the box were coated in a resistive coating, the coating could be easily removed. Since the terminals were close to the flange, there was some risk of contact between the flanges and the hex keys used to tighten the battery terminal bolts. Additionally, the open front face of the second 60 Ah pack, which secured the batteries using two horizontal aluminum straps, did little to prevent further expansion of the cells due to gas formation. For instance, not long after installing the battery pack, expansion was becoming noticeable on the larger face of select batteries, and gaps were appearing between the cells. Unfortunately, a third battery box would need to be built and the batteries themselves would again need to be constrained by the aluminum plates and straps.

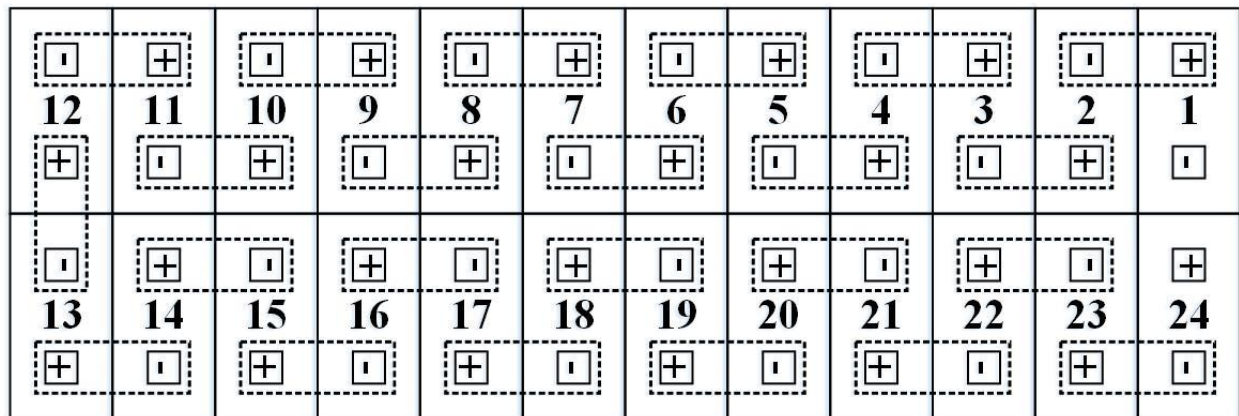


Figure 23: Cell configuration for the aluminum battery box. Busbar connections are again represented by the dotted rectangles.

2.6.2.3 Third Iteration 60 Ah Battery Box

The potential for harm due to electric shock and other issues with the first two battery packs, as well as the need to rectify the battery cell expansion issue, led to the construction of a third box made from half inch wood as shown in Figure 24. Just like the first two boxes, the wood box was spray-painted black. However, unlike the first two boxes, this box was constructed with enough room for the aluminum compression plates and straps.



Figure 24: Third iteration of the 60 Ah battery box, constructed of wood. Batteries were not yet connected for this photo.

Like with the aluminum battery box, carrying the battery pack from each side also simplified the removal and installation processes. In specific, no longer would the battery pack need to be pulled partially out of the battery drawer before the second carrier could grab the handles or straps. However, the battery box would still need to be shifted backwards before lifting due to

the length of the battery box. Lastly, the straps on the wooden battery box were made shorter than those that had been on both the aluminum and steel battery boxes. When the loop made by the straps was too large, it became difficult to transport the battery pack from the relatively low battery drawer to the work bench. In addition, shorter straps reduce the how far the battery pack can sway when being carried; thus, allowing those carrying the battery pack to have better control. As a result, the third battery box has two loops of tow straps that are securely fastened at the bottom of the box using heavy duty staples and come up around the sides of the box so that it can be carried by one person on each side. Moreover, six nylon chair glides were hammered into the bottom of the wooden box so that the staples would not scratch workbench surfaces and minimize the likelihood that the staples snag and are pulled out.

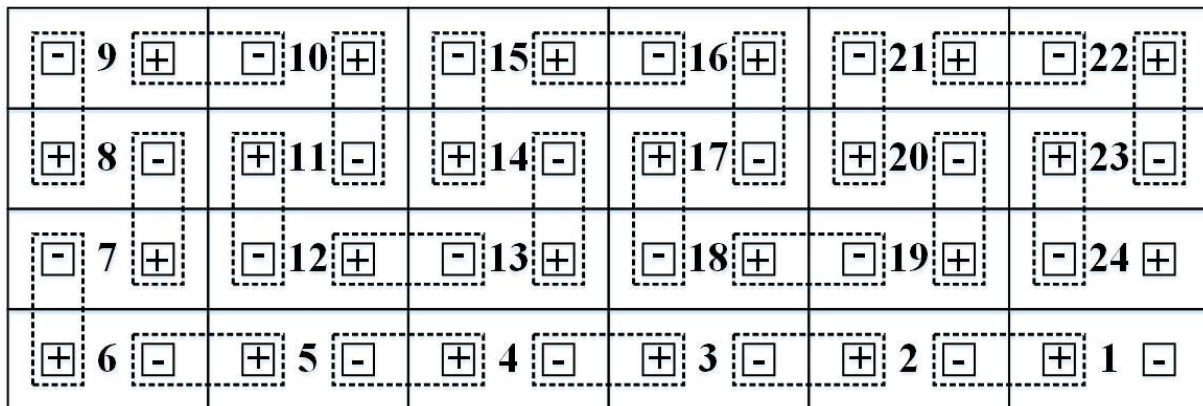


Figure 25: Cell configuration for the wood battery box. Each column (i.e., cells 1, 22, 23, and 24) are pressed together by aluminum plates and straps. Thus, no individual cell can be removed, but must instead be removed as part of a four-cell unit.

Since the cells were strapped into groups of four, the configuration of the cells within the battery box was changed, which may be seen in Figure 25. Just as before, cells 1 and 24 must remain at the front of the battery pack so that the battery pack positive and negative terminals are close to the vehicle power connector cables and may be easily reached through the access point labeled

as object 3 in Figure 3. Insofar as the layout of the BMS cell taps, there were no changes made. However, the wires on the battery pack side of the circular connector were replaced with more pliable wires during the change from the aluminum battery box to the wood battery box. Furthermore, the provisional terminal connectors from the vehicle were replaced with heavy duty power connectors, part number 6800G1 from Anderson Power Products. Two pairs of heavy-duty power connectors are used: two larger connectors connect the battery pack to the vehicle while the smaller pair connect the battery pack to the charger, as shown in Figure 26.

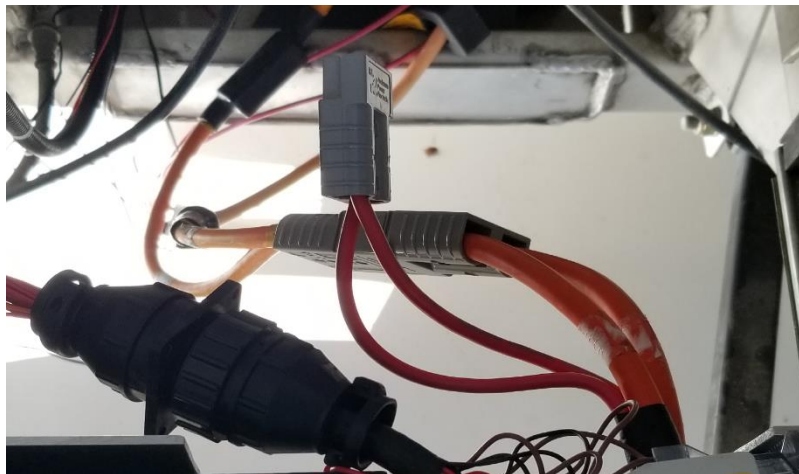


Figure 26: Heavy duty power connectors and circular connector attached to the battery pack. Uncoupled heavy duty power connector is for the charger while the coupled heavy-duty power connector links the battery pack to the vehicle. The black connector in the bottom left is the circular connector for the BMS cell voltage taps.

2.6.3 Troubleshooting

2.6.3.1 Start Switch Circuit

Once the GEM wiring was fully connected and the 60 Ah battery pack had been installed, it was possible to begin troubleshooting. All 12 VDC accessory systems were functional upon the initial startup of the GEM. However, an error code was displayed on the dash LCD. The same

error code that was shown during the initial installation of the BMS controls was again the issue: error 05. Since the relays (installed on the OR/BK wire connecting pin J of the accelerator to PSDM 72 GND post) interrupt the start switch circuit, this was a possible issue to investigate. However, by not initially understanding the functionality of the relay pair (Figure 16) and instead trusting the work of previous students, the investigation started with the accelerator. Since the accelerator houses the start switch, and error 05 is a condition where the start switch is not closing properly, the accelerator may not be functioning properly. Additionally, it is important to note that the drive mode switch is functional because it is displayed on the dash and designating reverse triggers the reverse lights and buzzer. The corrective action suggested by the printed repair manual is to review the motor controller circuit diagram and confirm that this segment is wired correctly. By removing the relay pair from the vehicle and reconnecting the GEM as it was originally, though sans charger, the error remained the same.

Here, the start switch functioned correctly, meaning that there was no conductive path while the accelerator was up. Hence, once the accelerator was pressed down, the switch closed and allowed current to flow between pins G and J of the accelerator. Since the start switch seemingly worked, the accelerator potentiometer was tested to verify if it had the same resistance values as the manual states. Per the maintenance manual, while measuring across pins 7 and 9 of the EMC connector (CH1), the resistance should be approximately $3000\ \Omega$ with the accelerator up and ought to steadily decrease as the accelerator is pushed down. When fully depressed, the resistance across CH1 pins 7 and 9 ought to be approximately $80\ \Omega$. Overall, the resistance across CH1 pins 8 and 9 should always remain about $3000\ \Omega$. If there was no continuity between either pin 7 or 8 and 9, the resistance would be too large, possibly resulting from broken contact

with the potentiometer or mis-wiring of the circuit. If the opposite case was true and the resistance value was always relatively small, then there may be a short circuit.

Considering the wiring harnesses and connectors come from the vendor pre-made, and the accelerator circuit had worked before, the accelerator seemed to likely be the cause. The actual resistance measured from CH1 pin 7 to 9 was significantly higher than the recommended value while the accelerator pedal was pushed down. Since the accelerator pedal is relatively easy to replace, a new pedal was purchased and installed. The new resistance of the potentiometer was $3996\ \Omega$ while the accelerator pedal was up. Unfortunately, even with the new accelerometer, error code 05 was still present. After removing the BMS control relays from the circuit and replacing the accelerator, the accelerator connection to ground was confirmed.

Since the BMS control relays interrupted the wire going to ground, that could have been an issue. Additionally, there was some concern that the regenerative braking wire was somehow affecting the start switch since the printed manual shows they intersect before going to the PSDM -72 post. However, removal of the regenerative braking switch opens that section of the circuit and does not interfere with the start switch wiring in the vehicle wiring. Although, shortly after ensuring the start switch jumper connected to ground, an emergency brake warning was noticed on the LCD display. However, the start switch issue took precedence. The next most likely cause of the start switch error would be the EMC.

2.6.3.2 Replacing the Motor Controller

Since the EMC is an expensive component, it would be prudent to consider other options before replacing it. One related issue was that the main contactor—a solenoid—was not closing when the accelerator was pressed. It is likely that the EMC closes the contactor when it receives the

signal from the accelerator to do so; however, it was not difficult to check the functionality of the main contactor. The main contactor has two bolts that hold it in place on the back side of the PSDM along with four electrical connections: two for powering the coil and two connected to the contacts. After disconnecting and removing the main contactor from the vehicle, the contact areas were disassembled and lightly sanded to remove superficial corrosion; thus, improving conductivity. Then, the main contactor was reassembled and connected to a power supply. Before activating the main contactor, it was confirmed that there was isolation between the two sides. Typically, this solenoid's coil is powered by the key switch output at 72 VDC and limited by fuse F13 to less than 10 A. Here, current does not flow through the solenoid coil until the EMC lowers the electrical potential of the EMC pin 17, labeled main contactor control. Outside the vehicle, the voltage supplied to the solenoid coil was lower than what it would see while in the GEM. Fortunately, the solenoid closed when power was supplied. Unfortunately, this was the last device that could have reasonably caused the error, save the EMC itself.

With the previous explanations exhausted, it appeared that the EMC was malfunctioning. This presented two options, keep the same type EMC or purchase a new EMC, preferably one capable of communicating with the BMS through CAN or at least OBD-II. The first option would require either purchasing a new EMC or having the current EMC fixed; purchasing a new SX Transistorized Motor Controller from a GEM vendor would have costed \$1029.99 and remanufacturing it through Flight Systems Industrial Products would have costed \$353. In comparison, there were some new EMCs costing less than the remanufacturing price that were seemingly more capable of communicating with the BMS. To meet system requirements, the motor controller would ideally run on DC electricity at 72 VDC nominal and could be limited to

draw only 100 A. Moreover, the GEM uses a shunt-series wound DC motor rated for 5 HP and 4100 RPM with the motor armature and field rated for 56 A and 10 A, respectively. Based on these specifications, the Kelly KDZ72200 motor controller was purchased.

When programming the Kelly KDZ controller, there was a concern that a reverse contactor would be needed. Since a reverse contactor was not used by the original EMC, there was some apprehension towards purchasing one. Moreover, the original EMC wiring diagram, shown in Figure 27, and the printed manual highlight that the motor armature supply and field supply are separated. For this reason, along with the potential need of a reverse contactor, it seemed that the Kelly KDZ controller would not work with this motor. In addition, the original EMC has a significant role in other vehicle functions, of which it is not ostensible that another EMC may be suitable. For example, error codes generated by the original EMC along with drive mode and vehicle speed are displayed on the LCD. Hence, it was not apparent how these commodities would be replaced by a different motor controller. Overall, the PSDM and ECM are interconnected and the vehicle's functionality revolves around these two parts.

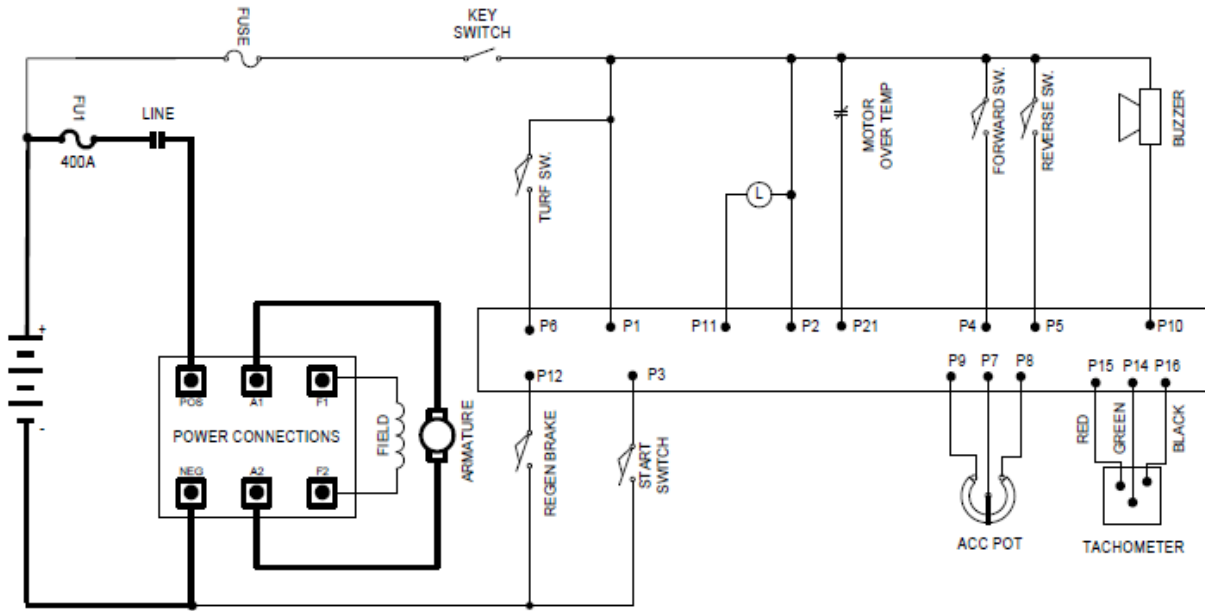


Figure 27: Standard drawing for original motor controller connections in NEV applications. [13]

After returning the Kelly EMC, the original EMC was sent to the company Ride-4-Fun that serviced and updated the EMC. Not long after sending the EMC away to be repaired, another setback befell the GEM. Unfortunately, while tightening connections at the 72 GND post of the PSDM, the bolt holding all the connectors snapped.

2.6.3.3 Repairing the PSDM

The PSDM is where battery pack current enters the vehicle and is distributed to subsystems. Initially, the BATT- and 72 GND posts may appear to have the same purpose and one is redundant. However, the BATT- post is always at a lower voltage than the 72 GND post because there is a shunt resistor between the two, allowing for an accurate measurement of current through the vehicle. Since the negative terminals of the PSDM are the last points within the vehicle before battery current returns to the negative terminal of the battery pack—besides the

leakage current through the suppression Schottky diode and current directed to the BMS and associated electronics—all vehicle current passes from the 72 GND to BATT- posts.

Unfortunately, the nature of the electrical connection makes these posts susceptible to breaking.

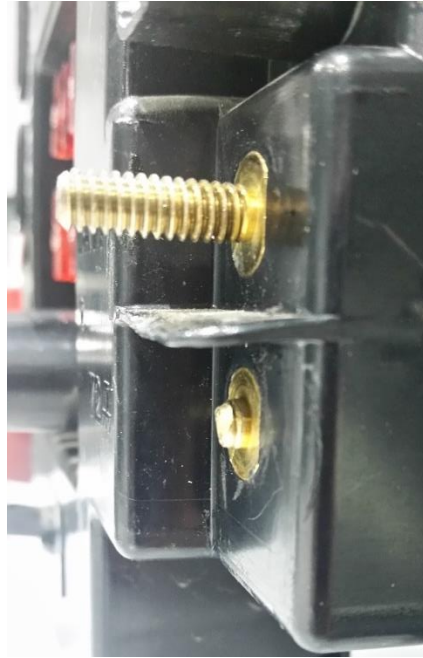


Figure 28: Photo juxtaposing the BATT- PSDM post to the remaining segment of the 72 GND post after snapping.

Electrical resistance is decreased by increasing the cross-sectional area the current is flowing through; hence, ring terminal connections have more contact area when tightly pressed together. While ring terminal contact areas are primarily longitudinal with the post, the associated wires extend laterally from the post. Furthermore, access to the post for electrical connections is diminished by the wall separating BATT- and 72 GND—to prevent short circuiting—and the elevated face of the PSDM. Since not all wires connected to the 72 GND expect the same electrical current, the wire gauges and ring terminals vary. In addition, space limitations force ring terminals to be stacked, which are then bent to keep the ring terminals pressed together but

also make room for the wire egress. Therefore, maintaining electrical contact under those conditions requires tightening the nut holding the terminals in place. Repeated fastening and unfastening of the nut and lateral loads from tension along the wires inevitably resulted in the bolt weakening until the bolt finally snapped under tension. Afterwards, only a small segment of the bolt remained connected to the PSDM, shown in Figure 28.

The remaining thread on the 72 GND post was insufficient to firmly grasp a coupling nut so that another bolt could be attached to extend the length of the post. Since the post is permanently attached and extends into the PSDM, the entire PSDM would need to be replaced. Regardless of whether the PSDM post is fixed or replaced, the PSDM would need to be removed from the vehicle. By removing the PSDM from the vehicle, the 72 GND post could also be accessed more easily. First, the ring terminals were disconnected from the PSDM high voltage posts. Then, the wiring harnesses were disconnected from the PSDM. Since the MDS is latched onto the rear face of the PSDM, the ring terminals fastened to the MDS were disconnected, as well. The PSDM is bolted onto a metal bracket which holds the PSDM away from the cabin wall—through which the front, controller, and DCDC harnesses pass. Additionally, the recessed space behind the PSDM bracket houses the main contactor, the heater blower, and the heater coil. Four K-lock nuts fasten the PSDM to the metal bracket. Although, because the contents of the PSDM were unknown, the bracket was removed alongside the PSDM.

Before resorting to replacing the PSDM, there were attempts to fix the 72 GND post. The initial effort to bridge the 72 GND post to a threaded rod employed solder melted at the base of the 72 GND post to reinforce the connection between the 72 GND post and a coupling nut. However, the solder would not readily adhere to the metal. Moreover, concerns of further damaging the

surrounding plastic PSDM face or risk of weakening the electrical connection prompted the disassembly of the PSDM and subsequently, considerations of other possible solutions.

Upon opening the PSDM, it was found that the printed circuit board (PCB) is connected to the three PSDM posts by small bolts. Each of the three bolts are thread through the PCB and into their respective PSDM posts. This discovery complicates the matter of replacing the 72 GND post. After collaboration with Ash Shadrack, a research technologist at KU, it was decided that the 72 GND post should be replaced in entirety with a new threaded rod. To prepare the 72 GND post replacement, a 1/4-20 × 2” zinc threaded rod was procured. Next, the end of the rod meant for the inside of the PSDM was drilled and tapped for the smaller internal bolt, seen in Figure 29.



Figure 29: Photograph from within the PSDM of the 72 GND (left) and BATT- (right) posts after installing the new 72 GND post. Neither post may be safely removed from the PSDM, though, the extant zinc base was sufficiently wide enough to support a new zinc rod.

As for the PSDM cover, a 13/64” drill bit was used to drill a hole through the original 72 GND location in the PSDM. Then, the 13/64” hole was tapped for a 1/4-20 bolt. After ensuring that the internal bolt threaded properly, the PSDM end of the zinc rod was coated in a thread-locking fluid and threaded into the PSDM. Electrical contact between the zinc base of the PSDM 72 GND post and the 72 GND post itself is not required, though preferred because it increases the

contact area shared between the aforementioned post and the ring terminals connected thereon.

In addition to the thread-locker adhesive, the edges of the zinc base in contact with the post were clipped—hence the radial marks shown in Figure 30—to further safeguard against the post being dislodged from the PSDM.

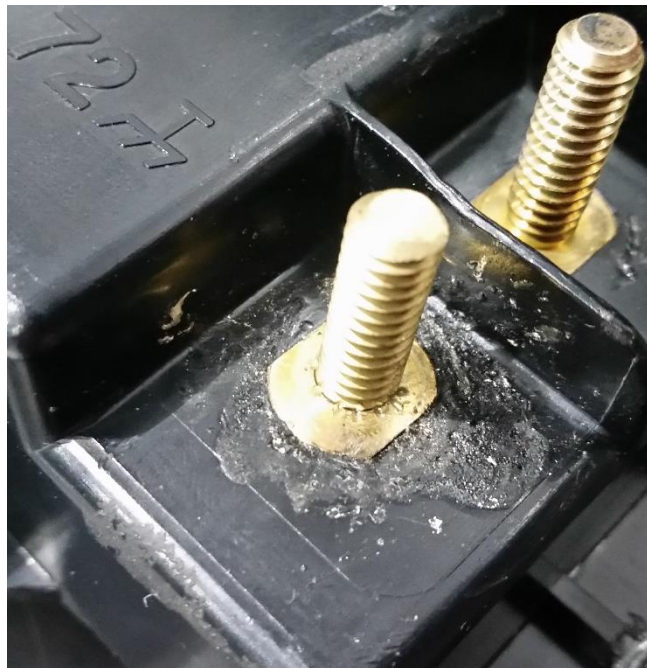


Figure 30: External view of the 72 GND post after repairs were made. The bolt is a different size than the original. Damage to the plastic resulting from attempts to solder the coupling nut are visible around the post. Marks from clipping the metal extend radially from the post.

Once the PSDM was repaired, it was reassembled with the PSDM bracket and bolted back in place within the GEM. Even with the PSDM in place, it was not until the EMC was returned from Ride-4-Fun that work resumed on troubleshooting the GEM.

2.6.3.4 Wiring and Brakes

Unexpectedly, the company reported nothing wrong with the EMC. When provided the context of the problem regarding error code 05, they suggested rechecking the motor controller wiring based on the software version. For older software options (i.e., GL5K or lower), modifications would not be necessary since the EMC does not have brake switch software. However, newer versions (i.e., GL5L or higher) require a wire jumper from CH pin 13 to BATT- for vehicles that do not have a brake switch installed. Otherwise, vehicle operation is suspended and error code 04 will be shown on the dash. Since the GEM has an emergency brake switch but this switch is not connected to the motor controller through pin 13, one must be added.

Instead, this wire jumper was not installed immediately because it was possible that the cause of the start switch problem was within the motor controller harness (CH). Replacing the CH would better ensure the integrity of the wire connections and reset the wiring back to its original state. Given the discrepancies between various manuals, notes on the vehicle, and the state of the vehicle itself, it was considered helpful to step through reconnecting the CH to enable better wiring documentation. However, it is prohibitively expensive as a single CH was cited to cost approximately \$300 if purchased from Powersports of Joplin. Instead, a CH was purchased on EBay and once installed it uncovered more inconsistencies between the maintenance manual and the actual vehicle hardware.

2.6.3.5 Charger Interlock

After the CH was installed, the GEM began showing it was charging whenever the vehicle was on. While the GEM is in charge interlock, for safety reasons the vehicle cannot drive, but it also was not showing error codes. Although the original lead-acid charger was disconnected, the

vehicle still expected a charger interlock signal. By simply leaving all wires that were connected to the QuiQ charger disconnected, the GEM was set in charger interlock mode; thus, it was unable to move or even display error codes related to the drive components. By connecting the charger interlock wire—DG wire on the FH that connects PSDM J1J to the HV GND—the vehicle will no longer enter charger interlock mode. Unfortunately, this would become an issue should any charger need to communicate charging status to the vehicle in the future. However, since the BMS ultimately decides whether the batteries are capable of discharging or if they can allow charging, the ElCon charger only communicates with the BMS. Currently, it is the role of the Orion BMS to shut down the vehicle while charging. The methodology of the Orion BMS in determining charger interlock mode is described in Chapter 3.

2.6.3.6 Parking Brake

Before repairing the EMC, the parking brake warning light showed on the LCD display regardless of parking brake engagement. As this had occurred before replacing the EMC, it was not likely an issue with the EMC. Usually the wire colors and connections described by the maintenance manual are correct but there are discrepancies between the digital copy of the GEM wiring diagram, the printed diagrams used by KU Facilities Services, and the actual vehicle wiring. The Charging System diagram of the printed maintenance manual shows an OR/DG wire connecting PSDM J6G to the parking brake. Several pages later, the Rear Lighting diagram shows an OR/WT wire running between a terminal of the parking brake and PSDM J6H. Both the OR/DG and OR/WT wires are shown to connect to the COM terminal of the parking brake according to the diagrams, but that should not be the case. Parking brake wiring in the 2005-2010 GEM service manual show the exact same configuration but the OR/DG wire is just DG and the

OR/WT wire is WT/DG, instead. The parking brake switch, a SPDT miniature basic switch model number V-10G1-1C25-K, is located at the rear end of the parking brake handle, and just under the GEM bench seat. While the parking brake is engaged, there is a conductive path between the COM terminal and NC terminal of the parking brake. Within the GEM, the two wires going to the parking brake are TN and RD/WT. Both wires are labeled with orange tape; the tape on the TN wire reads “TOP BRAKE” and the RD/WT wire is labeled “REAR BRAKE.”

Unlike in the parking brake diagrams, the parking brake does not directly connect to PSDM J6. Connector RH1 connects to PSDM J6, but neither pin H nor G are TN or RD/WT. Instead, J6H is OR/VT and J6G is OR/DG. According to the printed manual, the OR/VT and OR/DG wires ought to connect to the battery temperature sensor (BTS). However, the BTS is no longer in use since the BMS measures temperature with separate thermistors. Two automotive relays that were not in any of the wiring diagrams and were never mentioned in prior documentation are located on the passenger side under the dash. Under the dash, there was a four-pin connector with jumpers connecting to J6H, J6G, and two wires to the parking brakes. The mating four pin connector leads to the two automotive relays. It was not known originally if the parking brake was supposed to switch HV or 12 VDC, just that the parking brake is limited to 10 A current. Without knowing the purpose of the two SPDT relays, the simplest path to moving past the problem was to avoid them altogether. Which entailed rerouting the TN wire to connect with the OR/DG wire and the RD/WT wire to connect to the OR/VT wire. Based on the printed manual, when the parking brake is engaged, power is supplied, but the key switch is open, 72 VDC from J6H connects to J6G by means of the parking brake switch. Whereby, the parking brake buzzer is activated. By either disengaging the parking brake or by turning the vehicle on with the key, the

parking brake buzzer can be turned off. After applying this change, the parking brake light was still on.

Contrary to expectations, the parking brake buzzer would still engage as it should: the parking brake buzzer sounds when the parking brake is not engaged, the MDS is closed, but the key is off. If the brake buzzer is an indication that the parking brake is not the issue, then the error may serve another purpose. In Table 5 it is mentioned that the parking brake warning is also illuminated when the brake fluid level is low. The brake fluid level switch (BFLS) is connected to the brake fluid reservoir on the driver's side and under the hood. Manually checking the brake fluid level revealed that the brake fluid level was not low. It seems more probable that the BFLS opens when there is an issue, because then the circuit would draw current. Disconnecting the BFLS does not extinguish the error. As mentioned in Table 3, 12 VDC supplied to the BFLS, the brake pressure switch (BPS), and flashers goes through fuse F6. Fuse F6 is not the issue because the direction indicators are functional, as are the reverse and brake lights. In fact, all the fuses are intact. Pin C from display connector D1 was removed to open the circuit but did not remove the error either. A wire jumper could connect the RD and DB wires at the BFLS, but the marginal resistance of the wire jumper may lead to a short circuit. Under the assumption that the BFLS is indeed the problem, either the switch ought to be replaced or the brake lines need to be bled and refilled.

Prompted by the realization that the EMC wire jumper connecting pin 13 to BATT- had not been connected, the parking brake circuit was reexamined. Since the CH was delivered without a pin (jack) for position 13 of the EMC, a suitable jack had to be located. A suitable jack in this instance refers to one that is not specified for that connector but fits within the connector while

contacting the plug. A ring connector was crimped onto the opposite end of the wire jumper, so it could connect to the PSDM BATT- post. Connecting pin 13 to BATT- had no visible impact on the GEM; i.e., the parking brake warning remained. After reading testimonies of other individuals repairing their GEMs and seeing the parking brake diagram from the 2010 GEM service manual, it was clear that the parking brake wiring ought to be changed. The 2010 service manual shows EMC pin 13 connecting to position 87 of the controller relay, which is one of the two automotive relays. The second relay is labeled the PSDM relay. This diagram shows power to the parking brake switch coming from PSDM S6—seen in Figure 5 just to the right of J1 and J2. By closing the parking brake switch, both the PSDM relay and controller relays are activated. Both the PSDM relay and controller relay are NO. Thus, when the PSDM relay closes, 72 VDC from PSDM J6H is applied through PSDM J6G to HV GND. Subsequently, sounding the parking brake buzzer. Closing the controller relay connects EMC pin 13 to HV GND.

According to the 2010 parking brake diagram, the parking brake only switches 12 VDC [33]. This is quite different than the 72 VDC used in the 2007 parking brake circuit [22]. The voltage supply originates at the PSDM spade, S6. While the MDS is closed but the key switch is off, disengaging the parking brake allows the RD/WT 12 VDC voltage supply to pass through the parking brake switch COM spade to the NO spade. The TN wire on the parking brake switch NO spade follows the RH from under the bench seat to the passenger side of the dash, where it then splits to connect to positions 85 of both the PSDM and controller relays. Position 86 connects to 12 VDC, or chassis, GND. When there is 12 VDC across positions 85 and 86 of the relays, they close to produce the situation described in the previous paragraph.

Here, new wiring changes were tested, demonstrating that the parking brake buzzer still functions and pin 13 connects to GND. Unfortunately, this did not turn off the emergency brake light, either. With the parking brake fully-functioning, there are three remaining options to pursue. There might not be contact between plug 13 and jack 13 at the EMC; however, this is doubtful. Jack 13 is not as long as the other jacks, but it visibly appeared to be sufficient. Again, before choosing the jack, different jacks were compared to determine which fit the jack the best. Besides this, the issue may still concern the BFLS. Specifically, the BFLS was never replaced and there is no simple way to determine if it is functioning correctly. Otherwise, the brake warning may be resolved by bleeding the brake lines of any air. Considering the brake fluid master cylinder was opened to add brake fluid, air could have entered the system.

As a result, despite all attempts to resolve electrical and mechanical issues facing the GEM, the vehicle is not yet capable of being driven. However, all accessory systems are functional. While it is preferred to test BMS vehicle controls with a fully functioning vehicle, the next section illustrates the configuration of the BMS to ensure safe battery pack operation, subsequently addressing a prior issue.

2.6.4 BMS Vehicle Control

Ideally, integrating the BMS within the GEM would include communication between the BMS and the EMC; thus, allowing for finer controls. While the SX Transistorized EMC is not CAN enabled, it does have RS232 communication capabilities. However, configuring communication from CAN to RS232 is not typical, nor does this method guarantee success. Moreover, the RS232 communication lines on the EMC (pins 20 and 23 from Table 4) are already in use. In specific, negative (-) signals are sent from EMC pin 20 to PSDM J5G and then sent from PSDM

J3F to display D1K. Furthermore, positive (+) signals are sent from EMC pin 23 to PSDM J5E, and then sent from PSDM J3E to display D1J.

Alternatively, the same method used previously can be applied to the vehicle; however, now it would no longer interpose the start switch circuit. In particular, before the vehicle receives battery power, the BMS must decide if the batteries are safe to be discharged. Moreover, if the vehicle begins discharging too quickly, the BMS will again prevent current from flowing to the vehicle. Therefore, certain aspects of the original GEM will no longer play any part in the charging process, as regenerative braking is disabled, and charge interlock is decided by the BMS. Overall, the master disconnect switch (MDS) still determines whether the vehicle is in use or not. When the MDS is on, the switch is closed, and current can flow to the BMS and vehicle. Here, turning the MDS off opens the circuit, preventing further discharge. However, the batteries can still be charged while the MDS is off because both the BMS and ElCon charger are on a separate circuit that receives power from a properly-rated receptacle.

Once the MDS is closed, 72 VDC nominal is available to power the BMS. However, the BMS voltage input should be reduced to approximately 12 VDC. Here, a RECOM DC/DC converter (model RP20-11012SFR/P portrayed in Figure 31) converts the battery voltage to 12 VDC, which then provides power to the BMS through pin 2 (Ready Power) of the BMS Main I/O connector [34]. Positive input voltage to RECOM DC/DC pin 1 comes from the MDS once open and negative input; whereas, pin 2 is connected to PSDM post BATT-. Since the RECOM converter does not have an internal fuse, a 2 A fuse is in series with the positive input (pin 1). Overall, all 12 VDC electronics share the same ground; hence, RECOM DC/DC pin 5 is connected to chassis GND.

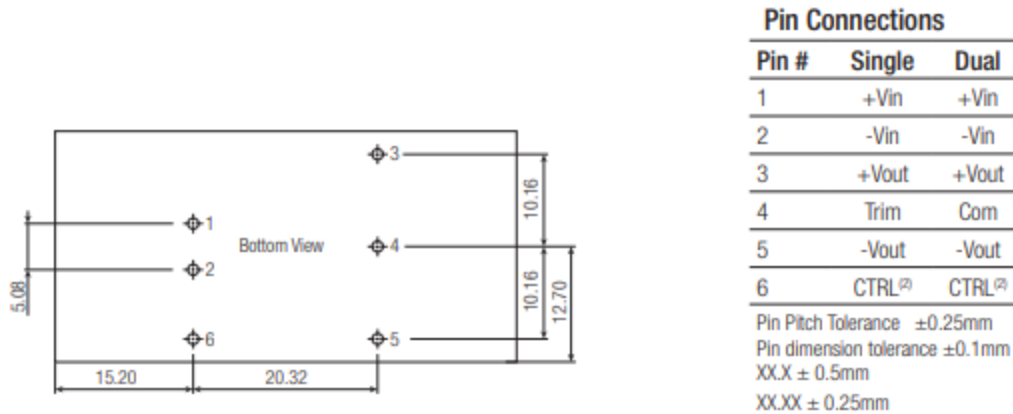


Figure 31: Layout and labels of pins on the bottom of the RECOM DC/DC converter [34]

In addition, the RECOM converter powers the relay that the BMS uses to regulate discharge.

Here, the BMS Discharge Enable (pin seven of the Main I/O connector shown in Figure 10) is connected to slot 4 of the Crydom D1D100 solid state relay (SSR) shown in Figure 32 [35]. The coil is powered through slot 3 of the Crydom SSR at 12 VDC, which is provided by the RECOM converter. While discharge is disabled, the voltage at the Discharge Enable pin is nearly the same as the 12 VDC input. To enable discharge, the voltage of the Discharge Enable pin is dropped to ground potential, subsequently resulting in current flow that then closes the relay.

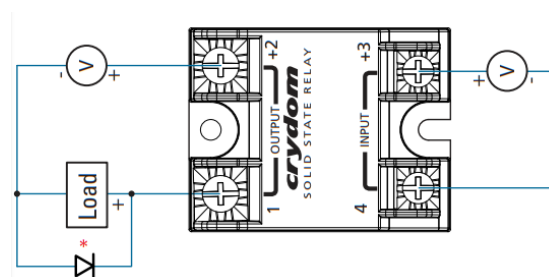


Figure 32: Crydom SSR suggested wiring diagram including diode suppression of the load [35].

In general, BMS digital outputs turn on by dropping to a lower voltage, where they draw (sink) up to 175 mA that can be dispersed as heat. However, the Orion BMS can only sink up to 100

mA. Consequently, the relays controlled by the BMS must work at nominal 12 VDC and pull less than 175 mA. The Crydom SSR has a maximum input current of 15 mA and works between 3.5 and 32 VDC. Typically, the BMS uses 250 mA, and combined with the current required by the SSR, the current is lower than the full load output of the RECOM converter (1670 mA). By means of the Crydom SSR, a low voltage and current passed through the coil is used to control vehicle access to high voltage and high current through the switch.

High voltage input from the MDS connects to terminal 2 of the Crydom SSR. When the relay is closed, current exits the Crydom SSR through terminal 1 that in turn is connected to the HV positive post of the PSDM. Here, the output connected to the Crydom SSR must be diode suppressed to prevent damage from inductive loads. Currently, a 1 A, 400 VDC rectifier diode from Comchip (part number 1N4004T-G) runs from the PSDM 72 GND post to the PSDM HV + post. There are replacement diodes available if the current diode fail, or a more robust Vishay Schottky diode (part number VS-100BGQ100HF4) may be used.

2.6.5 BMS Charger Control

BMS charger controls are similar to vehicle controls: i.e., power is supplied to the charger when the BMS has determined it is safe to charge. Therefore, when power is supplied through the charger cable, 120 VAC at 60 Hz is converted to 12 VDC that runs to Charge Power (pin 3) of the BMS I/O connector in Figure 10 using an Enercell Cat. No. 273-357 AC adapter.

Subsequently, Charge Power turns on the BMS. If both Charge Power and Ready Power are provided concomitantly, the BMS enters Charge Interlock; thus, preventing discharge while charging. In general, Charge Interlock stops the GEM from being driving while still connected to an external power source.

Once it is safe to charge the batteries, Charge Safety (pin 6) of the BMS I/O connector drops to a low voltage, in turn, sinking current drawn through the Omron DPDT relay (MJN2CE-D12, a 12 VDC non-latching 2 Form C relay consuming a nominal 1.2 W). The Omron relay terminal arrangement shown in Figure 33 differs from other DPDT Omron relays and is specific to the MJN2CE model.

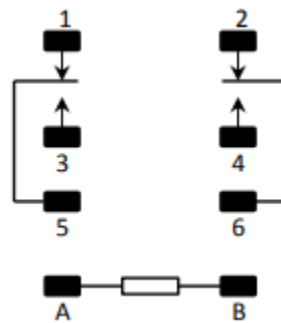


Figure 33: Terminal arrangement of the Omron DPDT relay.

A second AC/DC adapter (Bestec model EA0121WAA No. 2103-30001211R) converts the 120 VAC at 60 Hz to 12 VDC that connects to quick connect terminal A of the Omron relay. In comparison, Omron relay terminal B connects to Charge Safety. Since the ElCon charger receives power in the form of single-phase AC (i.e., power is typically comprised of two live or hot wires and ground), the two hot wires must be interrupted by the Omron relay; hence, the double throw. The BK hot wire enters through Omron relay terminal 5, while the WT hot wire connects to terminal 6. Moreover, Omron relay terminal 3 connects to the BK wire of the ElCon charger and WT wire from ElCon charger connects to terminal 4. The green ground wire proceeds uninterrupted by the relay. Both AC/DC adapter 12 VDC outputs are connected to the chassis ground. Finally, a 9 ft. 14 AWG Husky brand extension cord connects to the mains

power using a 3-prong plug, providing power to the three sockets used by the two AC/DC adapters and the ElCon charger.

2.7 Recommendations & Discussion

As the GEM currently stands, there are still errors to be addressed before the BMS and battery pack can be tested under road conditions. Determining the cause of the persistent emergency brake light and then rectifying the issue is necessary to begin troubleshooting any remaining issues. The advent of the emergency brake light made diagnosing the start switch impossible because the parking brake must be disengaged before the motor controller will enable the accelerator. If air in the brake fluid lines is not the cause of the emergency brake light, then it follows that the BFLS may need replaced. Moreover, it remains unknown whether the start switch will engage after repairing and upgrading the motor controller. Perhaps, the PSDM is broken, in which case replacement would likely be prohibitively expensive. In addition, there is the option to seek a certified technician to diagnose and repair the GEM, or the extant electronics within the GEM can be expunged and replaced with entirely new and discrete electronics. Assuming CAN remains the preferred form of communication within the upgraded GEM, it is feasible to retrofit the mechanical aspects of the vehicle (frame, chassis, suspension, brakes, etc.) with CAN enabled devices.

2.8 Conclusion

Efforts to repair the GEM to fully functioning status have been unsuccessful; however, significant progress has been made. All accessory systems are fully functional. Initially, driving was prohibited by a start switch error for which the retrofit BMS-controlled relays were removed, the accelerator was replaced, the SX Transistorized EMC was updated, and the CH

was replaced. Seemingly, none of these modifications restored start switch functionality. Moreover, further troubleshooting the start switch through diagnostic error codes on the LCD display have been impeded by the vehicle entering charge interlock mode, followed by brake issues. While the charge interlock issue was solved quickly, the brake issue persists. Since the emergency brake light is illuminated on the dash, the GEM believes that either the parking brake is engaged or that the brake fluid level is too low; thus, preventing the vehicle from driving. Despite upgrading the parking brake circuit and many attempts to identify the route of the BFLS issue, the cause remains unknown and has yet to have been fixed.

Notwithstanding the result of the GEM repair efforts, the GEM battery pack has been upgraded. The 40 Ah LFP batteries were replaced with 60 Ah LFMP batteries, and—with some trial and error—a new battery box was fabricated. There is evidence to believe that some of the original 40 Ah LFP batteries failed because of charging at below-freezing temperatures. Hence, greater attention has been given to making a BMS profile to prevent such harms befalling the 60 Ah pack and granting the BMS the ability to enforce limitations. Furthermore, BMS controls, hitherto intertwined with typical GEM functions, have been replaced. Now, BMS operations precede the original GEM. The new BMS scheme controls the power supplied to the GEM to avoid interrupting vehicle functions; whereby, causing issues much alike those of the first BMS scheme. While the BMS installed within the GEM cannot be fully tested, vehicle performance is predicated on the mode of employing battery management. In general, effectively employing a BMS involves understanding battery behavior, issues affecting these batteries, and the methodology of battery management.

3 Battery Management

3.1 Abstract

Battery management has become essentially necessary for use of lithium-ion batteries given their sensitivity to overcharge, over-discharge, and temperature particularly. Successful battery management requires knowledge of the interaction between battery composition, function, and external conditions. An introduction to batteries commences with composition and construction, and then proceeds with fundamental thermodynamics and electrochemistry pertaining to battery functions.

Nomenclature

Variable	Description	Units
C_B	Concentration in Bulk Electrolyte	$[mol/m^3]$
C_E	Concentration at Electrode Surface	$[mol/m^3]$
E_{anode}°	Standard Anode Potential	$[VDC]$
$E_{cathode}^\circ$	Standard Cathode Potential	$[VDC]$
E_{cell}°	Standard Cell Voltage	$[VDC]$
a_i	Activity of Species	$[-]$
η_c	Concentration Polarization	$[VDC]$
ΔG°	Standard Gibbs Energy	$[J/mol]$
F	Faraday's Constant	$[C/mol]$
R	Universal Gas Constant	$[J/mol \cdot K]$
T	Temperature	$[K]$
i	Current	$[A]$
n	Number of Electrons in Reaction	$[-]$
η	Overvoltage	$[VDC]$

3.2 Introduction

Batteries are used in numerous applications, many of which are employed in our quotidian lives. Nowadays, people tend to think of batteries as those used in mobile applications, such as electric vehicles (EVs), cell phones, and laptops. These secondary batteries are readily rechargeable; whereas, primary batteries are those intended for a single discharge cycle. Generally, primary batteries are preferred for more extreme climates where the battery cannot be charged, or when performance requirements are more rigorous. Such cases include pacemakers and electrical power for military installations. Contrastingly, primary batteries are still used in many common portable devices, like toys, radios, and flashlights. Application and performance of both primary and secondary batteries depend on chemical composition and construction.

The chemical constituency and output of batteries covers a broad spectrum, increasingly so as battery technology continues to improve. Specifically, as energy storage devices, care needs to be taken so that the stored energy is released appropriately. Performance relies on not only manufacture and design, but also the conditions of use. Maximizing the longevity and utility of a battery involves adhering to design limitations and maintenance. Furthermore, considering that batteries can be somewhat volatile and expensive, it is important to understand their capabilities and limitations (e.g., temperature range) so that they can be used safely and effectively. In general, the highest priority should be safety. Before working with batteries, there must be a basis of understanding with electrochemistry being core to battery function and limitations. Additionally, cell design and components are introduced here to establish fundamental concepts.

3.3 Getting to Know Batteries

3.3.1 Parts of a Battery

A cell is the fundamental unit of a battery and in practical usage is comprised internally of a positive electrode, negative electrode, electrolyte, and separator. Generally, cells include a casing, current collectors, and terminals. As mentioned in section 2.5.1, commercial secondary cells are formed into prismatic, cylindrical, and pouch formats. At the simplest, an electrochemical storage device requires two electrodes—an anode (positive electrode) and a cathode (negative electrode)—and electrolyte. The terminology anode and cathode refer to reaction sites and will be discussed in the following section. Separators are placed between electrodes to prevent contact and current collectors connect to the electrodes, allowing electrons to freely travel between the electrodes and the battery terminals. Current collectors from each positive electrode interconnect, ending at the positive terminal. Conversely, current collectors

from each negative electrode are all interconnected with the negative terminal. The separator and both electrodes are all enveloped in the electrolyte.

An arrangement of cells in series, parallel, or a combination thereof, as well as any protective components thereon, make up a battery. Internally, prismatic cells are comprised of alternating anode sheets and cathode sheets, with a separator sheet inserted between each electrode. Since the stack of electrodes and separators cannot operate independently, it represents just one cell. Thus, individual 3.2 VDC, 40 Ah or 60 Ah units are cells, while simultaneously considered a battery in vernacular. The 60 Ah GBS cells currently in the GEM have plastic cases and aluminum terminals. Unfortunately, the specifics of commercial cells often remain confidential, so generalizations must be made. Discussion henceforth is limited to lithium-ion batteries.

Positive electrode current collectors are predominately aluminum, while the negative electrode current collectors are mostly copper. These materials are chosen because they are electrical conductors that are relatively stable at the electric potential for which they are used. Sometimes the current collector will form a passivation layer which greatly reduces the rate of corrosion, but coatings can be applied to further resist corrosion. Likewise, alternative current collector materials have been suggested [36]. In commercial uses, separators are often polyolefins, such as microporous polyethylene or polypropylene films [15].

3.3.1.1 Negative Electrode

Before the development of the secondary lithium-ion battery, lithium metal was used as the negative electrode but was not successful due to safety concerns [37]. Negative electrodes of lithium-ion cells, and more specifically LFP and LFMP, are typically composed of carbon: petroleum coke or various forms of graphite, like natural graphite or mesocarbon microbead

(MCMB). An ordered graphite electrode allows for the intercalation of lithium ions and increases the electrode volume by roughly 10% [17]. Improvements to carbon electrodes has led to research of various binding materials, production processes, and molecular structure and porosity. Meanwhile, lithium titanium oxide or lithium titanate (LTO) have been introduced as a safer negative electrode for high power and high cycle applications [18, 38]. Additionally, research into conversion materials forming lithium alloys might be an option when there is little concern about volume changes greater than 200% [17].

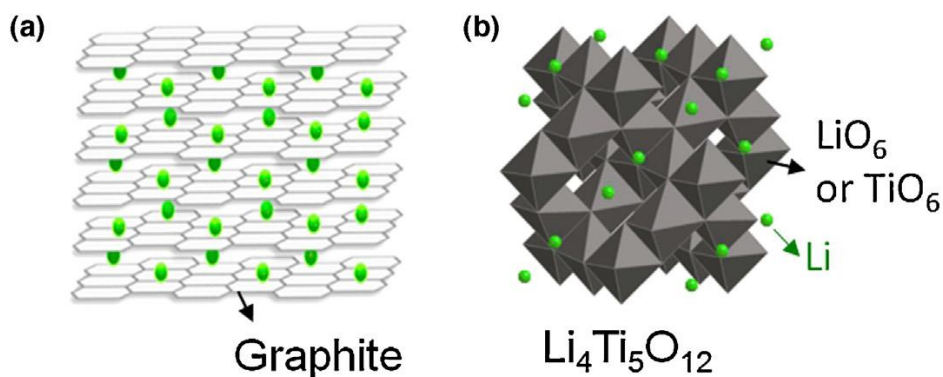


Figure 34: Molecular structure of two contrasting negative electrode materials in lithium-ion batteries [17].

Cells using graphite negative electrodes, like shown in Figure 34, have higher voltages than cells using LTO, illustrated in the same figure. Graphite electrodes are often coated with amorphous carbon to prevent intercalation of the electrolyte propylene carbonate (PC), and reduce surface area [15]. Disordered carbon electrodes with small grain sizes undergo less strain, and reduced PC intercalation. Reducing the surface area of the carbon electrode increases safety, but it also reduces the rate capabilities of the electrode. Here, LTO is less reactive with electrolytes and experiences far less strain from lithiation; thus, it has a longer cycle life.

3.3.1.2 *Positive Electrode*

As suggested by the naming convention of cells, positive electrode materials have become more variable and distinguishable than negative electrode materials. Positive electrode materials in lithium-ion batteries allow for the intercalation of lithium ions, preferably without structural changes or solubility within the electrolyte [15]. Moreover, positive electrode materials are sought to be inexpensive, be relatively easy to prepare, be thermally stable, have high energy density, and have a large electrical potential in respect to lithium. Many lithium-ion battery cathodes constitute transition metal oxides with varying metals and relative quantities researched to improve performance [17]. One avenue of cathode materials explored are polyanion compounds, which led to the production of LFP. Phosphate, sulfate, and silicate—to name a few—are polyanions used in lithium-ion batteries to increase the redox potential and stabilize the chemical structure. In general, LFP and lithium manganese phosphate (LMP) often have olivine structures, like that shown in Figure 35. While LFP cathodes have high power capabilities and thermal stability, they have low potential and often need carbon coating to improve their low electrical and ionic conductivity. Both electrodes include binding materials (i.e., polyvinylidene fluoride (PVDF)) and diluents (i.e., carbon black) to adhere the electrode to the current collector. For the GEM vehicle, details of Zhejiang GBS Energy Co., Ltd. lithium iron manganese phosphate (LFMP) cells are limited; therefore, perception of the LFMP cells is limited to generalizations evinced by the active positive electrode material.

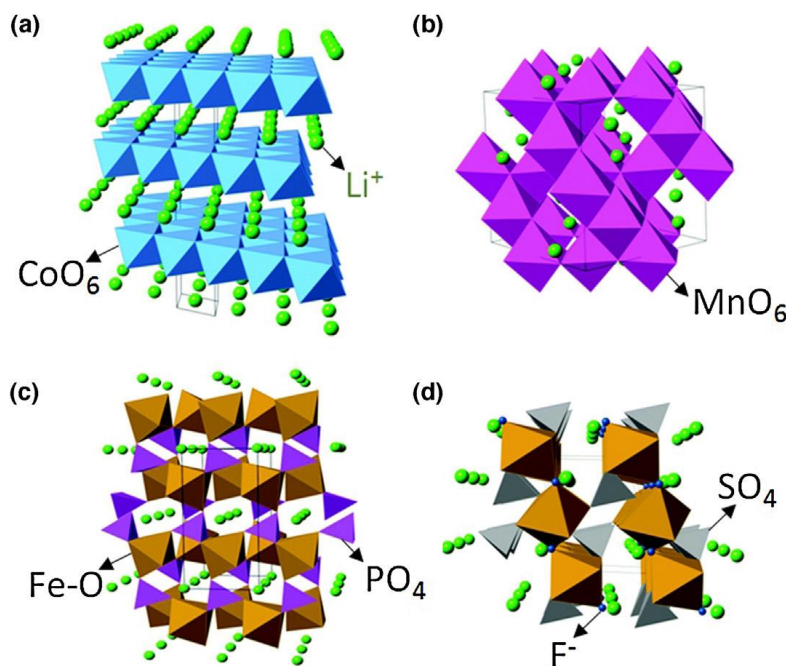


Figure 35: Crystal structures of different lithium-ion positive electrodes. LiCoO_2 (LCO) is the layered structure in (a). The spinel structure in (b) is that of LiMn_2O_4 . LFP in (c) is an example of an olivine crystal structure. Lastly, (d) is a favorite structure belonging to LiFeSO_4F (LFSF) [17].

3.3.1.3 Electrolytes

Liquid electrolytes in lithium-ion batteries—typically composed of organic solvents and lithium salt—also vary greatly to overcome electrochemical challenges. Some of the more notable salts include LiPF_6 , lithium bistrifluoromethanesulfonimide ($\text{LiN}(\text{CF}_3\text{SO}_2)_2$), and lithium bis-oxalato borate (LiBOB) [15, 37]. Organic solvents used in LFP cells are often carbonates, including ethylene carbonate (EC), dimethyl carbonate (DMC), and diethylcarbonate (DEC). Use of propylene carbonate (PC) is usually avoided unless used with other solvents as it can destroy graphitic negative electrodes. Though aqueous solvents have better conductance, hydrogen gas is formed during the creation of the passivating film at the anode and combining water with lithium salts containing fluorine (F) creates hydrofluoric acid. Organic solvents are still inflammable and

react exothermically with oxygen. However, LFP/LFMP cells decompose at higher temperatures than lithium metal oxide cells and are less likely to release oxygen. Electrode surface structure and chemical stability change when cycled with different electrolytes. Depending on the degree of lithiation of a carbonaceous anode, exothermic electrode decomposition may begin at elevated temperatures as low as 41 °C, and higher when in contact with EC and DEC [39]. Assorted solvents and salts are used to achieve desired properties: increasing thermal stability, conductance, rate capability, while decreasing capacity fade.

3.3.2 Simplified Battery Function

Battery function requires that the electrodes and current collectors are electrical conductors while the electrolyte and separator are both electrically insulating and ionically conducting. The active materials in the electrodes determine the theoretical voltage of a cell. Each material has an electrode potential that describes its tendency to acquire electrons or to give electrons compared to the standard hydrogen electrode (SHE). Materials that accept electrons through reduction are oxidizing agents and have positive voltage with respect to the SHE. Materials that give electrons through oxidation are reducing agents and have negative voltage with respect to the SHE.

Discharge proceeds once there is a path—an external circuit—connecting the positive electrode to the negative electrode. While discharging, the negative electrode is the site of oxidation, and is thus an anode. Following, the positive electrode is reduced; thus, it is the cathode while discharging. However, the roles are reversed while charging since the negative electrode is reduced and the positive electrode is oxidized. The electrolyte and separator are electrical insulators and ionic conductors, allowing the movement of lithium ions.

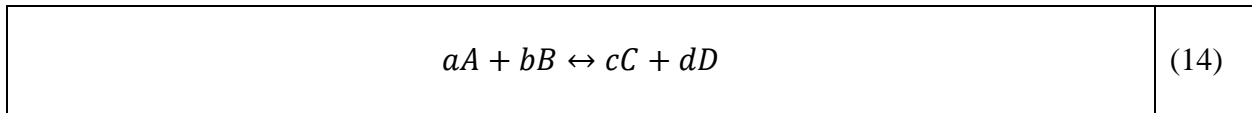
An electromotive force drives the reaction. For a cell comprised of an anode and a cathode, the voltage (E_{cell}°) is equal to the difference between the cathode potential ($E_{cathode}^{\circ}$) and the anode potential (E_{anode}°).

$E_{cell}^{\circ} = E_{cathode}^{\circ} - E_{anode}^{\circ}$	(12)
--	------

For a cell with a LiC_6 (graphite) anode and a LiFePO_4 (LFP) cathode at 25 °C, the standard reduction potential of the anode is approximately -2.8 VDC and 0.42 VDC for the cathode. Hence, the approximate standard reduction potential of the cell is 3.22 VDC. Subsequently, equilibrium conditions of the electrochemical system are determined by thermodynamics. The difference in electric potential, or voltage, between the positive and negative electrode draws current through the external circuit. In an ideal situation, the theoretical voltage across the electrodes equals the sum of the oxidation potential of the anode and the reduction potential of the cathode. Following reactions at both anode and cathode sites decrease the Gibbs energy (ΔG). Therefore, under standard conditions:

$\Delta G^{\circ} = -nFE^{\circ}$	(13)
-----------------------------------	------

where the standard electromotive force is denoted as (E°) with (F) as Faraday's constant and (n) is the number of electrons moved in the reaction. However, for non-standard conditions, the voltage can be calculated using the Nernst equation, which includes the activity of the species, (a_i), the temperature, (T), in Kelvin, and the gas constant, (R). Given a basic reaction:



The Nernst equation using species activity can be calculated:

$E = E^\circ - \frac{RT}{nF} \ln \frac{a_C^c a_D^d}{a_A^a a_B^b}$	(15)
---	------

As current flows through the battery, the cell potential changes from its equilibrium value. This change is known as polarization, and has three primary contributors: ohmic, concentration, and activation. In addition, the polarization of an electrode is known as overvoltage with the operating voltage reduced as the current draw is increased, as seen in Figure 36 [15, 24]. As an electrical system, the battery has an overall impedance resulting in the ohmic polarization. The resistance component (IR loss), shown in Figure 36, characterizing this impedance is due to the electronic resistances of the electrodes, current collectors, and contact resistances between electrode to current collector and current collector to terminal. Since resistance is added in series, this can be represented as a singular internal resistance value, R_{int} .

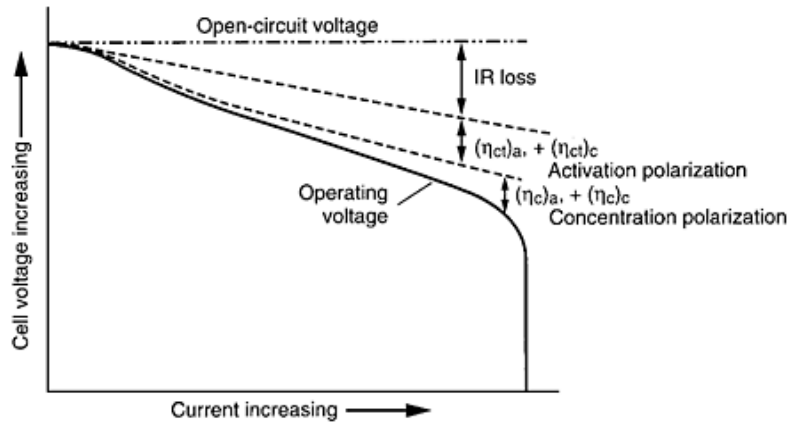


Figure 36: Reduction of operating voltage from open-circuit voltage due to ohmic, activation, and concentration polarizations [15].

Polarizations are comprised of losses in each mechanism of battery function. Typically, there are several steps in the overall process. This involves the movement of electroactive species to the electrode surface through migration or diffusion, and possible adsorption before and after

electron transfer. With many batteries, there are chemical reactions affecting the processes at the electrode. Experiments on many electrochemical systems have shown that for large overvoltage, the Tafel equation describes the relation between current and overvoltage. Accuracy is greatly diminished at low overvoltage; hence, it is assumed that this expression represents unidirectional processes. Therefore, overvoltage, (η), is exponentially related to current, (i), of which the general relation is described by the Tafel equation:

$\eta = a \pm b \log i$	(16)
-------------------------	------

with constants (a) and (b). When the overvoltage is large, current and overvoltage are nearly linearly related, simplifying the determination of a and b . Moreover, the slope of the log current versus overvoltage curve is b , while a is the projected intercept with the logarithmic current axis (horizontal).

Concentration gradients play a role in the movement of species towards the electrodes but the concentration at the electrode-electrolyte interface is also affected by the electric potential differences. Activation polarization is attributed to losses during charge transfer across this interface. The potential driving the charge transfer at each electrode is equal to the difference between the electrode potential and the potential of the species at its closest approach. Charge within the electrolyte is polarized to form a boundary impeding the ion from reaching the surface of the electrode. When polarized, there is a layer of charge at the electrode and another in the electrolyte, creating an electrical double layer. Extending out from this first double layer are repeated layers of charge, but at diminishing electrical potential.

In conditions where there is an excess of electrolyte, the electric potential gradient has little effect on mass transport. However, the electric field is increased by convex curvature of the electrode. In addition, mass transport grows through stirring and convection, but the impact is nullified when gelling agents are used to increase viscosity or the battery is a dry cell, meaning that there is no free liquid. Diffusion enabled by a concentration gradient is the primary mass transport mechanism in dry cells. In an ideal cell, losses from diffusion are not considered; wherefore the concentration gradient driving mass transport contributes to the overpotential. Specifically, concentration overpotential results from the concentration gradient in the diffusion layer between the bulk electrolyte and electrode surface. Using the Nernst equation, the concentration polarization, (η_c) , can be calculated:

$\eta_c = \frac{RT}{nF} \ln \left(\frac{C_B}{C_E} \right)$	(17)
---	--------

The variables remain much the same from equation (15); however, here the ratio of the concentration in the bulk electrolyte, (C_B) , and concentration at the electrode surface, (C_E) , are used rather than the activities of species.

Batteries do not operate under perfect conditions, nor do they function ideally. Even under the best operating conditions, secondary batteries can only be cycled (discharged and charged) a finite number of times. External factors may exacerbate battery issues, but typically when a battery is retired, it is because of internal damage or impending failure. The properties of materials making up the cell are variable, and after repeated use over time, active material can be lost and electrodes might be damaged.

3.3.3 Battery Issues

3.3.3.1 *Mass Transport and Diffusivity*

In practice, mass transport is complicated by diffusion through the porous electrodes. The surface area of the electrode is augmented by implementing porous electrodes, which in turn provides more sites of charge transfer. In general, temperature has a considerable impact on battery health and performance. Discharging at low temperatures reduces chemical activity and increases the internal resistance of the cell. Liquid electrolytes become more viscous and mass transport slows. While high temperature discharge increases chemical activity, there is a point where the self-discharge rate increases enough to cause a noticeable loss of capacity. High temperatures also increase the favorability of undesired side reactions. When temperature is too high, the passivating layer of the electrodes breaks down and reacts exothermically.

3.3.3.2 *Self-Discharge*

Self-discharge of a cell is the process of a cell losing capacity and dropping in voltage while the cell is not in use. Capacity lost to self-discharge is largely reversible and the rate of self-discharge in lithium-ion cells is respectively quite slow [40]. However, the mechanisms largely responsible for self-discharge are influenced by temperature, where elevated temperatures will significantly increase the rate of self-discharge. Moreover, certain electrolyte additives and positive electrode coatings reduce the favorability of solvent oxidation at carbon black regions of the positive electrode surface; thus, slowing the rate of self-discharge. Solvent oxidation at the positive electrode and solvent reduction at the negative electrode both form passivating films on the respective electrodes, in turn reducing the rate of continued passivation. Hence, after the film has formed, self-discharge is slowed. Once the film has formed, the voltage at which the cells

discharge will be lower than expected, relative to the impedance of the passivating film [15].

Batteries stored at higher temperatures and for longer durations are more likely to have reduced discharge voltage. However, most of the capacity lost while in storage can be returned. The time it takes for the voltage to return to its expected level is known as the voltage delay. Slow discharge and high temperatures contribute to shortening the voltage delay, or the period before the voltage returns to its expected level. Contrarily, the voltage delay increases with the rate of discharge and decrease in temperature.

3.3.3.3 Lithium Plating on Anode

Some negative electrodes may be susceptible to lithium plating and dendrite formation. This issue is especially common with lithium metal batteries, and while the anode materials used in lithium-ion batteries are different, the impact remains the same. This effect most often occurs in graphitic anodes while fast charging, at cold temperatures, and at approximately full charge or especially when overcharged. Fully lithiated graphite anodes have little electric potential difference from lithium metal—once the anode overpotential is below 0 VDC versus Li^+ , lithium metal begins accumulating on the surface [41, 42]. Here, while charging too quickly, the lithium ions cannot diffuse quickly enough, which can also be the case when cold temperatures slow the diffusion rate [43]. Regions of lower electric potential on the anode—typically near the separator boundary—are more susceptible to lithium plating. Lower potential carbon anodes, such as graphite, are more likely to undergo lithium plating than coke [40]. Besides external conditions, lithium plating becomes more likely when there is an excess of cathode material, instances where the positive electrode overlaps the negative electrode, and local irregularities in the negative electrode composition and structure that cause increased polarization [21, 40]. Lithium plating

reduces the amount of active material in the cell, but also occludes pores on the anode surface. Large accumulations of lithium metal form dendrites, which are liable to puncture the separator between the anode and cathode, engendering a short circuit and subsequently fomenting hazardous side reactions [18, 44]. It is possible to strip the lithium plates from the negative electrode in cases where the cell has not been overcharged by simply allowing the negative electrode to rest; thus, this allows the lithium ions time to diffuse into the electrode [42]. Increasing the temperature of the cell will decrease the time it takes for the negative electrode to relax. Additionally, reversible lithium plating can be stripped during constant voltage (CV) discharge [41]. Since lithium metal readily reacts with many types of electrolyte, irreversibly consuming lithium to produce a variety of compounds that then make up the solid-electrolyte interface (SEI), it is best practice to avoid conditions propitious to lithium plating and dendrite formation.

3.3.3.4 Formation of SEI on Anode

Most electrolytes are not stable at the voltage of the negative electrode anode, approximately 0 VDC; thus, the solvent of the electrolyte is reduced, creating a passivating layer. Formation of the SEI effectively reduces the available charge of the cell but also impedes further degradation of the electrolyte [21]. SEI formation during the first several cycles appear as a reduction of capacity. Many variables of the cell design and manufacturing influence the formation of the SEI, including the active material, electrolyte composition, porosity, defects, etc. The SEI has variable composition but generally allows movement of cation through; hence, the slow ongoing corrosion of the anode and breakdown of electrolyte. Continued SEI formation reduces the active surface area of the electrode. While the initial formation of the SEI reduces the rate of

passivation, irreversible loss of active material and increasing impedance resulting from the SEI are signs of battery ageing. Transition metals from the cathode are prone to dissolution, increasingly so with elevated temperature, and can be found within the anode SEI [45].

Certain circumstances involving the SEI may result in hazardous conditions. Formation of the SEI can produce gases, which may need to be vented to continue using the cell [40]. Breakdown of the SEI can occur at high temperatures, resulting in an exothermic breakdown of the electrolyte. Accelerating heat generation occurs as electrolyte is reduced at the anode and oxidized at the cathode. Reactions depend on battery composition and state of charge. Without sufficient heat dissipation, the battery may enter a thermal runaway stage where combustion is likely.

3.3.3.5 Mechanical Degradation of Electrodes

Repeated lithiation and delithiation of electrodes develops stress inside the electrode, between the binding material—often carbon black to increase conductance—and LFP in the positive electrode, or between crystal boundaries or layers in the negative electrode. Strain resulting from lithium insertion in either electrode, or between the electrode and current collector, may lead to cracking or even exfoliation and delamination. This is pronounced in electrodes comprised of larger grain sizes and where the structure is more ordered. Cracks can electrically isolate regions, resulting in increased impedance and decreased capacity. Intercalation of lithium into the negative electrode results in an approximately 10% increase in volume, which when paired with the brittle nature of the SEI formation, can fragment the SEI. Thus, the negative electrode is opened to new sites of electrolyte reduction, further decreasing the available lithium.

Iron dissolution from the positive electrode occurs due to elevated temperature and reactions with acidic species such as hydrofluoric acid (HF), which primarily result from contamination with water. Carbon coatings used on the positive electrode to prevent iron dissolution. When first introduced, the LFP cathode was proposed to undergo a phase change while cycling, which has been cited in lithium metal-oxide cells to produce stress at phase change boundaries. Instead, LFP undergoes a non-equilibrium solid-solution reaction while cycling. Thus, LFP has an increased cycle life. As lithium enters the positive electrode, it is believed that the FePO_4 structure elastically deforms to accept the lithium ion. While phase change causes localized stress, the degree of delithiation is responsible for the phase change [46]. During the manufacturing process, delamination can be counteracted by using a gel-polymer electrolyte. Delamination of electrodes can be counteracted by applying pressure perpendicular to the laminated surfaces.

3.3.3.6 Over-Discharge

Using cells of different performance capabilities will reduce the available capacity of a battery pack. A battery pack connected in series is limited to the capabilities of the weakest cell. When discharging, it is the lowest cell voltage that prevents further discharge. And while charging, the cell with the highest voltage determines when charging is halted. There are several methods used to help batteries work more synchronously so they can last longer. When purchasing multiple cells at once, it is generally better to choose cells fabricated in the same line or closely within time so that the cells have similar capacities and internal resistances. Once fabricated, cell performance further diverges with disparities in use and storage; variations in cycling, depth of usage, and temperature are ageing factors to watch. Whether discharging or charging, it is

important that every cell is passing the same current, at the same temperature, and have the same resistance. Cells discharging more quickly will stop battery pack discharge early, unless an error indicates that the cell is over-discharged. Repeated overcharge and over-discharge of one or a few cells in the pack will accelerate their degradation. Even if the overall voltage of the pack appears normal, it is necessary to check individual cells. Over-discharge of even 10% in LFP cells will cause the oxidation of copper current collectors [47]. The voltage of the negative electrode increases greatly, 3.92 VDC versus Li^+ , as copper oxidizes to Cu^+ and increases again to 4.17 VDC versus Li^+ as copper oxidizes to Cu^{2+} . Copper cations that diffuse through the electrolyte and separator are reduced at the positive electrode to form copper dendrites. Based on the depth of over-discharge and the number of cycles the cell has reversed voltage, copper dendrites can puncture the separator and cause short circuits. Reduction of Cu^+ to Cu diminishes the voltage of the positive electrode to 3.19 VDC versus Li^+ . Since the negative electrode is at a higher voltage than the positive electrode, the overall cell voltage is negative. This is a case of cell reversal, or reverse voltage. Ideally, a cell will be replaced before voltage reversal occurs, but in instances that it occurs, protections ought to be in place to protect other batteries and the BMS from damage. Many electronics are susceptible to damage if the voltage polarity is opposite of expected.

3.3.4 Basics of Battery Care

Safe operation of lithium-ion batteries requires avoiding temperature extremes, over-discharge, and overcharge. Ideally, voltage, current, and temperature should be kept consistent across all cells. Cells ought to be stored at room temperature and roughly 50% SOC, away from direct heat sources and moisture. Avoid dropping, throwing, puncturing, crushing, setting aflame, or

otherwise physically harming the cell. External short circuits produce heat within the battery, may damage terminals, and if sustained, may irreparable damage the cell. Conductive tools and loose terminal connections are common reasons for external short circuits. Mechanical vibration within a vehicle in tandem with insufficiently secured cables may lead to complete disconnection, or repeated sparking between loose connections. Cycle life and longevity of cells is improved by moderating charge and discharge rates.

3.3.4.1 Passive Battery Protection

In the simplest of cases, battery management may only entail using passive means of protection. Passive electronics, which are even recommended for use in addition to complex BMS systems, can prevent excessive current rates and voltage reversal. Fuses and electrical breakers are employed to protect batteries against excessive current rates, whether discharge or charge. Fuses are designed to be used just once; thus, they must be selected so that they trigger only when necessary. Breakers, however, will trigger at different speeds based on the rate of current: higher current closes the breaker faster. Overcurrent protection is often inserted between the vehicle and the battery pack to prevent cell damage or placed between sections of the battery pack to limit the extent of damage to the pack. Positive temperature coefficient (PTC) devices increase resistance greatly with a rise in temperature; thus, they can be used to reduce current when in series with cells. Similarly, thermal fuses and temperature cutoff (TCO) devices can be set to trip at a designated temperature to prevent further current flow. Both PTC and TCO devices are resettable but TCO devices are usually for internal battery pack temperature while PTC responds to ambient temperature.

In general, thermal runaway represents a greater harm to people than other modes of battery failure. Damage due to voltage reversal can be reduced by adding a diode in parallel to each cell [15]. Bypass diodes conduct in the same current direction as battery discharge so that if a cell in series with another cell fails, most of the current will flow through the diode. Blocking diodes are in series with the cells to prevent current from flowing in reverse. Typically, blocking diodes are used to prevent primary cells from charging but can also suppress transient voltages from load switching or motors.

Safe usage of a battery in EVs requires more than electronic precautions. The battery pack needs to be electrically isolated from the chassis. Additionally, the cells should be protected from the ingress of dust and water while also allowing for heat dissipation and even temperature distribution, which primarily relies on convection. There should be a way to dispel gas purged from cells, though gas formation is hopefully avoided through applying pressure to prevent expansion and delamination. The battery pack should be secured, stable, and away from moving objects. Connectors to the battery pack should also be secured and routed such that the cables do not rub against abrasive or sharp objects that could damage the cable's insulation. Wires and electrical connectors should be properly sized and fastened firmly. There should not be tension on wires, or across wire connections. Bolted connections should be tightened according to their torque rating. Electrical contacts should be kept clean of oxidation, which may include applying an anti-oxidant compound if there is contact between aluminum and copper or connectors have not been coated against oxidation. This is especially important for the battery terminals and other high current connections. Increased resistance, including reduced contact area, will result in increased heating of the connection which then further oxidizes the connectors and terminals.

Flat washers should be used to increase the contact area of bolted connections. Additionally, split washers are used to apply a greater contact force on the connectors.

3.3.4.2 Series and Parallel Cell Configurations

Primarily, the decision to connect a battery in parallel or series depends on voltage and current requirements. Cells in series connect the positive terminal of the preceding cell to the negative terminal of the next in line. Voltage measured between the positive terminal of the last in line and the negative terminal of the first in line is the sum of all individual cell voltages. Each cell within the series all (dis)charge at the same rate—discharging the series of cells at one amp requires that each cell is also discharges one amp. Cells are placed in series to meet the voltage requirement of a system. Since the GEM functions between roughly 84 and 60 VDC, 24 LFP cells are placed within series for a nominal voltage of 72 VDC. At full charge, the series of LFP cells can get up to 86.4 VDC; however, this can be limited to the upper threshold of the system. The minimum (acceptable) voltage of the LFP battery pack is 67.2 VDC, which is above the lowest limit of the system. While the capacity removed from each battery is the same, each battery still has different internal resistance, may be at a different SOC, and thus may be at a different voltage. Cells in series are not forced to be at the same voltage or SOC; hence, cells at lower states of charge will finish discharging before cells at higher SOC. Similarly, cells at higher SOC will reach full charge before cells at lower SOC. The dangers of overcharging and over-discharging cells have been covered. It is prudent to avoid overcharging and over-discharging cells from the beginning because those cells will become more susceptible to further divergence from the rest of the cells. Knowing that the cell voltages can vary, cell voltages

should be tracked individually as well as across the pack. The cumulative voltage across the cells in series does not adequately inform if any cells are at risk of overcharge or over-discharge.

Within a circuit, the voltage across cells connected in parallel are always the same but resistance and current through each line can vary. The current output of a parallel arrangement of cells is the sum of current output by each cell. In most applications, but especially EVs, the operating voltage of the system exceeds the voltage of the cell. Once enough cells are placed in series to attain that voltage, then oftentimes a string of cells in series will be placed in parallel with another string of cells in series. Thus, the voltage meets the desired level, and the current output of the parallel strings is the sum of the output of each series. The cells in the GEM currently have a capacity of 60 Ah. If the number of cells was doubled, ideally the capacity of the 48 cell battery pack would be 120 Ah when comprising of two parallel strings of 24 cells in series. Discharge in each parallel string is limited to its weakest cell, as seen in Figure 37. Voltage of each string parallel string is the same, but individual batteries in a series may vary in voltage. If a cell is weaker than other cells in series and, therefore, has a higher internal resistance and lower voltage, the other cells in series will need to compensate for the lower voltage.

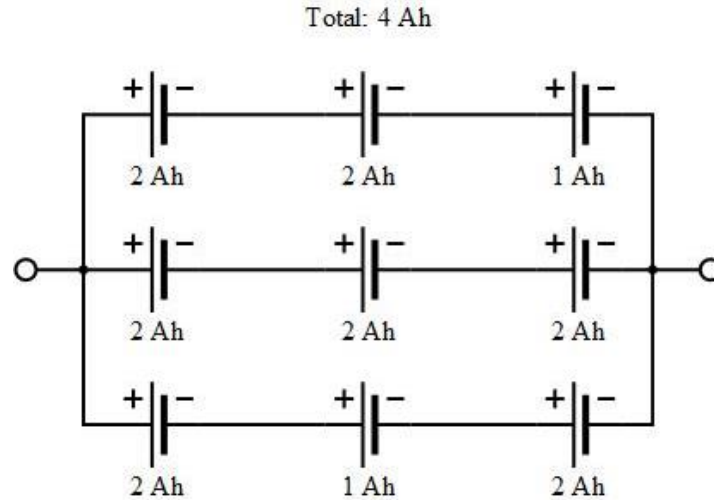


Figure 37: An example of a battery comprised of three parallel strings of three cells in series. The top and bottom series are limited to 1 Ah while the middle discharges 2 Ah for a total of 4 Ah from the battery.

Conversely, an array of cells in parallel can go in series with another array of cells in parallel that would ideally meet the same output as the two parallel strings of cells in series. An example of this configuration, shown in Figure 38, demonstrates that a weak cell in this configuration still reduces pack capacity but to a lesser degree. Cell voltage of a weak cell is supported by other cells in parallel, which can continue to discharge regardless of the weak cell.

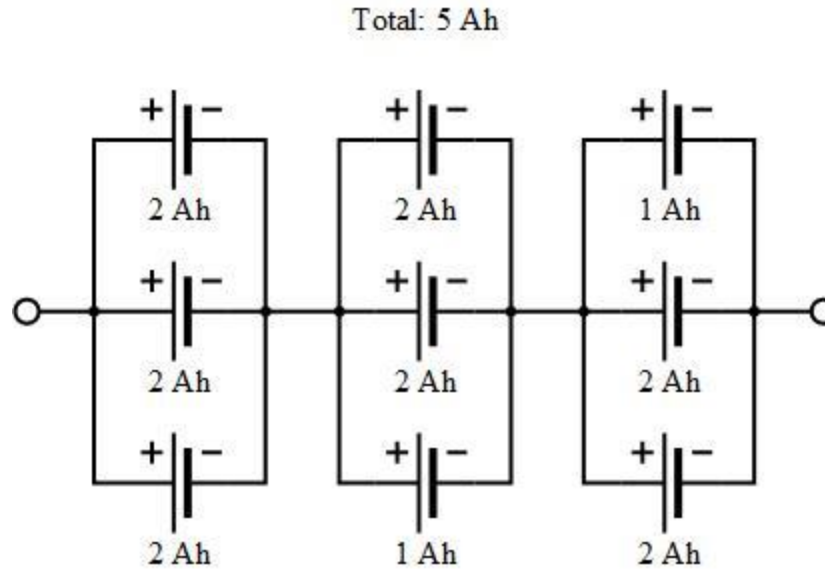


Figure 38: A battery configured as a series of three sets of three cells in parallel. Two of the parallel sets can only discharge 5 Ah; thus, the pack can only discharge 5 Ah.

3.3.4.3 BMS Configurations

Insofar as installation and space requirements are concerned, there are two categories of BMS: non-distributed and distributed. As mentioned in 2.5.6, a non-distributed BMS is installed in the GEM. Both distributed and non-distributed systems could have been used within the GEM, but the distributed BMS used by colleagues had proven onerous and delicate. Each cell in a distributed BMS has a cell board that monitors voltage and current. An example of cell boards is shown in Figure 39, but the image omits the central BMS controller.

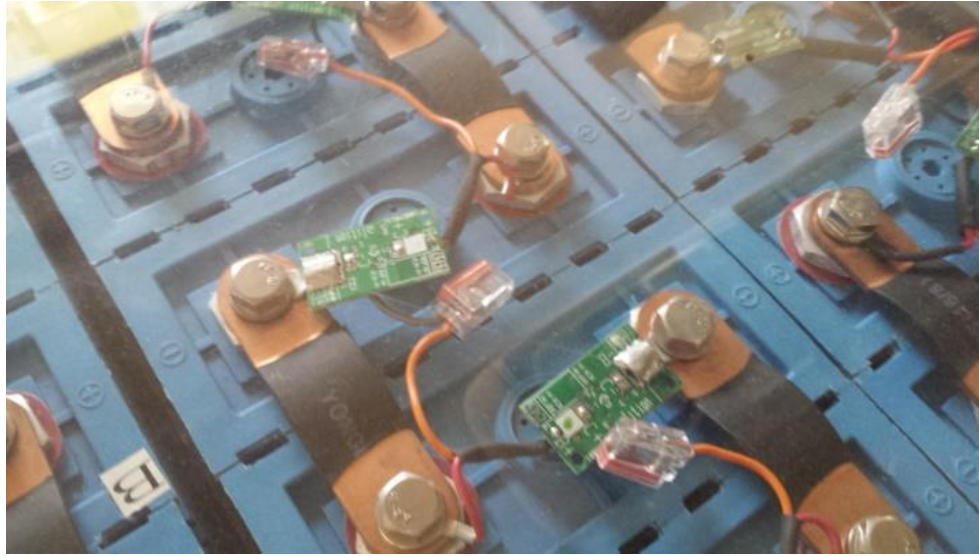


Figure 39: Photo of Elithion cell boards installed in a vehicle electrical conversion project [7].

Either a different distributed system could have been used or a non-distributed system could be instituted. However, a non-distributed BMS was favorable because it would not require as much space within the battery pack—a feature sought after because room for the battery pack is limited. Additionally, a distributed BMS still requires a large controller. Non-distributed BMS are not without weaknesses; here, 26 wires are connected to terminals throughout the GEM battery pack that need to be organized and constrained.

3.3.4.4 BMS Functions

Besides categorizing BMS by configuration, the degree of integration and complexity of the BMS can vary greatly. In general, the BMS exists to monitor batteries, protect batteries, maximize battery performance, and relay information to other devices and/or operators. Some BMS devices might only do one of these tasks while others have more features. Tasks may be approached differently with degrees of success.

Monitoring a battery includes direct measurement and approximating states, recording or displaying these data. The directly measurable aspects of a battery are calendar age, cycle number, voltage, current, and temperature. Cell-to-cell variations in voltage are the reason individual cell voltages are tantamount to the cumulative battery pack voltage. Furthermore, both discharge and charge current ought to be measured. Precise current measurement is important because it improves the accuracy of the SOC estimation. In addition, it is important to account for temperature. Extremes in ambient temperature can have a noticeable and severe impact on the batteries, but temperature gradients in and between cells will also degrade the battery pack. Here, battery states are not directly measurable, but can be approximated in several different ways using current and past data. In EV applications, the SOC is the pertinent information to the driver, and is a priority. Depth of discharge (DOD) is an alternative indication of SOC, instead describing the ratio of charge depletion to the max capacity as opposed to the percentage of remaining capacity. SOC ranges from 0-100% which limits the capacity based on voltage while DOD, in this definition, considers that there may be charge remaining that is temporarily inaccessible because of diffusion limitations.

There are battery protection strategies that do not require monitoring the battery pack, but these methods are usually less successful than informed systems. Arguably the simplest among BMS are chargers with charging profiles, such as constant current constant voltage (CCCV), that are designed to avoid overcharging the cells [25]. This option is not adequate for use with lithium-ion batteries because it is lacking critical functionality: the ability to prevent over-discharge, maintain cell balance, or inhibit individual cells from overcharging. The next step in capabilities is the addition of a regulator which bypasses current from cells once they have reached a certain

voltage [25]. Regulators help prevent overcharging and can balance cells to a moderate degree since all the cells will stop charging at the same voltage. Though the cells may be at the same voltage, this method does not consider that cells may vary by internal resistance and thus may settle to different voltages. There is an obvious need for the BMS to have control over discharge and charge limits, but before a BMS can implement controls, it must be capable of taking measurements and storing this information. Generally, with the ability of a BMS to gather and store information comes the capability of displaying or otherwise communicating information.

Active controls allow the BMS to start and stop (dis)charge, or even reduce the rate (derate) (dis)charge to prevent excessive harm. Overcharge can be prevented by either preventing current flow to the battery or by turning off the charger, subsequently ending the charge. Once a cell reaches the minimum cell voltage limit, discharge is ended. These limits apply to each individual cell, not to the pack to avoid damage when the pack is not balanced. Imparity of internal resistances between cells may result in a cell with greater resistance having higher voltage while charging and lower voltage while discharging. Because the SOC is defined by voltage, a BMS will cutoff (dis)charge even when just one cell hits the threshold. However, if the current rate is reduced, the cells would appear to equalize. The DOD remains the same; however, the SOC changes to reflect that (dis)charge can continue. Balancing is important to safe management of lithium-ion batteries and should be incorporated into charging and maintenance. Cells have maximum and minimum operating temperatures, though these temperatures change depending on whether the battery is being charged or discharged. For LFP cells, the window temperatures at which the cells can discharge extends both below and above the safe charging temperatures. If the BMS is capable, it is preferable to reduce the allowable current rate as temperature

approaches these thresholds. The allowable rate of (dis)charge also depends on the duration spent at that rate. In some applications, the battery might be subject to short durations of high current before resting or returning to reduced current. Limiting the duration of high current to pulses intend to reduce the damage incurred by the high current by giving a short rest period to allow diffusion.

Either analog or digital signals can be used to control (dis)charge. These methods allow for smoother operation of the vehicle than simply opening and closing a switch to stop and start current flow. On/off controls are typically the last resort when controlling a vehicle. Analog communication works through a linear relationship between a signal voltage and allowable current. The BMS may either source or sink a signal voltage proportional to the allowable current rate. Highest precision operation is over digital communication systems that offers the benefits of smooth transitions and faster communication. However, this digital communication is more susceptible to error or malfunction. The BMS should always have a way to stop current in and out of the battery pack for emergency and as a backup in case of malfunction.

3.3.4.5 Balancing Cells before Battery Pack Assembly

Battery voltages can be matched without the intervention of a BMS by connecting the cells in parallel. The difference in voltage between the cells will drive current from the higher voltage cells to the lower voltage cells until they are about equal. This method is especially beneficial if the cells are significantly unbalanced simply because balancing cells can be a time-consuming process. Charging the cells while in parallel can be used to prevent cells from falling below a certain level and additionally encourages more current flow where otherwise stymied by resistances. Once the charging current is removed, the cells voltages will settle. Typically,

balancing cells in parallel is done before assembling a battery pack because it can be an arduous process transitioning from the intended battery pack layout to having all the cells in series, then returning to the intended layout.

3.3.4.6 Battery Balancing Strategies

Besides taking steps to maintain the batteries equally, passive and active balancing can be used to minimize voltage differences amongst cells in a pack. Both methods start the same: remove charge from the higher voltage cells. Passive balancing discharges the cell through a resistor and the energy is dissipated as heat. Active balancing moves charge from the higher voltage cells to the lower voltage cells. There are several methods of active charge balancing varying by electromechanical topology and are preferably used in higher power applications to reduce the power lost. Balancing can be done at different times within the charge/discharge cycle. There are benefits to each, but top balancing is likely more beneficial for the GEM batteries. Bottom, middle, and top balancing refer to the states of charge at which balancing occurs with bottom being 0% SOC and top being 100% SOC. With bottom balancing, the batteries are discharged until a lower threshold to avoid over-discharging the cells. While every cell has a slightly different capacity, bottom balancing defines 0% SOC at a certain voltage near depletion. Bottom balancing prevents over-discharge, but the voltage at 100% SOC is more variable. Middle balancing defines a voltage representing 50% SOC. Top balancing defines a voltage for 100% SOC. Top balancing is pertinent to electric vehicles because they are usually charged to max capacity when charged. Fully discharging a vehicle battery pack is generally avoided, and range anxiety increases the operator's tendency to maintain a high state of charge. Balancing cell voltage at the end of charging will extend the duration needed, however. Since it occurs at the

end, there is a chance that balancing could be interrupted or repeatedly delayed. Fortunately, with proper battery maintenance, the cells will likely only need minor balancing monthly.

The rate of passive balancing is determined by the ability of the system to dissipate heat. Passive shunt resistors are used by the Orion BMS to balance the cells in the GEM. Approximately 200 mA can be dissipated per cell; thus, requiring about three hours to correct a 1% SOC discrepancy between the highest and lowest cells in the 60 Ah pack. Translating SOC to the voltage of a cell is not straightforward, but voltage can be easily measured while SOC is not directly measurable. And considering a general charge/discharge curve of LFP batteries, a relatively large change in voltage while nearly fully charged or nearly depleted correlates to a relatively small change in SOC. Thus, balancing cells within a small variation in voltage at either end of the charge/discharge cycle will bring the batteries within an even smaller difference of SOC.

In the Orion BMS manual, the maximum difference in voltage between the highest and lowest cells should be 10 mVDC for LFP batteries, though a larger difference will decrease the time it takes the battery pack to balance [29]. Setting the maximum voltage difference lower than 10 mVDC is typically not recommended as this may lead to a prolonged balancing cycle where the BMS repeatedly discharges alternating cells. Since the voltage of a cell is elevated above its resting voltage while charging in direct correlation with its internal resistance, there is a point where this raise in voltage is larger than the increase in voltage associated with increasing the SOC. Cells with higher resistance, though they may appear at a higher voltage while charging, will have a lower voltage while discharging; wherefore, the higher resistance cells will repeatedly undergo charge and discharge and possibly increase the unbalance of the pack.

3.4 GEM BMS

The purpose of the BMS within the GEM is to monitor the health of the batteries and extend their lifespan. Several measurements are taken by the BMS to monitor battery health and inform operating decisions. The Orion BMS can send information to the operator and other electronics, and stores data it acquires. In this application, the BMS is employed to enforce limitations on the rates of charge and discharge and battery voltage, which is done by interrupting or prohibiting use of the charger and vehicle. While the interfaces between the BMS and other electronics were more stressed during the design of the vehicle, the GEM BMS acts independently to balance cells and mitigate failures. PTC and TCO devices are not integrated into the battery pack so the BMS must shut off discharge in the event of thermal runaway. Diagnostic trouble codes are generated and stored, alerting operators of any issues arising from erroneous wiring, short circuits, isolation breakdown, damaged cells, etc.

Wiring and connectors of the Orion BMS are introduced in section 2.5.6, which includes images of the connector pinouts. The BMS has three possible power supplies and two primary modes of operation. Since the vehicle will not always be running nor connected to an external power supply, pin 1 of the Main I/O connector, shown in Figure 10, will not be used. The BMS uses approximately 0.25 A at 12 VDC while operating. When power is delivered to the Ready Power pin (pin 2 of the Main I/O connector), the BMS enters the ready mode unless powered simultaneously through the Charge Power pin (pin 3 of the Main I/O connector). While powered through the Charge Power pin, regardless of supply to Ready Power, the BMS enters its charge mode. Charge interlock mode behaves like charge mode but has some settings specific to this occurrence. There are three ways the Orion BMS is capable of enforcing (dis)charge limits. The

first method of control is by using digital I/O signals. These I/O signals are Charge Safety, Discharge Enable, and Charge Enable, which are pins 6, 7, and 8 respectively on the BMS Main I/O connector. Only Charge Safety and Discharge Enable are relevant to the GEM because there are no energy generation mechanisms in the GEM. Use of the Discharge Enable signal is discussed in section 2.6.4, while Charge Safety is discussed in section 2.6.5. Charge Safety is only available in charge mode while Discharge Enable is available in both charge and discharge modes. Digital I/O signals are necessary to protect the battery pack but do not communicate limits to keep the vehicle functioning continuously. Four analog voltage signals are provided and can be scaled for the load they are controlling. The third method of (dis)charge control is by communication over CANbus, which allows for higher precision control. The ElCon charger is CAN enabled so the BMS can use this method communicate charge limitations. Since the motor controller is not equipped to communicate through CAN nor analog signals, the digital I/O control must suffice.

Measurements are critical to proper BMS function. The BMS measures the voltage across each cell within the battery pack, starting with the lowest cell potential, the negative terminal of cell one. Cell taps are wires connected across the battery pack to measure cell voltage. Voltage of cell one is measured as the difference in electrical potential between the negative and positive terminals of cell one and each additional cell voltage is measured between the potential of its positive terminal and the previous cell's positive terminal. After 12 cells, another cell tap is placed on the negative terminal, indicating the start of a new stack where the negative potential can be reestablished. This negative cell tap added every 12 cells is useful in determining the resistance of the busbar opposed to the internal cell resistance. Higher internal resistance of cells,

in comparison to cells of the same pack, usually means that the cell is weak; whereas, busbars with high impedance should be included in the compensation. Each cell group connector can connect to 36 cells, or three stacks. Should safety disconnects or fuses be inserted between cells, the fuse or disconnect should fall between cell group connectors else risk catastrophic damage or even injury with the breakdown of isolation. The voltage between consecutive cells must be between 0 VDC and 5 VDC, lest the Orion BMS internal protection diodes begin conducting [29].

3.4.1 Programming the BMS

A DB9 connector is placed in parallel with other electronics on the CAN1 CAN bus. With this connector in place, a CAN to USB converter (CANdapter) from Ewert Energy Systems can link a computer to the BMS. Another, though unused, option translates CAN bus to the OBD-II port. The BMS can only be programmed over CAN1, and to reduce the number of CAN systems being used, the ElCon charger also uses CAN1. However, since the ElCon charger only communicates at 250 kbps, all other electronics including computers must be set to that baud rate. Once a computer is connected, the current BMS settings can be downloaded and edited or a new profile can be uploaded. Live data can be displayed in the Orion BMS Utility software as text or graphs. In addition, there are tabs to view the battery profile, third party data, diagnostic trouble codes, and live CANBUS traffic.

3.4.1.1 Guided Battery Profile Generation

Whether just starting or still uncertain about the profile, the Orion BMS Utility software has a helpful guide called the Profile Setup Wizard that uses third party test data and datasheets to provide recommended settings. However, not all batteries have been tested thoroughly and data

may not be available, like shown in Figure 40. Hence, all settings should be reviewed for accuracy before uploading a profile.

The screenshot displays a 'Profile Setup Wizard' window. Under the 'Battery Selection' header, there are two dropdown menus: 'Battery Type' is set to 'GBS 40Ahr' and 'Current Sensor' is set to 'LEM DHAB S/24 (+/-500A)'. Below this is the 'Layout Configuration' section. It contains a 'Cells In Parallel' input field with the value '1' and a 'Cells In Series' section with a 'Configure Cells' button. Below the button, it says 'Loaded Cells: 24'. To the right of the text inputs are two circuit diagrams. The top diagram shows three battery cells connected in parallel, with their positive terminals joined at the top and negative terminals joined at the bottom. The bottom diagram shows three battery cells connected in series, with the positive terminal of one cell connected to the negative terminal of the next.

Figure 40: Profile Setup Wizard pop-up. The selection of “Battery Type” does not include GBS 60Ahr so GBS 40Ahr was chosen and settings were corrected [48].

The correct current sensor and cell layout configuration within the battery pack should be entered in the “Profile Setup Wizard.” Here, “Cells In Series” can be automatically populated if the BMS is programmed while connected to the cells [48]. Proceeding, the pop-up dialogue—shown in Figure 41—queries which thermistors are connected and which relay outputs will be used. Four thermistors are used, connected to the “Thermistor/Current Sensor” in accordance with Figure 13. Since there is scarcely enough room for the 24 cells within the battery box and battery drawer, it is unlikely that a fan would fit.

The image shows a software interface for configuring thermal and relay settings. It is divided into two main sections: 'Thermal Settings' and 'Relay Settings'.

Thermal Settings:

- Connected Thermistors: ☒ #1 ☒ #2 ☒ #3 ☒ #4
- ☐ Enable Fan Output

Relay Settings:

- ☐ Enable Charge-Enable Output
 - ☒ Turn off relay if current limit is exceeded
- ☒ Enable Discharge-Enable Output
 - ☒ Turn off relay if current limit is exceeded
- ☒ Enable Charger-Safety Output
 - ☒ Turn off relay if current limit is exceeded

Figure 41: The “Profile Setup Wizard” includes a simplified setup of thermistors and relay outputs for controlling loads [48].

Once the appropriate selections have been made, the next set of settings, shown in Figure 42, pertain to the baud-rate of each CAN bus and which third-party devices are enabled on either CAN bus. Here, CAN1 must be set to 250 kBps. Presently, the CAN2 baud-rate is inconsequential in the GEM. Only one third-party device is on the GEM CAN bus: the ElCon PFC charger. Hence, the “Elcon/Bestgo/TC Charger” option is selected under “Chargers” in Figure 42.

CANBUS Settings

CAN #1 Baud-Rate:250 kBit/sec

CAN #2 Baud-Rate:250 kBit/sec

Currently Connected To CAN #: 1, Baud: 250 kBit/sec

Please select which (if any) support for third party devices should be enabled.

Enable CANBUS Support For

Chargers

☒ Elcon / Bestgo / TC Charger
☐ Eltek Valere / Valeo Charger
☐ Current Ways / Brusa Charger
☐ Thunderstruck TSM2500 Charger
☐ Thunderstruck EVCC (Charger Controller)
☐ CHAdeMO Charging Protocol

Displays

☐ Andromeda EVIC Display

Figure 42: “Profile Setup Wizard” pop-up inquiring CANBUS settings and which third-party devices are enabled on the CANBUS [48].

After making the appropriate selections, the guide can be finished and uploaded to the BMS. It is recommended that this new profile is saved to an accessible computer location so adjustments can be made to the program without beginning anew. Incidentally, the BMS profile created by the “Profile Setup Wizard” still uses incorrect capacity values for the cells. Thus, capacity and current rate settings ought to be corrected before using the BMS in conjunction with the battery pack. Profile settings should be reviewed before accepting and uploading to the BMS.

3.4.1.2 Orion BMS General Settings

Charge Limits	Discharge Limits	Relays	Thermal Settings	Fault Settings
General Settings	Cell Settings	SOC Settings	CANBUS Settings	Addon Settings

General Settings

Current Sensor Selected	LEM DHAB S/24 (+/-500A)
Multi-Purpose Input Function	Clear Error Codes
Multi-Purpose Output Function	Error Signal Output
Turn MPO ON If Critical Fault	<input type="checkbox"/>
Invert Multi-Purpose Output Polarity	<input type="checkbox"/> Active HIGH
Pack Amp Hours [Ah]	60.00
Current Sensor Polarity Inverted	<input checked="" type="checkbox"/>
NOTE: Charging current should show up as negative (-)	
Always-On Power Source Not Used	<input checked="" type="checkbox"/>
Profile Password (Locking)	0 <input type="checkbox"/> Enabled

Help

Figure 43: “General Settings” tab of the “Battery Profile” page [48].

Generating a profile begins at the general settings, shown in Figure 43. Beginning at the top, the user selects which current sensor is connected to the BMS. Depending on the battery pack, several different Hall Effect sensors can be purchased with the Orion BMS; here, the GEM uses the LEM DHAB S/24 that measures up to 500 A. Current measurements can be seen in the Live Parameters tab at the top of the Orion BMS Utility window. Neither of the multi-purpose functions are used in the GEM, but the multi-purpose input (MPI) is set to clear error codes when 12 VDC is applied to pin 13 on the main I/O harness. Alternatively, the MPI could be set to maintain power if ready power is removed, alternate to a different preset charge current limit, or switch to a different minimum cell voltage. Next, the multi-purpose output (MPO) is set to

activate when there are error codes present. Just like other BMS outputs, power is not supplied by this output, but rather acts as an open drain to sink up to 175 mA of current when active. MPO supports numerous options, activating in the event there are certain error codes, battery limitations are reached, or when entering certain states. The pack capacity in Ah is defined by the batteries: the first LFP batteries were 40 Ah while the current battery pack is 60 Ah. Current sensor polarity is inverted if charging current measured by the sensor shows a negative value. Rather than reversing the Hall Effect sensor—removing it and replacing it 180° to its original direction—the polarity can be inverted. An always-on power source will not be used because that would be unnecessary power drain while the vehicle is not in operation. Finally, a profile password can be generated to prohibit undesired changes to the BMS profile.

3.4.1.3 Orion BMS Cell Settings

Entries under the second tab, “Cell Settings” in Figure 44, are determined by battery limitations and application requirements. Voltage recommendations are usually stated in the manual for the batteries. In general, the maximum and minimum cell voltages differ depending on whether the cell is being used individually versus in a pack. Individual cells often have higher maximum cell voltages and lower minimum cell voltages because an individual cell is respectively easier to watch. The cycle life of lithium-ion cells can be improved by designating a maximum cell voltage below the actual maximum voltage of the cell. Both overcharging and over-discharging should be avoided, but the depth to which a cell can be discharged is more variable. Usable capacity of a cell is not greatly diminished by ending charge and discharge slightly early. For lithium-ion batteries, the voltage greatly increases when nearly fully charged and rapidly declines when nearly depleted.

Charge Limits	Discharge Limits	Relays	Thermal Settings	Fault Settings
General Settings	Cell Settings	SOC Settings	CANBUS Settings	Addon Settings

Voltage Settings

Resistance Settings

Cell Voltage Limits

Maximum Cell Voltage

?

3.550

Volts

Minimum Cell Voltage

?

2.800

Volts

Max Cell Voltage While Charging

?

3.550

Volts

Configure Which Cells Are Connected (Populated)

Balance Settings

☒ Enable Cell Balancing

Start balancing if at least one cell is above

3.500

Volts

Stop balancing when all cells are within

0.020

Volts

Never balance individual cells below

3.200

Volts

Pack Voltage Limits

☒ Limit based on individual cell voltages
☐ Limit based on cell voltages AND pack voltage

Maximum Pack Voltage

Disabled

Volts

Minimum Pack Voltage

Disabled

Volts

Max Pack Voltage While Charging

Disabled

Volts

Figure 44: “Voltage Settings” are set in the “Cell Settings” tab. Voltage limits are enforced during charge and discharge to avoid damaging the cells but are not the only conditions influencing these decisions [48].

For example, the 40 Ah LiFePO₄ cells would be at approximately 80% depth of discharge (DOD) when at 3.1 VDC but could still be discharged until 2.0 VDC before permanent damage would likely onset. The absolute minimum voltage for the 60 Ah batteries is roughly 2.0 VDC; here, any further discharge and the batteries will likely be permanently damaged and unusable. Discharge of individual cells ought to end at 2.5 VDC while the minimum cell voltage in a battery pack should not fall below 2.8 VDC. Maximum cell voltage as stated in the GBS 60 Ah battery manual is 3.6 VDC; however, there is a voltage limitation for the original GEM motor controller of 86 VDC. Exceeding 86 VDC across the battery pack is not expected to damage any

of the electronics, but the EMC controls will suspend and error code 16 will be shown on the LCD dash display [13]. With measures taken to keep the maximum battery pack voltage below the limit, it does not seem necessary to limit based on pack voltage. Coincidentally, the third-party data lists a maximum voltage of 3.55 VDC which meets the EMC maximum voltage criteria.

Below the cell voltage limits, there is a button to choose which cells are populated. It is quicker to select the “Automatically Populate” button as that will fill in the boxes based on which batteries have a measurable voltage. The table should already be populated if it was filled during the Profile Setup Wizard. Incorrect wiring or other faults may result in cells not appearing correctly in the list, which ought to be corrected. If a cell is not appearing, check to see that the cell taps have been firmly connected in their proper order, the cells are all above 0 VDC, and ensure there are no short circuits. Once the cells are populated and the associated voltage measurements are correct, the busbar compensation can be entered. The busbars that were provided with the 40 Ah LFP cells have a resistance of approximately $0.3\ \Omega$ while those for the 60 Ah LFMP cells have a resistance of approximately $0.2\ \Omega$. These are relatively low resistances and when busbars are shorter than four inches with consistent sizing, the busbars are typically ignored. Resistance compensation is important for battery pack layouts that have longer or irregular busbars, like the custom busbar shown in Figure 21. Because the custom aluminum busbar had a higher resistance than the conventional busbars, the added resistance was entered in $m\Omega$ to the cell population table. With all pertinent values entered, apply changes and begin balance settings.

Reiterating from before, cells do not need to be balanced every cycle. When the cells are balanced is decided by the user; recall, imbalance will decrease the available capacity of the

battery pack. Moreover, the time required to correct the imbalance is another consideration. Since the Orion BMS can only discharge 200 mA per cell, correcting for a 1% loss of capacity in the 60 Ah battery pack would require approximately three hours presuming there is sufficient cooling of the BMS. In comparison, the recommended charging rate of the 60 Ah batteries is anywhere from 0.25 C-rate to 0.5 C-rate, corresponding with four-hour and two-hour charging times, respectively. The Orion BMS recommends balancing cells to a delta voltage (ΔV) within 0.01 VDC, though many factors affect how voltage correlates to SOC. Instead, the ΔV of 0.02 VDC will be adopted since that is the recommended value for GBS 40Ahr cells [48].

Without testing the 60 Ah batteries themselves or determining how usage within the GEM unbalances the batteries, it cannot be determined how frequently the batteries will need to be balanced. Using a practical time limit placed on the duration the vehicle could charge and balance before it had to return to service (i.e., no more than 12 hours) and using the upper recommended charge rate of 0.5 C-rate, ideally the BMS could correct 2 Ah or 3.3% loss of capacity. Using the recommendations in the Orion BMS manual, the voltage at which LFP cells should start balancing is close to 3.5 VDC since this is when the cell is within 5-10% of the maximum SOC. Cells below 3.20 VDC will not be further discharged when balancing. The lower threshold for balancing should be set to below the settling voltage.

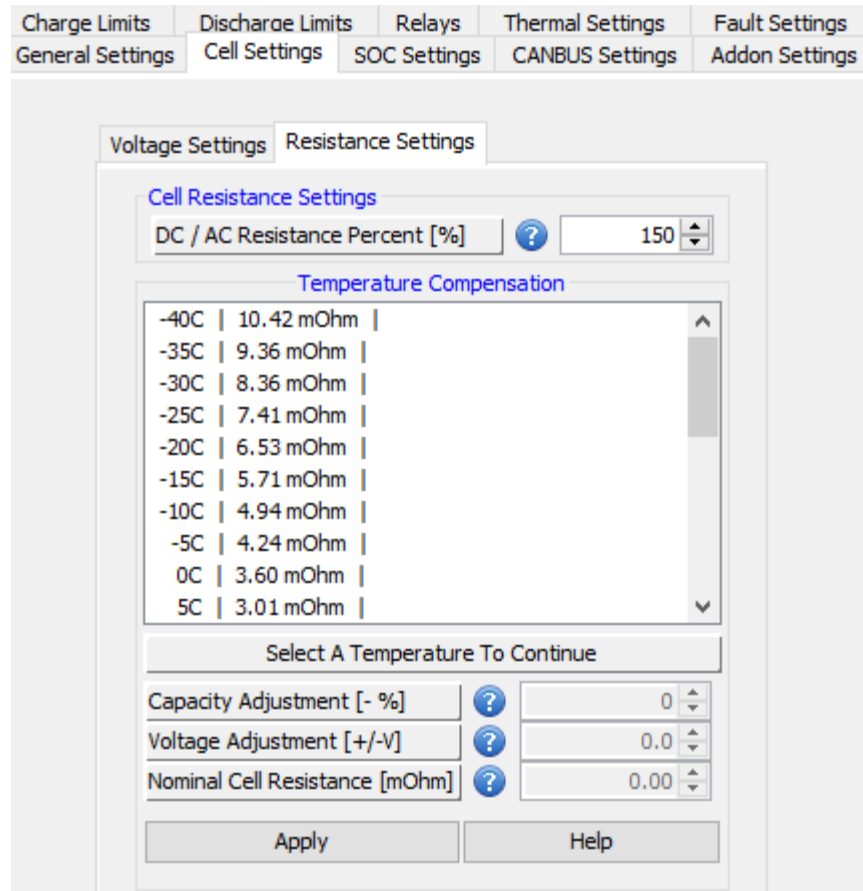


Figure 45: BMS cell resistance settings tab with values used in the GEM profile [48].

Within the “Cell Settings” tab, besides “Voltage Settings” there is a “Resistance Settings” page, as seen in Figure 45. These values have not been changed from the “Profile Setup Wizard” recommendations simply because there are no data to support changes. Cell resistance and behavior resulting from temperature have not been measured, nor did the Orion BMS Utility have values for this capacity battery.

3.4.1.4 Orion BMS SOC Settings

Charge Limits	Discharge Limits	Relays	Thermal Settings	Fault Settings
General Settings	Cell Settings	SOC Settings	CANBUS Settings	Addon Settings

SOC Settings

Charged SOC [%] 95

Discharged SOC [%] 10

SOC Drift Points

Drift #1: 2.90v -> 10% (DOWN)

Drift #2: 3.00v -> 20% (DOWN)

Drift #3: 3.45v -> 80% (UP)

Drift #4: 3.53v -> 95% (UP)

Drift #5: 0.00v -> 0%

Drift #6: 0.00v -> 0%

Drift #7: 0.00v -> 0%

Drift #8: 0.00v -> 0%

Select A Drift Point To Continue

Pack SOC To Drift To [%] 0

Cell Voltage For Drift [V] 0.000

☐ SOC only corrected DOWN based on this point

☐ SOC only corrected UP based on this point

Apply Clear Point Help

Figure 46: SOC settings and SOC drift points used in the GEM profile [48].

The Orion BMS calculates SOC using the coulomb counting method, which will be discussed in finer detail in Section 4.4.1. Here, the BMS State of Charge settings are shown in Figure 46. In specific, the “Charged SOC” does not control when the batteries ought to stop charging. Instead, it is used to calculate the SOH of the battery pack by comparing the observed capacity of the battery pack to an expected capacity. The percentage of the expected capacity that the observed capacity attains at full charge should be at least the “Charged SOC”. If the observed capacity is greater than the expected capacity, either the expectation was set too low or the cell voltage settings were set to charge and discharge the battery to a greater extent than expected. For properly adjusted settings and a healthy battery pack, the observed capacity should be about

equal to the expected capacity. As batteries age, the observed capacity will decline in relation to the expected capacity. Similarly, the “Discharged SOC” describes the percentage of capacity a cell should have remaining when considered fully discharged. Again, this is used to compute the battery pack SOH.

The “SOC Drift Points”, shown in Figure 46, are used to correct the state of charge to correspond to a voltage profile. One drift point designates that the battery pack is at 100% SOC when the voltage is at the maximum voltage set in Cell Settings. There is an absolute capacity of a battery, but the start and finish points of a cycle are redefined to keep a battery from over-charging or over-discharging. The SOC described by drift points describe how much capacity has been used of the portion set aside to be used. Since voltage is directly measurable, unlike SOC, and SOC is linked to voltage, voltage can be related to SOC when considering certain factors. Moreover, it is because of other factors that the voltage at a certain state of charge may not be the same every time. A battery that has been discharged at a high current rate may not discharge the full expected capacity, but it still must stop discharging once the cells hit a minimum voltage. Hence, when a cell drops to 2.9 VDC yet has not reached 90% DOD, the SOC drift point corrects the DOD to 90%. In this case, the SOC drifts downwards. Contrarily, the SOC drifts upwards when charging at a high rate. Though the voltage may reach the fully charged threshold when charging quickly, the cell voltage only indicates the available charge. The cell voltage will decrease as it rests as lithium ions diffuse into the anode, subsequently after which, charging can resume.

3.4.1.5 Orion BMS CANBUS and Addon Settings

The screenshot displays the 'CANBUS Settings' tab within a software interface. At the top, there are several tabs: 'Charge Limits', 'Discharge Limits', 'Relays', 'Thermal Settings', 'Fault Settings', 'General Settings', 'Cell Settings', 'SOC Settings', 'CANBUS Settings' (which is active), and 'Addon Settings'. The 'CANBUS Settings' section contains the following fields:

- CANBUS #1 Frequency [Kbps]: 250 kBit/sec
- CANBUS #2 Frequency [Kbps]: 250 kBit/sec
- OBDII ECU Identifier: 0x7E3
- Enable Battery Cell Broadcast: ☐
- Battery Cell Broadcast Interface: CANBUS #1
- Battery Cell Broadcast Identifier: 0x0

Below these fields is a button labeled 'Edit CANBUS Messages'. Underneath is a list of components categorized into three groups:

- Chargers:**
 - ☒ Elcon / Bestgo / TC Charger
 - ☐ Eltek Valere / Valeo Charger
 - ☐ Current Ways / Brusa Charger
 - ☐ Thunderstruck TSM2500 Charger
 - ☐ Thunderstruck EVCC (Charger Controller)
 - ☐ CHAdeMO Charging Protocol
- Displays:**
 - ☐ Andromeda EVIC Display
- Motor Controllers:**
 - ☐ Netgain Motor Controller
 - ☐ HPEV Curtis 1238/1239 (CAN)
 - ☐ Toyota Prius Gen2

A 'Help' button is located at the bottom center of the window.

Figure 47: CANBUS Settings tab of the BMS GEM profile [48].

The CANBUS settings, shown in Figure 47, do not require much involvement. As required by the ElCon charger, the CAN1 frequency is set to 250 kbps. Since CAN2 is not in use, frequency is not important. Besides these two selections, the ElCon charger is selected under the Chargers category. The GEM does not contain any CAN enabled displays or motor controllers at this time, but an Orion Basic Display module is available for use once the vehicle has been set up.

Charge Limits	Discharge Limits	Relays	Thermal Settings	Fault Settings
General Settings	Cell Settings	SOC Settings	CANBUS Settings	Addon Settings

Addon Settings

Enable Thermistor/ Expansion Modules	?	<input type="checkbox"/>
Thermistor Broadcast CANBUS Interface	?	CANBUS #1
Thermistor Broadcast CANBUS Identifier	?	0x0
Number of Thermistor Expansion Modules	?	0
Enable Data Logging Display Module	?	<input type="checkbox"/>
Data Logging Display Module CAN Interface	?	CANBUS #1
Simulate ECM (For Scantool)	?	Disabled
BMS Unit Type (Master/Slave)	?	Single Unit (None)
<div style="border: 1px solid #ccc; display: inline-block; padding: 2px 10px;">Edit Prius Settings (Only Used For PHEV Conversions)</div>		

Help

Figure 48: GEM BMS profile Addon Settings tab and selections [48].

Furthermore, Addon Settings, shown in Figure 48, are configured for additional modules interacting with the BMS. Here, CAN1 should be selected for the Thermistor Broadcast Interface and Data Logging Display Module Interface. Only one BMS unit is used and a thermistor expansion module is not used. Fortunately, the battery pack only contains relatively few cells compared to full-size EVs; thus, a single BMS unit suffices.

3.4.1.6 Orion BMS Charge Limits

The screenshot displays the Orion BMS configuration interface, specifically the 'Charge Limits' tab. The interface is organized into several sections:

- General Settings:** Includes tabs for General Settings, Cell Settings, SOC Settings, CANBUS Settings, Addon Settings, Charge Limits (selected), Discharge Limits, Relays, Thermal Settings, and Fault Settings.
- Basic Limit Settings:** This section is active and contains:
 - Maximum Charge Current Limits:** Includes fields for 'Maximum Continuous Charge Limit [A]' (set to 30), 'Maximum Analog Output CCL [A]' (set to 30), and 'Maximum Amperage While Charging [A]' (set to 30). A checkbox for 'Stop all charging when SOC reaches' is set to 95%.
 - Derate for Temperature:** Includes fields for 'Start reducing current limit when pack is warmer than' (40 °C), 'Reduce maximum possible limit by' (5 Amps per °C), 'Start reducing current limit when pack is cooler than' (15 °C), 'Reduce maximum possible limit by' (7 Amps per °C), and 'Never reduce limit below' (0 Amps for temperature alone).
 - Derate for State of Charge:** Includes fields for 'Start reducing current limit at' (95 % State of Charge (SOC)) and 'Reduce maximum possible limit by' (10 Amps per % SOC).
- Help:** A button at the bottom of the interface.

Figure 49: GEM BMS Charge Limits profile showing the Basic Limit Settings [48].

Within the “Charge Limits” tab there are three subsections, the first of which is the “Basic Limit Settings” that are shown in Figure 49. In this tab, the “Maximum Continuous Charge Limit” (CCL) is set to 30 A since that is the highest allowable continuous charge current. However, the ElCon charger is limited to 16 A maximum output which is even less likely to cause lithium-plating on the anode, as discussed in section 3.3.3.3. While the BMS does not use analog outputs in the GEM, settings can be entered to facilitate future expansions or changes. Setting the Maximum Analog Output CCL to 30 A will give the output more range: signaling to charge at

16 A would be approximately 2.7 VDC out of a maximum 5 VDC signal. The amperage while charging is set to 30 A because the only time the battery pack will be charging is during Charge Mode. Regenerative braking and other possible charging methods applied during Ready Mode are not enabled within the GEM. Charging is not completed based on a calculated SOC in this application; i.e., charging ends when cells reach their maximum voltage. However, charge current is reduced based on SOC and temperature. Charge current is de-rated by 5 A for every degree Celsius increased starting at 40 °C. The cells are rated to charge at temperatures up to 65 °C, but charge operations will be limited to 46 °C. While the ElCon charger cannot charge at the maximum charge current of 30 A, the BMS still begins to de-rate current starting at 30 A until 0 A as the temperature rises from 40 °C to 46 °C. Though 46 °C is far below the temperature of SEI breakdown, 120 °C, which can evolve into thermal runaway, SEI formation increases with elevated temperatures. As discussed in section 3.3.3.4, SEI formation reduces the capacity of the cell and increases the internal resistance, which in turn increases voltage hysteresis and resistive heating. Since the GEM has been indoors, the ambient temperature will not contribute to over-heating. The GEM cannot actively cool the batteries but the BMS can disable charging to avoid contributing to battery damage. However, it is prudent to reduce the allowable ambient temperature when outside as resistive heating may increase the internal temperature above the desired limit.

Charging at low temperatures must be stringently restricted to prevent damaging the 60 Ah LFMP cells and to avoid conditions that befell the 40 Ah CALB cells. In general, lithium iron phosphate cells should never be charged at below freezing temperatures, lest risk lithium plating and dendrites. Charging current will always be low, which mitigates one factor that section

3.3.3.3 mentioned encourages dendrite formation. Unfortunately, late fall and winter temperatures can frequently fall below freezing in Kansas; hence, vehicle utility will be reduced unless the vehicle is stored or charged in a heated environment. The onset temperature and rate of current reduction in Figure 49 are those suggested by the Profile Setup Wizard. Current de-rating will begin at 15 °C. The CCL will reduce at 7 A/°C, with charging shut off at 10 °C. It is still not recommended to charge the batteries while they are at these cold temperatures. According to the GBS cell operation manual, the LFMP cells retain 78% of their original capacity at 0 °C. Since the BMS determines when to stop charging based on voltage, and assuming the SOC Settings are correct, de-rating CCL based on SOC is not necessary. If the batteries have not yet attained maximum voltage but have reached 95% SOC, CCL will be reduced at 10 A/% SOC.

Timer Settings		
Voltage Derate CCL To Zero Timer [Seconds]	?	0.1
Voltage Restore CCL Timer [Seconds]	?	1.0
Voltage Failure Derate Timer [Seconds]	?	9.0
Peak Current CCL Increment Timer [Seconds]	?	1.0
Peak Current CCL Decrement Timer [Seconds]	?	3.0
Peak Allowable CCL Percentage [%]	?	30

Figure 50: Default GEM BMS profile Charge Limits Failsafe settings after completing “Profile Setup Wizard [48].”

Overall, pulse charging will not be used within the GEM. While pulse charging may decrease the charging duration, there is no need to further complicate the charging process. The charger failsafe is comprised of several timers, shown in Figure 50. The “Voltage Derate CCL to Zero Timer” is the duration the charging voltage can exceed the charging voltage limit before the charging current is reduced by 10% of the CCL. This voltage can be exceeded for 0.1 s, which

should be sufficient for such a spike to clear. Next, the “Voltage Restore CCL Timer” is the duration that the charging voltage does not exceed the voltage limit before CCL is restored to the max CCL. Additionally, this parameter describes the duration that the voltage sensor must be functioning again after a critical voltage sensing failure before battery charging current can be restored. The “Voltage Failure Derate Time” is the interval between when a critical voltage sensing fault is detected and when CCL is reduced by 10%. Once ten intervals have passed, charging current will be halted to protect the batteries. Following the voltage-related settings are the current limit failsafe settings, starting with “Peak Current CCL Increment Timer.” This timer sets a duration at which the peak current limit can be sustained before a diagnostic trouble code is issued. Peak charge current limit is calculated as the sum of the maximum charge current and the charge current allowed by the peak charge current limit percentage. Peak charge current limit percentage is a parameter within Relay Settings. This Peak Current CCL Decrement Timer is the time it takes for the peak current counter to return to zero after the current limits are no longer being exceeded. Finally, the “Peak Allowable CCL Percentage” is the percentage of CCL that can be exceeded before there is an error or fault.

3.4.1.7 Orion BMS Discharge Limits

The screenshot shows the Orion BMS configuration interface. At the top, there are tabs for General Settings, Cell Settings, SOC Settings, CANBUS Settings, and Addon Settings. Below these are sub-tabs for Charge Limits, Discharge Limits, Relays, Thermal Settings, and Fault Settings. The 'Discharge Limits' sub-tab is active. Within this sub-tab, there are three sub-sections: 'Basic Limit Settings', 'Pulse Limit Settings', and 'Failsafe Settings'. The 'Basic Limit Settings' section is expanded, showing 'Maximum Discharge Current Limits'. It includes a 'Maximum Continuous Discharge Limit [A]' set to 90, a note about the actual limit being lower, and a 'Maximum Analog Output DCL [A]' set to 120. Below this is a 'Derate for Temperature' section with settings for reducing the limit when the pack is warmer than 40 °C (11 A/°C) and cooler than 20 °C (6 A/°C), with a floor of 0 A. Finally, there is a 'Derate for State of Charge' section with settings for reducing the limit at 10 % SOC (14 A/% SOC). A 'Help' button is at the bottom.

Setting	Value	Unit
Maximum Continuous Discharge Limit	90	A
Maximum Analog Output DCL	120	A
Start reducing current limit when pack is warmer than	40	°C
Reduce maximum possible limit by	11	Amps per °C
Start reducing current limit when pack is cooler than	20	°C
Reduce maximum possible limit by	6	Amps per °C
Never reduce limit below	0	Amps for temperature alone
Start reducing current limit at	10	% State of Charge (SOC)
Reduce maximum possible limit by	14	Amps per % SOC

Figure 51: Basic discharge current limit (DCL) settings in the GEM BMS profile [48].

The discharge limit settings, shown in Figure 51, are set up nearly identically to the charge limit settings. The “Maximum Continuous Discharge Limit” is 90 A, which must be lower than the battery pack fuse rating. The discharge current limit (DCL) is restricted to under 100 A by the battery pack protection fuse and by the MDS, which will shut if that current limit is exceeded. The “Maximum Analog Output DCL” is set to 120 A to allow more current if it becomes available. This value can be larger than the actual vehicle limitations for the time being because the analog output is not in use. Like charging current, discharge current is also derated based on temperature and SOC. Discharge is null by 49 °C, but begins decreasing beyond 40 °C at a rate of 11 A/°C. The values in Figure 51 reflect the recommendations of the Profile Setup Wizard based on the GBS 100Ahr battery. Again, the working temperatures listed in the GBS 60 Ah

operation manual exceed the Profile Setup Wizard recommendations. The manual specifies working discharge between -20 °C and 65 °C, while the profile guide enables discharge between 5 °C and 49°C. Though it appears to be an inconsistency, it is equally likely that the values differ based on performance expectations. The battery performance will be stronger and more consistent during the limited temperature range and slows the rate of damage to the battery. Only if necessary for the intended function of the GEM would the derating onset temperatures be reduced. Even then, charging is inadmissible below freezing and it should be understood that the vehicle capabilities will be reduced for both temperature extremes. The rate of discharge at low temperatures is reduced because diffusion is slowed. Though capacity remains after high rate discharge, over-discharging can lead to dissolution of iron from the positive electrode, especially at high temperatures. High temperatures, regardless whether charging or discharging, will promote the breakdown of the electrolyte and dissolution of the cathode. Since discharge proceeds at often higher current rates, resistive heating has the potential to be a greater issue.

Timer Settings		
Voltage Derate DCL To Zero Timer [Seconds]	?	0.1
Voltage Restore DCL Timer [Seconds]	?	1.0
Voltage Failure Derate Timer [Seconds]	?	9.0
Peak Current DCL Increment Timer [Seconds]	?	1.0
Peak Current DCL Decrement Timer [Seconds]	?	3.0
Peak Allowable DCL Percentage [%]	?	30

Figure 52: GEM BMS DCL Failsafe settings entered by the Profile Setup Wizard [48].

The “Timer Settings” for the DCL failsafe, shown in Figure 52, function just like the timer settings for the CCL failsafe. With these values, there is the concern that a 30% “Peak Allowable DCL Percentage” will result in blowing either the battery pack fuse or the MDS fuse. However,

it is preferred that the battery pack fuse blows first, and very well may since it does not have a time-delay.

3.4.1.8 Orion BMS Relays Settings

Two of the three available relays are used in the GEM: “Charger Safety” and “Discharge Enable.” Relays can be enabled or disabled either in the “Profile Setup Wizard” or in the “Relays” tab while making profile changes. Charger Safety settings for the GEM BMS are seen in Figure 53 while the “Charger Safety Functional Flowchart” is included in the Appendix, Figure 78. When the BMS receives power through the Charge Power pin, the BMS enters Charge Mode. The flowchart illustrates the conditions that engage and disengage the Charger Safety pin, where engaged means that the BMS is sinking current and disengaged means that there is no current flow. Since the ElCon charger cannot charge above 16 A, the charger will never exceed maximum CCL. However, if CCL drops below 16 A, the new charging rate ought to be shared with the charger across CAN1. If the charger does not heed the CCL, charging will continue until CCL drops to zero. The Charger Safety is also disengaged when there are fatal DTCs and while the BMS is balancing cells. The relay, when disengaged, must remain disengaged for only one second before it can be reengaged, if conditions apply. While the cells remain out of balance, Charger Safety will engage every 15 min to ensure cells reach full charge and that enough time has been given for cells to approach OCV and undergo balancing.

General Settings	Cell Settings	SOC Settings	CANBUS Settings	Addon Settings
Charge Limits	Discharge Limits	Relays	Thermal Settings	Fault Settings

Charger Safety
ENABLED

Charge Enable
DISABLED

Discharge Enable
ENABLED

Charger Safety Behavior

☒ Enable charger safety relay output

☒ Trip relay off only when charge current limit hits 0 amps
☐ Trip relay off if charge current limit hits 0 amps OR pack current exceeds charge current limit by: %

Max time [minutes] that relay can stay on

After Charge Is Complete

By default output will remain off until Charge Power is re-applied

☒ Turn relay output back on every minutes

☐ Re-enable relay when SOC is below %
AND at least minutes have elapsed

Other Options

Figure 53: Charger Safety relay settings in the Orion BMS GEM profile [48].

Unlike the charger, to which the BMS can convey CCL over CAN, the vehicle discharges with disregard for the DCL until the BMS shuts off power. Settings for the Discharge Enable relay are shown in Figure 54, which are applied according to the “Discharge Enable Functional Flowchart”, shown in the Appendix, Figure 79. Discharge Enable is disengaged if the BMS sets DCL to zero amps or if the vehicle exceeds DCL by 10%. At the current maximum DCL, much beyond 10% would exceed the current rating of the battery pack fuse. The Discharge Enable settings were chosen to keep the vehicle functioning without removing power for as long as possible without damaging the GEM electronics. Once discharge is cutoff, so long as DCL is greater than zero amps, the GEM should regain power after only a second of lapse.

General Settings	Cell Settings	SOC Settings	CANBUS Settings	Addon Settings
Charge Limits	Discharge Limits	Relays	Thermal Settings	Fault Settings

Charger Safety ENABLED	Charge Enable DISABLED	Discharge Enable ENABLED
----------------------------------	----------------------------------	------------------------------------

☒ Enable discharge enable relay output

- ☐ Trip relay off only when discharge current limit hits 0 amps
- ☒ Trip relay off if discharge current limit hits 0 amps
OR pack current exceeds discharge current limit by: %

Allow relay to turn back on after 1 second(s) if:

☒ Discharge current limit is above Amps

OR

☐ State of charge goes above %

☒ Require READY power (Main I/O Pin 2) to turn relay output on.

☒ Turn relay off if both CHARGE and READY power are both energized (charge interlock condition).

☐ Latch Discharge Limit At 0A When Discharge Enable Is Off

Other Options

☒ Minimum time relays are off (seconds)

[View Help & Relay Flowcharts](#)

Figure 54: Orion BMS Discharge Enable relay settings for the GEM [48].

3.5 Discussion

The BMS can derate current and shut down the battery pack before it is damaged by high temperature but there is nothing in place to decrease cell temperature and prolong discharge and charge. Utilizing a fan in the battery pack only cools the cells when the ambient temperature is at a lower temperature than the cells themselves. A fan does help evenly distribute heat amongst cells which evens out the rate at which the cells age. Unfortunately, there is not enough room within the battery pack or battery box for a fan. The battery pack can be cumbersome to carry

with two people given its weight and size; modifications to the battery drawer, discussed in Section 2.6.2.1, were required since the length of the battery pack made its removal from the vehicle difficult. Considering the issues involving battery pack size, expanding the battery pack to allow room for air flow is not feasible. Since there are four rows and six columns of cells, as seen in Figure 25, there are eight cells which are surrounded on four sides by other cells. These eight cells will likely be at elevated temperatures when the ambient temperature is lower than the cell temperature and considering that cells generate heat. If the battery box is at a constant temperature throughout—specifically that the front or back of the battery box is not at a higher temperature than either side or contrariwise—then the cells on the top and bottom rows will have the best heat transfer. During the lifetime of the battery pack, the cells will age at different rates; it will be interesting to see if the ageing discrepancies seem to result from cell position within the pack. If it seems to be the case where the inner cells are suffering increased internal resistance and reduced capacity, it would be prudent to rearrange the cells within the pack so that the inner cells are moved to the outside.

3.6 Conclusion

In consideration of the swappable battery pack aspect of the GEM, it would seem more appropriate to have all battery specific electronics as a single unit that would be removable from the vehicle. This would reduce the time needed to swap battery packs since the Orion BMS situated in the GEM would need a new profile uploaded when the new pack is installed. Furthermore, utilizing a BMS to control charge, maintain cell balance, and maintain battery measurements while the battery pack is not in use is highly advised. Battery management and

vehicle function could improve through replacing the GEM EMC, PSDM, LCD display, and associated electronics with components that can be integrated more effectively.

The effect of BMS settings on vehicle functionality will not be fully understood until the GEM is operational. It is anticipated that as long as the rated capacity of the cells is sufficient such that even when capacity is reduced due to the conditions of use, the battery pack still provides adequate performance, vehicle performance will not necessarily impact battery pack health. Moreover, as long as the vehicle is being used within reason, the battery pack ought to remain healthy. Overall, the limitations of lithium-ion batteries are more apparent than lead-acid batteries because lithium-ion batteries fail at extrema in temperature, SOC, and discharge rate that lead-acid batteries can better handle. By appropriately sizing the battery pack and utilizing safety devices, battery pack failure can be averted and the apprehension behind lithium-ion batteries disappears. Still, without testing the battery pack in the GEM, it is difficult to judge the efficacy of BMS provisions. Vehicle modeling, like the subject of Section 2.4, when used alongside battery models can inform design decisions. Depending on the comprehensiveness of the models, it should be possible to foresee and counteract problems.

4 Battery Modeling for Electric Vehicles

4.1 Abstract

For battery management and typical vehicle use there are a few important states; in Chapter 4, the battery models used to estimate the condition of batteries are discussed. While fundamentally battery behavior is electrochemical, commercial cells are sealed and opening would destroy them. Thus, the internal state must be understood indirectly through measurable attributes such as terminal voltage, current, and temperature. Various different testing methods are presented, which also demonstrates particular interesting aspects of battery discharge behavior that may require special attention. Keeping in mind the goal of modeling and which measures are available, different mathematical models frequently found in the literature are introduced. Each model attempts to describe battery behavior without becoming exceedingly complicated. Simple models can be quite accurate but require much more data to train them, while more complicated models may provide an adequate estimation with less effort in parameterization. To demonstrate model accuracy and suitability when used for certain cell chemistries, a few models are combined and parameterized for a variety of cells.

Nomenclature

Variable	Description	Units
C_0	Original Capacity of Cell	[Ah]
C_1	Thévenin Capacitance	[F]
C_2	Second RC Pair Capacitance	[F]
C_{DL}	Double-Layer Capacitance	[F]
C_P	Rate-Specific Capacity	[Ah]
C_R	Capacitance of Reaction	[F]
C_S	Surface Capacitance	[F]
C_W	Warburg Capacitance	[F]
C_b	Bulk Capacitance	[F]
C_n	Cell Capacity	[Ah]
C_t	Current Cell Capacity	[Ah]
E_0	Cell Potential	[VDC]
K_0	Combined ECM Constant	[VDC]
K_1	Shepherd Constant	[VDC]
K_2	Unnewehr-Nasar Constant	[VDC]
K_3	Nernst ECM Constant	[VDC]
K_4	Nernst ECM Constant	[VDC]
Q_n	Maximum Rated Cell Capacity	[Ah]
R_0	Internal Resistance	[Ω]
R_1	Thévenin Resistance	[Ω]
R_2	Second RC Pair Resistance	[Ω]
R_C	Electrolyte Resistance	[Ω]
R_R	Resistance of Reaction	[Ω]
R_S	Series Resistance	[Ω]
R_S	Surface Resistance	[Ω]
R_b	Bulk Resistance	[Ω]
R_{ct}	Charge Transfer Resistance	[Ω]
R_{sq}	Coefficient of Determination	[—]
V_{OC}	Open Circuit Voltage	[VDC]
V_{res}	Model Voltage Results	[VDC]
Z_W	Warburg Impedance	[Ω]
ΔC_r	Incremental Change of Capacity	[Ah]
h	Hysteresis Voltage	[VDC]
C	Capacitance	[F]
CPE	Constant Phase Element	[Ω]
G	Equation Matrix	[—]
I	Current	[A]
M	Value of Hysteresis	[VDC]
R	Equivalent Cell Resistance	[Ω]
SOC	State of Charge	[%]

SOH	State of Health	$[-]$
T	Temperature	$[K]$
V	Terminal Voltage	$[VDC]$
X	Column Vector of Variables	
Z	State of Charge	$[\%]$
i	Current	$[A]$
k	Peukert's Constant	$[-]$
n	Discrete Time Step	$[-]$
s	Direction of Current	$[-]$
t	Time	$[s]$
α	Current Offset Constant	$[-]$
α	Coulombic Efficiency	$[-]$
β	Temperature Offset Constant	$[-]$
γ	Enhanced Peukert Proportionality Constant	$[A]$
γ	Rate of Hysteresis Voltage Decay	$[-]$
η	Coulombic Efficiency	$[-]$
τ	Variable of Integration	$[-]$

4.2 Introduction

Battery models are helpful tools for approximating the current state of the battery and its future behavior. Over time, the preferred models have changed as more accurate methods have been proven and technology has improved. However, the desired function of the model remains the same: using measurements and conditions to determine states. While there may be some variation on which outputs are desired, battery models suited for EVs generally focus on terminal voltage, state of charge (SOC), state of health (SOH), state of power (SOP), state of function (SOF), remaining useful life (RUL), and temperature [49].

Occasionally, battery models might be used to detect or prevent faults. These outputs serve a purpose: to provide information pertinent to battery management and safe, effectual vehicle operation. Applicability and effectiveness of a model is determined based on several considerations. The selected battery model should be capable of providing the desired outputs

with reasonable accuracy and timeliness. Furthermore, implementation of the model is another key consideration. This requires proper measurement devices to provide model inputs, computational power and digital storage space, equipment to characterize the cells and parameterize the model while also affording the time to update the model. In addition, there are limitations on what measurement equipment is available and how often the battery model can be parameterized. Measuring current, voltage, and external temperature is common, but frequent testing like the hybrid pulse power characterization (HPPC) test or Electrochemical Impedance Spectroscopy (EIS) takes specialized equipment and time. For a vehicle that is not serviced frequently, online estimation and characterization are important attributes. Such degree of self-sufficiency requires integration and might require more processing power. Unfortunately, there is usually a trade-off between model accuracy and complexity. As a result, battery modeling in EVs, due to power and space limitations, benefits from simple models capable of simulating battery dynamics without necessarily accounting for the details of battery behavior.

4.3 Battery Evaluation Considerations

Setting up a battery model for EV usage is different than models used to design EVs or even improve cell design. Battery models used in EVs often rely on current, terminal voltage, and external temperature measurements. Depending on the style of BMS, internal resistance values are also available and while the exact number of cycles or age of the cell is not usually known, it can be readily approximated. Moreover, if the cells are balanced at a specific SOC, then the SOC is known. Here, SOC is the percentage of remaining charge out of the charge at full capacity, the rated capacity specified by the manufacturer. The value of SOC is of paramount importance to consumers relying on electronics and/or EVs because it encapsulates the information desired by

battery consumers: i.e., how much longer the battery can be used before it needs to be charged.

In addition, SOC is an important parameter in battery management; not just because it is important to EV operators but balancing the SOC of cells in a battery pack increases the available capacity so that it is limited only by the cell with the lowest capacity. In contrast, absolute cell capacity decreases over its cycle and calendar life; whereas, available capacity changes with rate of discharge and temperature. Overall, there are several methods of estimating SOC; however, only some of which are practical for EVs.

Similar to SOC, Depth of Discharge ($DOD = 1 - SOC$) is the percentage of the full capacity that has been discharged. Efforts to standardize battery capacity have redefined DOD in some cases to refer to the charge delivered by the battery. Redefining DOD in this manner insightfully incorporates an often-neglected detail associated with constant current (dis)charge: even though a cell may reach 0% SOC, charge may still be available within the cell when discharged at a lower rate. Generally, SOH relays the capacity of the battery pack as its capacity is reduced when the battery ages or is damaged. In comparison, SOP is the ability of the battery to provide power and becomes simply a yes or no statement. More complicated is the SOF, which determines the available capacity and the change to overall capacity of a cell. Lastly, RUL predicts the number of cycles remaining before the battery must be decommissioned. Since none of these states are directly measurable, they are defined in relation to what can be measured: terminal voltage, current, external temperature, internal impedance, and time.

Of the methods applicable in EVs, only those capable of high accuracy under dynamic loads and variable conditions are suitable for use. Since batteries are electrochemical by nature, an electrochemical model would be most apt for battery modeling. As a result, electrochemical

battery models have the greatest potential for accurate predictions and are capable of far more than determining the SOC. Unfortunately, electrochemical models are computationally expensive and prohibitively time-consuming for use in EVs [50, 51]. Specifically, there are too many partial differential equations and unknowns for the typical on-board computer to handle.

4.3.1 Illustrating Dynamic Behavior

Recalling the discussion on how batteries function and the issues that befall batteries, determination of the desired states must consider the non-linear and dynamic aspects of battery behavior. Particularly, the relationship between voltage and current has always been of interest. Characterizing battery behavior is done through non-invasive tests that demonstrate crucial aspects that ought to be considered for accurate battery models. As seen in Section 3.4.1.3, the definition of SOC is based on voltages. However, the cell voltages recommended by the manufacturer might not be the same as the operating voltages of the battery pack in the EV. After distinguishing the operating voltages, the static capacity of the cell is determined by measuring charge during a constant current discharge test at the rated capacity while starting from full capacity [52]. If the cell is new, the SEI may not have fully formed yet; hence, the rapid drop in capacity during the first few cycles of a cell. Therefore, the static capacity test may need to be repeated until the capacity stabilizes. It also bears consideration to repeat the discharge test at a low rate to establish an approximate maximum capacity value. In addition, recall that tests done at extremes of the cell temperature range and at high current are likely to damage the cell.

4.3.1.1 *Constant Current Charge and Discharge*

Many battery manufacturers demonstrate cell capabilities with constant current discharge tests at room temperature, showing the decrease in voltage as the charge output increases like shown in

Figure 55. Sometimes a similar plot is included highlighting how temperature affects the charge output for the same rate of discharge. Here, the LFMP cell used in Figure 55 is the same manufacturer and type as those used in the GEM. From the modeling and management perspective, it is important to notice a few key features of the discharge profile. Keep in mind that the voltage profile in Figure 55 is working voltage measured at the terminals, not the open circuit voltage (OCV). OCV is always higher than the working voltage while discharge and lower when charging. At both the beginning and end of the discharge cycle, the voltage decreases considerably. Next, the nearly flat voltage during the majority of discharge is a desired attribute of batteries. Lastly, though the discharge at 3 C-rate seemingly delivers less capacity, the discharge is stopped at a cutoff voltage to prevent harm to the cell. If the cell had continued discharge past the 2.6 VDC threshold, it could have delivered the full capacity. Alternatively, if the cell had continued discharge at a lower C-rate, the terminal voltage would have increased. Thus, more capacity could then be discharged before reaching the cutoff voltage.

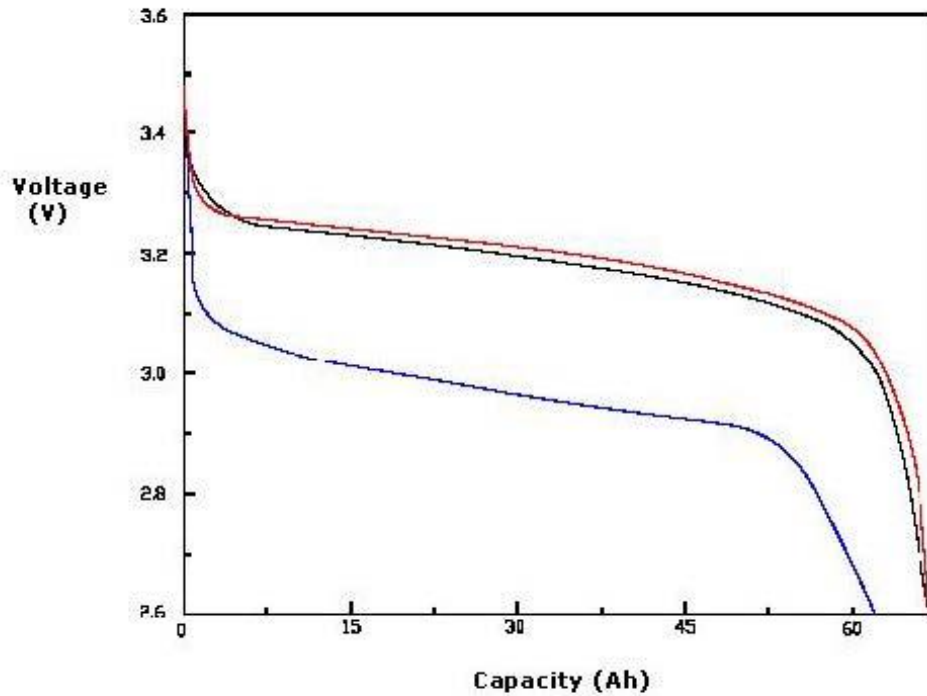


Figure 55: Discharge curve of the GBS 60 Ah LFMP cells provided by AA Portable Power Corp [31]. The red line, which remains at a higher voltage for the majority of the discharge event, is at 0.5 C-rate. The black line, right below red, is at 1 C-rate. Lastly, the blue line is at 3 C-rate.

While the cell in Figure 56 has a different positive electrode chemistry, it is also a lithium-ion battery. Terminal voltage of cells at a higher temperature are, in this instance, always greater than cells at lower temperatures. Similarly, the capacity output of cells at lower temperatures is lower than cells at higher temperatures. Ordinarily, terminal voltage decreases over discharge, but the terminal voltage of the cells at 0, -10, and -20 °C in Figure 56 all rise to at least some extent. This may be caused by energy lost in the form of heat as the discharge current flows through the internal resistance. The increase in temperature raises the rate of diffusion and the charge transfer rates at both electrodes [53, 54].

Discharge Characteristics (by temperature)

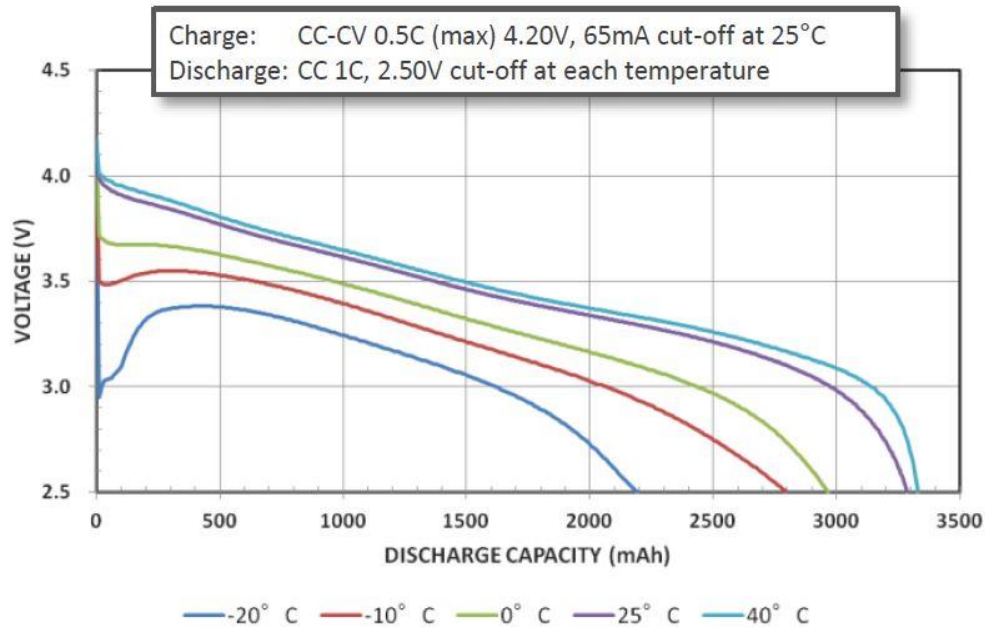


Figure 56: Discharge characteristics of a Panasonic 3200 mAh battery, model NCR18650B, at different temperatures [55]. The voltage decreases as the temperature decreases.

4.3.1.2 Hybrid Pulse Power Characterization

Hybrid Pulse Power Characterization (HPPC) is a testing procedure to determine the power capabilities of the cell by discharging—and charging—the cell at short bursts at different states of charge. The procedure, seen in Figure 57, begins with a full discharge of the cell at one-third C-rate, followed by a one hour rest for the cell to reach equilibrium voltage and temperature [52]. Then, the cell is fully recharged and given another rest period before starting the actual test. Each pulse lasts 30 seconds and is conducted at a minimum of one C-rate which is used consistently across all pulses. Once both charge and discharge pulses are completed, the cell is discharged at one-third C-rate until it reaches the next testing SOC that are in increments of ten. For example,

pulses are conducted at 80% SOC, after which the cell is discharged until it is at 70%, whereupon it will rest for an hour before undergoing the next set of pulses.

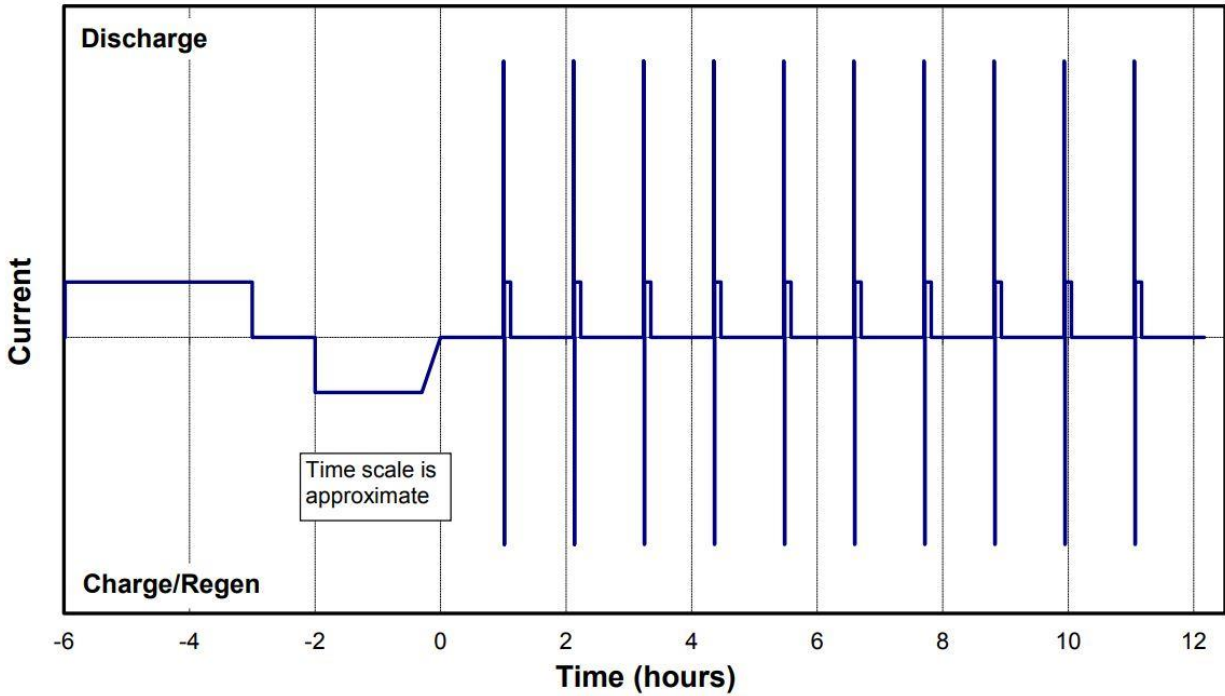


Figure 57: General procedure of an HPPC test [52].

The characterization in Figure 58 does not include regeneration, unlike Figure 57, but the voltage and SOC share the same plot [56]. HPPC tests are especially useful when demonstrating the transient voltage as the cell is discharge, and then as the voltage recovers after current is reduced. The sloped region where the voltage recovers is also called voltage relaxation. Given enough time, the battery will reach equilibrium near open circuit voltage (OCV).

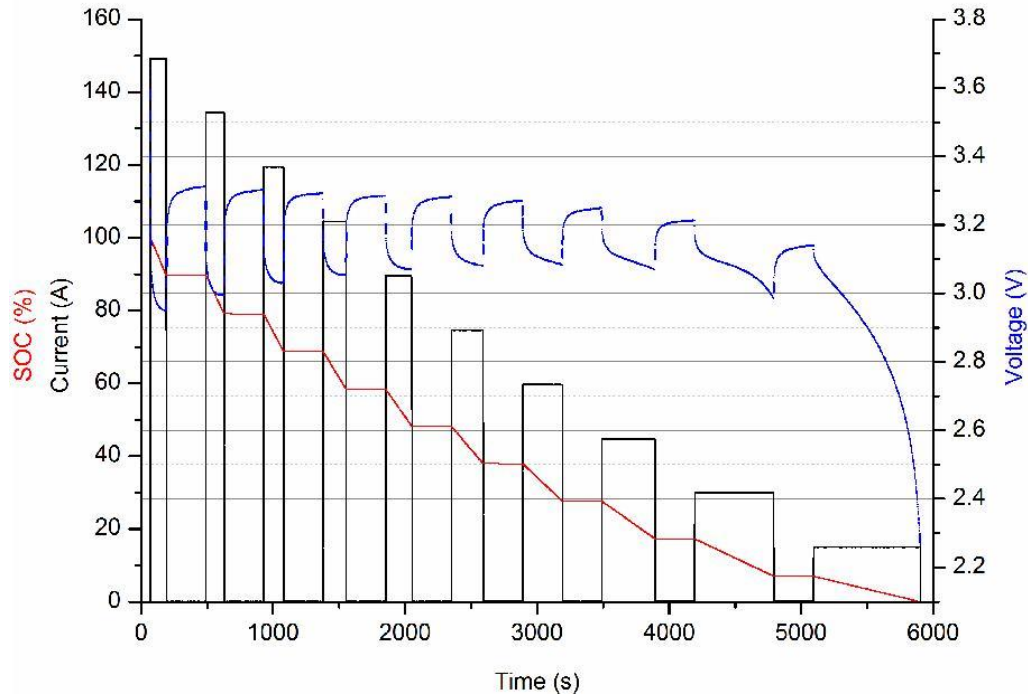


Figure 58: HPPC discharge current sharing a plot with the SOC and terminal voltage response [56]. Voltage response is fin-shaped where the curves represent time-dependent cell processes.

4.3.1.3 Hysteresis Effects

Voltage hysteresis can be seen through the difference in the voltages of a cell at each SOC when charging and discharging at the same rate. This voltage difference appears in OCV, like shown in Figure 59, where it is mostly independent of current rate [57]. By viewing hysteresis as a difference between OCV, it is expected that there is also an average OCV where the difference between OCV while charging and OCV while discharging is 0 VDC. Major hysteresis loops are formed when charging and discharging for the entire capacity while minor hysteresis loops are formed when transitioning between charging and discharging modes [58]. An example of creating minor hysteresis loops is as follows: OCV while charging will follow the hysteresis loop for charging until the cell begins to discharge, wherein the OCV will begin to approach the

average OCV for that SOC and continue until it reaches the discharge hysteresis OCV [59]. All minor hysteresis loops are located within the major hysteresis loop [57].

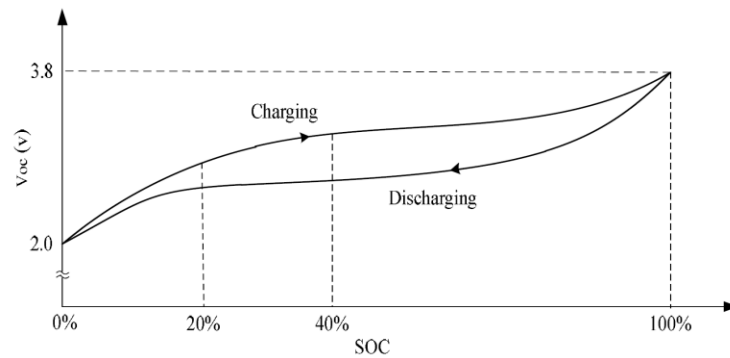


Figure 59: The difference in OCV while charging and discharging is from hysteresis effects [57]. Since this is a complete cycle, this is a major hysteresis loop.

OCV hysteresis results from the distortion of lattices in the electrode, increased mechanical stresses, and non-uniform phase distribution [57]. The rate of reaching OCV—and the level of hysteresis—after (dis)charge changes due to chemistry, temperature, DOD, and the rate of (dis)charge before voltage relaxation [59, 60]. Temperature is a major contributor to how quickly the cell approaches OCV since voltage relaxation is due to the SEI formation, double-layer capacitance, and solid-state diffusion [60, 61]. Furthermore, hysteresis is more pronounced at lower temperatures [51]. Given the major limitations of LFP batteries at low temperatures, discussed in Section 3.3.3.3, consideration of hysteresis is recommended for models calculating SOC with voltage. Since voltage hysteresis changes the expected voltage for a certain SOC, determining SOC using voltage will be incorrect unless compensating for hysteresis. Unfortunately, acquiring experimental data for hysteresis models can be a tedious and long-term effort.

4.3.1.4 Electrochemical Impedance Spectroscopy

Electrochemical Impedance Spectroscopy (EIS) is the determination of cell impedance by measuring the current and voltage response to various frequencies of low magnitude AC voltage. While this is not a modeling approach, the information gleaned from these tests can be used to characterize models. EIS measurements are often displayed in Nyquist plots, which can be generated at specific SOC or temperature. Nyquist plots show the relationship between real and imaginary components of the impedance, as seen in Figure 59. In the same figure, there are three points of particular interest: the abscissa when the impedance is purely ohmic, the vertex within the “Charge Transfer” region, and the vertex occurring after the inflection point. Since the vertical axis of Figure 60 is reversed, the positive ordinate values represent capacitance while negative ordinate values are inductance.

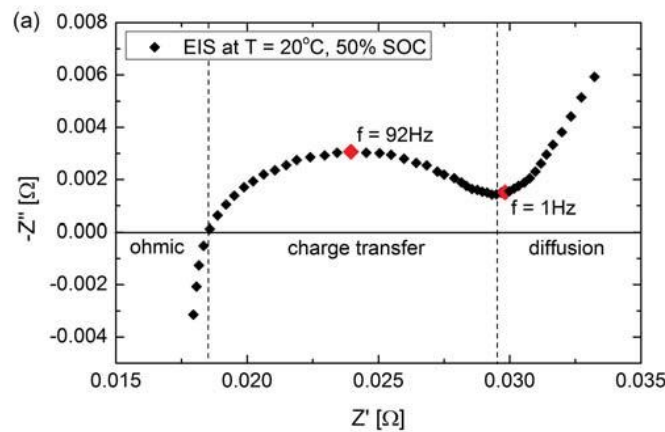


Figure 60: EIS Nyquist plot of a LFP cell at 20 °C and 50% SOC [62].

Using EIS, time dependent cell behaviors can be studied—so long as they occur at different rates. Performing measurements across an array of temperatures and SOC is a time-intensive process. As seen in Figure 61, the magnitude of the impedance is highly dependent on

temperature, but SOC has only a minor impact [63]. There is some variation across SOC in the low frequency linear region that indicates that the phase angle at low frequency decreases as SOC decreases.

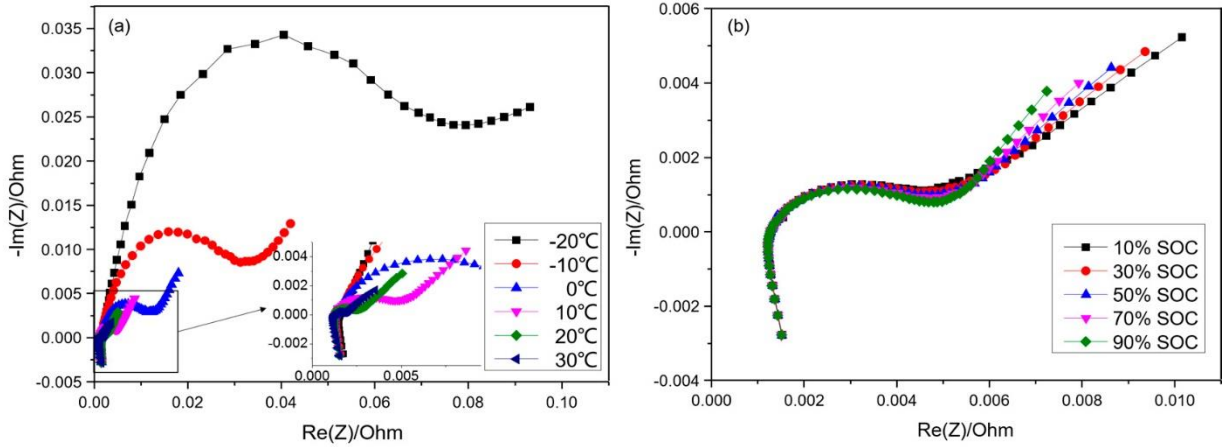


Figure 61: Left—Nyquist plot of EIS measurements of a cell at 50% SOC and across a range of temperatures [63]. Right—Nyquist plot of EIS measurements of a cell at 10 °C and at various SOC.

Moreover, considering the noticeable effect cycling has on impedance, like that shown in Figure 62, determination of SOC by EIS data and models will eventually become inaccurate [64].

However, regularly conducting EIS measurements and recalibration of the battery model is feasible. Although, model recalibration is tedious and time-consuming because it would likely require taking the vehicle in for maintenance.

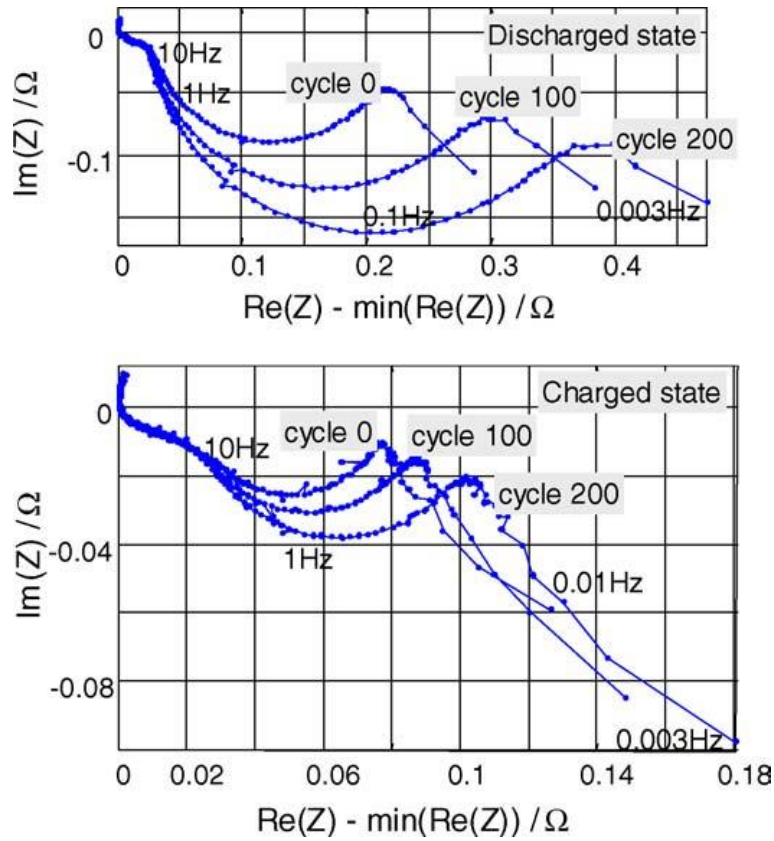


Figure 62: EIS plots of a discharged cell (top) and charged cell (bottom) at different cycles [64].

4.4 Battery Modeling

4.4.1 Coulomb Counting

Coulomb, or Ampere hour (Ah), counting is a relatively simple way of estimating SOC while the battery is still in use. Similar to discharge testing, Coulomb counting measures the ingress and egress of charge over time. This method is popular in battery management practices since it is straightforward and respectively easy to calculate. However, there are important errors and limitations inherent in this method that should be considered. Specifically, the capacity of a cell is always just an estimation, at least according to practical methods and without

decommissioning the cell. All cells age at different rates, losing active materials in side reactions and deterioration of components. Moreover, there is a loss in overall available charge through aging, even when the cell is not in use. While testing can provide a relatively good approximation, it is important to keep in mind that the available charge is depleted slowly through self-discharge. In addition, available charge in the battery depends on the rate of discharge and temperature. This brings up another issue, estimating the SOC if no previous data on the cell exists. In this case, SOC is then determined as a function of measurable factors. Finally, even when the battery is working appropriately, recorded charge and discharge efficiencies might be inaccurate, or even the current measurements themselves. As a result, coulomb counting requires accurate current measurements because the measurement error will accumulate until the system is recalibrated [51]. Furthermore, the initial SOC estimate must be accurate; otherwise, all ensuing states may be incorrect. The maximum capacity must be updated when recalibrating the system since it does not remain constant. Overall, because of accumulated errors in current measurements, high power systems can quickly reach significant errors [65]. Thus, co-estimation and confirmation between two methods is preferred.

A mathematical expression of coulomb counting to determine SOC can be calculated as follows [32, 51]:

$\text{SOC}(t_2) = \text{SOC}(t_1) - \frac{\eta_i}{Q_n} \cdot \int_{t_1}^{t_2} I(\tau) d\tau$	(18)
---	------

Here, the SOC at a moment in time is equal to the difference between the initial state of charge and the proportion of the total charge that has entered or exited the battery. Current (I) is measured in amperes [A] and follows the notation of negative when charging and positive when

discharging. Within the context of Eqn. (18), it is assumed that the overall charge capacity of the battery (Q_n) remains constant with the coulombic efficiency (η_i) employed as the ratio of charge output to charge input. Not all energy that goes into charging the battery will be available, as some will be lost as heat due to the internal resistance of the cell. In general, the cell coulombic efficiency decreases over time with the growth of the SEI layer and passivation of components. However, all charge that enters the cell will remain available, except for leakage current that is quite small. The energy lost is due to hysteresis and is apparent through the difference between discharge voltage and charge voltage. Accounting for hysteresis will be discussed in Section 4.5.1.

4.4.2 Data-Based Empirical Methods

Empirical battery models consist of equations derived from these experimental data through which current battery measurements can be related. This method suffers inaccuracies from data limitations, most as a result of highly dynamic battery behavior [66]. In general, accuracy of this method is improved by characterizing the battery across a multitude of situations. Specifically, voltage measurements—or impedance—are measured periodically through full discharge and charge for various current rates and temperatures. Furthermore, even if the equation fits the experimental data well, the equation will be inaccurate for conditions outside those of the experiment [67]. Differences in temperature, rate of (dis)charge, SOH, or even between cells of the same type and chemistry may lead to errors. Other mathematical models, while still parameterized using experimental data, are functions developed through simplifying physical and electrochemical behaviors.

4.4.3 Peukert's Law

Peukert's equation—or Peukert's Law—is an empirical relationship that was originally applied to lead-acid batteries to demonstrate the loss of capacity associated with an increased rate of discharge. The efficiency of discharge in lead-acid batteries decreases as current increases, resulting in the noticeable loss in available capacity. The available capacity in lithium-ion batteries does not experience the same degree of loss as lead-acid batteries, but Peukert's equation can still apply to lithium-ion batteries with reasonable results. An Enhanced Peukert model has been introduced that accounts for temperature and the absolute capacity of the cell, while reconciling units [68, 69]. The original Peukert expression is as follows:

$C_p = I^k \cdot t$	(19)
---------------------	------

The cell capacity at a specific discharge rate (C_p) is measured in [Ah]. Constant current (I), in [A], is raised to an exponent known as Peukert's constant (k), and multiplied by the time (t) it takes in hours to discharge the battery. Ideally, a cell will have a k value equal to one, meaning that regardless of discharge rate, the capacity remains the same. In general, lithium-ion cells have Peukert constants near unity, approximately 1.05 [25]. The enhanced Peukert capacity model calculates the change in capacity over the duration of a time step, (ΔC_r) in [Ah] [7]. For the duration of the time step (Δt) it is assumed that current and temperature (T) remain constant. Both current and temperature in the enhanced Peukert capacity model are the numerator and denominator respectively to reference values to remove units. The reference values must remain constant across models for consistency proper comparisons to be drawn. The contribution that current rate has on capacity is affected exponentially by a battery-specific constant (α).

Similarly, the temperature component is set to the battery-specific exponent (β). The final battery-specific variable of this expression is the proportionality constant (γ), which is measured in [A] to balance units and scales the product such that a cell unaffected by current rate or temperature would have γ equal to the rated capacity:

$\Delta C_r = \gamma \cdot \left(\frac{I}{I_{ref}} \right)^\alpha \cdot \left(\frac{T_{ref}}{T} \right)^\beta \cdot \Delta t$	(20)
---	------

The enhanced Peukert capacity model utilizes the notion that each cell has an absolute capacity from which charge is removed during discharge. A high rate of discharge may reduce the voltage of a cell to 0% SOC, but capacity remains within the cell and is accessible at a lower discharge rate. This model is heuristic, established by trends and unrelated to the electrochemical processes transpiring within the cell but still relatively accurate. However, it is unable to estimate the voltage of the cell and, therefore, relies on experimental voltage maps that can deviate from actual operation.

4.4.4 OCV-SOC Relationships

This empirical method develops open circuit voltage (OCV)-SOC relationships: equations that estimate desired states using experimentally derived parameters and battery measurements, but all have some basis in battery behavior. These, and equivalent circuit models (ECMs), are lumped-parameter models often used in EVs for real-time application because of their ease of use. Regardless of whether solving for terminal voltage or SOC, OCV is either constant or a function of an input. Furthermore, OCV is not usually an output but rather characterizes the cell. As mentioned regarding measuring hysteresis (Section 4.3.1.3), OCV is measurable to some extent, though it is not practical for use when the vehicle is active. Depending on the cell

chemistry, temperature, the DOD, and the rate of (dis)charge before resting, it can take anywhere from an hour to a couple days for the voltage to stabilize. Even then, hysteresis effects may linger.

Each of the following OCV-SOC relationships share a similar perspective of cell voltage, which is analogous to polarizations [51]. In specific, models differ by the terms used to express overpotential—discussed in Section 3.3.2—in relation to SOC. Previously, these models were especially useful for lead-acid batteries because the OCV-SOC relationship was primarily linear [70]. Unfortunately, OCV-SOC relationships in lithium-ion batteries are not linear and the relationship changes with age. Furthermore, the degree to which it changes is not yet fully understood [49, 71]. However, despite the complicated nature of OCV, the basic models are simple and still can be used effectively.

4.4.4.1 *Shepherd Model*

Starting at the beginning, the Shepherd battery model was introduced in 1965 to describe current density distribution so that cell design could be optimized [72]:

$V_k = E_0 - R_0 \cdot I_k - \frac{K_1}{Z_k}$	(21)
---	------

This particular model employs a cell potential term (E_0) from which there are voltage losses [51]. Depending on model requirements, cell potential can remain constant, but sometimes E_0 is a function of temperature. Since Eqn. (21) is discretized, the step number is (k). The voltage is decreased proportional to the current (I) as it passes through the internal resistance (R_0). Both the cell potential and internal resistance are functions of whichever effects the model is

considering. This internal resistance depends on the direction of the current [73], and can also change based on SOH, SOC, and temperature. The SOC (Z) is the quotient of the available charge to the overall charge and a constant of proportionality, known as the coefficient of polarization (K_1), is utilized [72]. This form uses SOC as a state to determine the terminal voltage (V) and the open circuit voltage (V_{OC}) is a function of SOC, which is a part of the Shepherd model [66]:

$V_{OC} = E_0 - \frac{K_1}{Z_k}$	(22)
----------------------------------	------

Here, SOC is determined using coulomb counting, but can also be determined iteratively if terminal voltage is provided.

4.4.4.2 Unnewehr-Nasar Universal Model

The Unnewehr-Nasar model has the same open circuit potential term and voltage drop due to internal resistance as the Shepherd model [51].

$V_k = E_0 - R_0 \cdot I_k - K_2 \cdot Z_k$	(23)
---	------

The only difference from the Shepherd model is that the constant of proportionality (K_2), is multiplied by the state of charge in this model; hence, it is contrary to the corresponding parameter in Eqn. (21) [20]. Similarly, OCV (V_{OC}) is a function of SOC.

$V_{OC} = E_0 - K_2 \cdot Z_k$	(24)
--------------------------------	------

4.4.4.3 Nernst Model

The Nernst equation—one representation shown as Eqn. (15)—calculates the cell potential of the complete electrochemical reaction. The Nernst model is an adaptation to resemble the Nernst equation by including logarithmic terms to adjust for cell polarizations related to SOC [74]. The change in this voltage is proportional to the logarithm of the fractional state of charge [51, 75]:

$V_k = E_0 - R_0 \cdot I_k + K_3 \cdot \ln(Z_k) + K_4 \cdot \ln(1 - Z_k)$	(25)
---	------

The new terms for the Nernst model are the constants of proportionality K_3 and K_4 . Following the same trend as the previous two models, the OCV equation simply includes these new terms:

$V_{OC} = E_0 + K_3 \cdot \ln(Z_k) + K_4 \cdot \ln(1 - Z_k)$	(26)
--	------

4.4.4.4 Combined Model

The combined model approximates the voltage by including the state of charge terms of the Nernst, Unnewehr-Nasar, and Shepherd models [51, 66, 73]. Each state of charge term can be considered as compensation for overpotentials in the cell with the E_0 and K terms as constants.

$V_k = E_0 - R_0 \cdot I_k - \frac{K_1}{Z_k} - K_2 \cdot Z_k + K_3 \cdot \ln(Z_k) + K_4 \cdot \ln(1 - Z_k)$	(27)
---	------

Thus, the OCV term is a more complicated function of SOC:

$V_{OC} = E_0 - \frac{K_1}{Z_k} - K_2 \cdot Z_k + K_3 \cdot \ln(Z_k) + K_4 \cdot \ln(1 - Z_k)$	(28)
--	------

4.4.5 Equivalent Circuit Models (ECMs)

Mathematical battery models describe battery behavior using one or multiple sets of equations. Simplified electrochemical models are a subsection of mathematical models that describe the behavior of a cell in terms of voltage, current, and state of charge. Moreover, additional aspects of the battery are usually taken into consideration, such as the electrical resistance within the cell. At a glance, a battery appears to be a simple electrical device. Though, as discussed in 3.3.2, cell behavior is best described in terms of physics and chemistry. While it is important to understand the fundamental processes, it is too difficult for many systems, especially mobile applications, to track and predict the system using chemistry and thermodynamics. Reducing the number of parameters by simplifying electrochemical reactions into their electrical circuit analogs consequently decreases the computational load and time. Here, phenomenological approaches to battery modeling can be faster and sufficiently accurate for mobile applications, but they are not capable of attaining the same level of accuracy as electrochemical models. As a result, ECMs have been developed to simplify battery modeling. For EV applications, the battery model is expected to return the SOC of the battery pack, usually based on the history of the load placed on the battery and sometimes the external voltage supplied. In addition, numerous battery models are arranged to output terminal voltage

Many ECMs include an OCV component that is the voltage measured at no load, which is estimated by measuring the voltage when the current is nearly zero. This OCV value varies depending on the goal and complexity of the model. Typically, this component relates voltage to SOC but can also include temperature and SOH effects. Since temperature does have an impact

on OCV-SOC relationship, the model should compensate for its influence [74]. Generally, ECMs involving time-dependent terms are more accurate than OCV-SOC relationships. Here, an ECM provides an electrical representation of the electrochemical kinetics (e.g., resistance and capacitance) within the cell. Specifically, the internal reactions, materials, temperature, health, etc. all impact the battery's electrical performance. These influences can be described in terms of electrical components that behave electrically similar. Essentially, the developed circuit is an analogy of the battery including its internal components and functionality. In addition, the equivalent circuit analogy is supported by impedance measurements through EIS.

4.4.5.1 Ideal Battery ECM

The simplest ECM is an ideal battery that has no internal impedance, like shown in Figure 63. Terminal voltage (V) is the same as OCV (V_{OC}). OCV can still be a function of external factors, such as current (I), time (t), temperature (T), SOC (Z), SOH, etc.

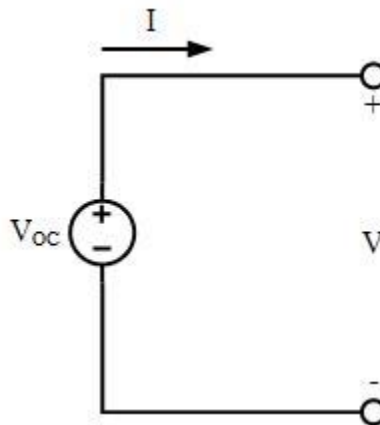


Figure 63: Ideal Battery ECM comprised of only a voltage source.

The ideal battery ECM equation is as follows:

$V = V_{OC} = f(I, t, T, Z, SOH, \dots)$	(29)
--	------

The function is assumed to be continuous; however, it can be discretized like the OCV-SOC relationships in Section 4.4.4. The ideal battery is not actuality; i.e., cells do have internal resistance and terminal voltage has a more complicated relationship with OCV.

4.4.5.2 Internal Resistance ECM

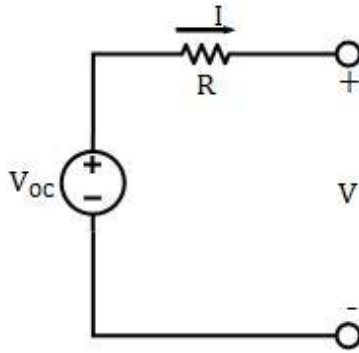


Figure 64: Internal resistance (R_{int}) ECM.

The internal resistance model (R_{int}), shown in Figure 64, determines terminal voltage (V) with the following mathematical equation:

$V = V_{OC} - I \cdot R_0$	(30)
----------------------------	------

where the open circuit voltage (V_{OC}) is reduced by the voltage drop caused by current (I) passing through the internal resistance (R_0) during discharge. While charging, the current is conventionally negative; hence, the terminal voltage is equal to the sum of OCV and the product of current and internal resistance. Of importance, the resistance values during charging and discharging may be different to compensate for hysteresis. Resistance and OCV can be functions

of temperature, SOC, current, SOH—same as with the ideal battery ECM. In terms of overpotentials, only the ohmic polarization is considered in the R_{int} ECM.

The terminal voltage in the R_{int} model changes linearly with current that is ideal but not realistic since the electrochemical processes within the cell are not instantaneous. Thus, ECMs ought to account for dynamic voltages. The R_{int} ECM is functionally the same as the OCV-SOC relationships mentioned in Section 4.4.4 and effectively Eqn. (21). This relationship would be established experimentally and applied in either a lookup table or an empirical function. As seen in EIS Nyquist plots in Figure 61, internal resistance does not change significantly with SOC, but slowly increases with cycle life. Furthermore, growth of the SEI layer is associated with increased resistance; hence, a decreasing SOH.

The non-linearity of the voltage response to current is apparent in Figure 65 and implicit from the EIS results in Figure 60. Immediately upon discharging, the voltage decreases proportional to the current rate due to internal resistance. Once discharge stops, the voltage immediately recovers the same voltage dropped. This is the resistive component of the cell enabling ohmic polarization.

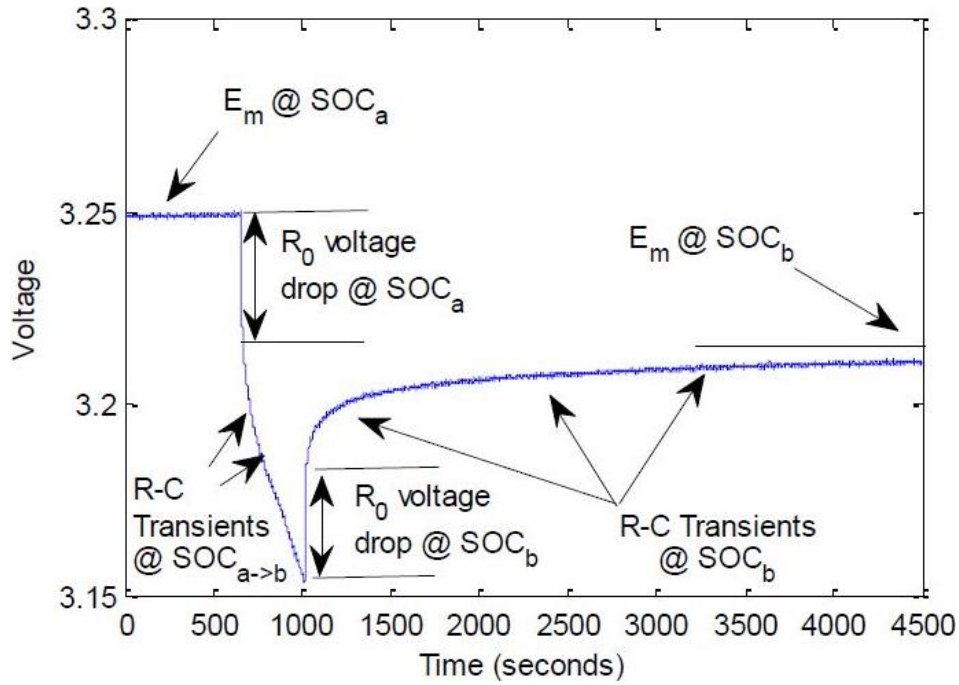


Figure 65: LFP cell voltage after single pulse discharge [76].

The continued voltage drop during the discharge event subsequently followed by voltage recovery once current stops occurs as functions of time and current rate, as seen in Figure 65.

The non-linear region—occurring in the transition from the resistive voltage drop to the mostly linear section of the RC transients—is attributed to charge transfer [77]. The voltage drop due to ohmic and activation polarizations can also be seen in Figure 66. Thus, the primary contributor to the remaining voltage drop is the diffusion aspect of the concentration polarization. In terms of electrical impedance, since the current is leading the voltage, the battery has a somewhat capacitive nature. Hence, the voltage response is seen to have both resistive and capacitive components of the overall impedance.

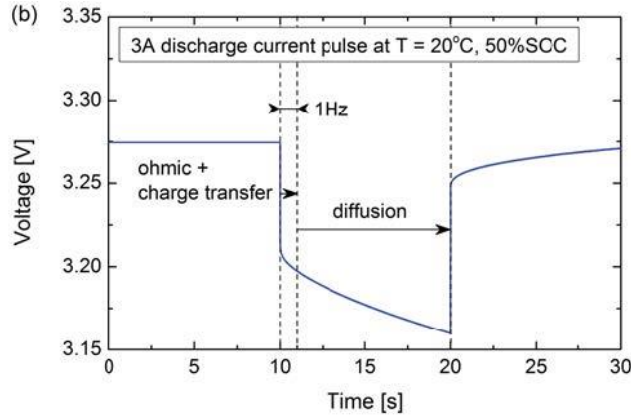


Figure 66: Voltage response to a discharge pulse. The LFP cell measured here is the same as in Figure 60. Typically, behavior occurring at frequencies lower than one hertz are mass transfer through diffusion [62].

Oftentimes, ECMs that use OCV to determine states employ ideal voltage sources within their circuit, while other ECMs may use one or multiple pseudocapacitors as their voltage source [15]. Here, pseudocapacitance refers to the storage of electricity in an electrochemical capacitor, which in batteries exists as the double-layer boundary at the surface of an electrode. Subsequently, delayed voltage responses are represented by the pseudocapacitance in ECMs (e.g., Saft-NREL resistance-capacitance (RC) model) while ideal voltage is instantaneous in the internal resistance (R_{int}) and Thévenin models (to be discussed) [78]. This use of pseudocapacitance represents mass transfer limitations and the double-layer effect. Furthermore, resistors in series with the terminals within the circuit generally represent ohmic losses within the battery, while resistors parallel to capacitors are the faradaic components of charge transfer losses. Hence, a resistor in parallel to a capacitor can be used to represent the activation or concentration polarizations. In addition, multiple resistor-capacitor pairs can be used to account for numerous time-variable battery functions [79].

4.4.5.3 Thévenin ECM

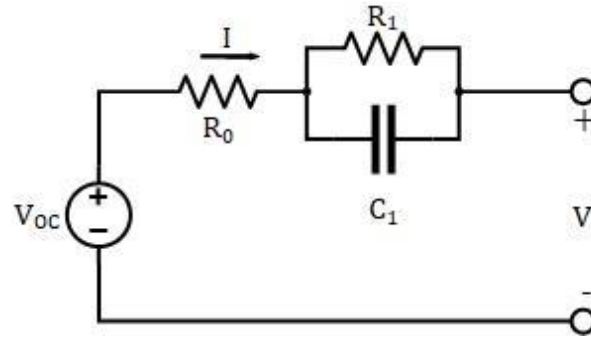


Figure 67: Thévenin ECM highlighting the inclusion of a capacitor into the model.

Therefore, the next complex ECM is the Thévenin circuit in Figure 67 where the terminal voltage is equal to the open circuit voltage reduced by the voltage drop over a resistor/capacitor pair while also including an internal resistance (R_0):

$V = V_{OC} - V_{C_1} - I \cdot R_0$	(31)
--------------------------------------	------

The purpose of the resistor/capacitor pair in parallel is to emulate dynamic attributes of battery behavior in the time domain. Particularly noticeable in the frequency domain, the resistive and capacitive components influence the overall impedance that changes with temperature, SOH, and to a lesser extent, SOC. Since the capacitor is in parallel to the resistor, the voltage drop across them are the same but the current may differ. Here, current through the capacitor is as follows:

$I_C = C \cdot \frac{dV_C}{dt}$	(32)
---------------------------------	------

where the current through the capacitor branch (I_C) is equal to the product of the capacitance (C) and the time (t) rate of change of the voltage drop across the capacitor (V_C). By rearranging

Eqn. (38) and using Ohm's Law, the time change in voltage (\dot{V}_{C_1}) of the RC pair is determined to be:

$\frac{dV_C}{dt} = \dot{V}_{C_1} = -\frac{V_{C_1}}{R_1 C_1} + \frac{I}{C_1}$	(33)
--	------

4.4.5.4 Randles ECM

While quite similar to the Thévenin ECM, the Randles ECM was developed based on the impedance of electrode reactions and primarily used in the frequency domain [80]. The generalized Randles ECM is shown in Figure 68.

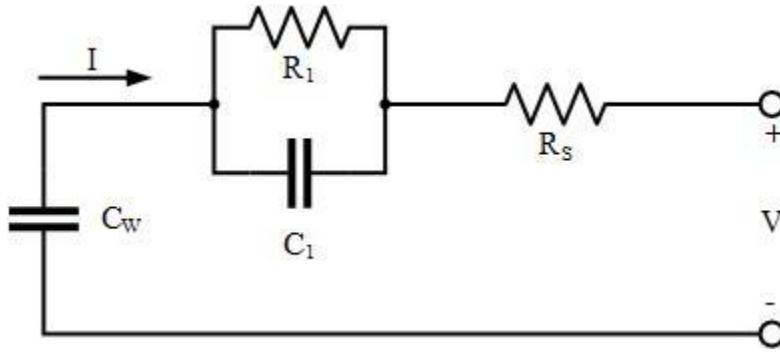


Figure 68: Generalized Randles' ECM with one RC pair [66, 79].

Now, instead of a voltage source, the bulk of the charge and voltage in the generalized Randles ECM originates in the Warburg capacitor (C_w), though other sources label it the bulk capacitor [66, 79]. Series resistance (R_0) of the generalized Randles ECM has the same electrical effect as the internal resistance term used in the R_{int} model, representing ohmic polarization from the conduction of charge carriers through the electrolyte, electrode, and current collectors [66, 79]. Since EIS studies the electrical response of the system, ECMs made in the frequency domain

give a clearer image of the underlying behavior. Originally, Randles ECM was relatively different.

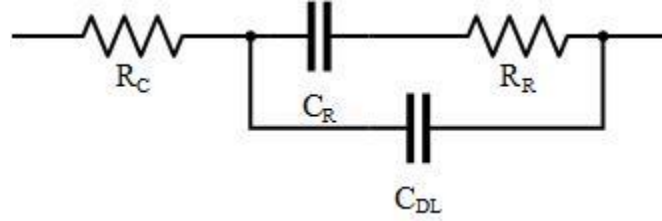


Figure 69: Randles equivalent circuit for electrode reactions [80].

Randles' equivalent circuit, shown in Figure 69, represents the kinetics of a rapid electrode reaction where diffusion and electrolyte resistance play a role in the rate of the reaction [80]. The series resistance (R_C) is from the electrolyte. Impedance of the reaction itself has capacitive (C_R) and resistive (R_R) components, which are parallel to the capacitive effect of the double-layer (C_{DL}) at the electrode surface. The resistive component of the reaction is from charge transfer (R_{CT}), and the electrical reactance of the reaction is more frequently modeled with Warburg impedance (Z_W). Further development of EIS characterization characterizes the double-layer capacitance as an imperfect capacitor because of the roughness of the electrode surface, choosing instead to model it with a constant phase element (CPE) as seen in Figure 70 [81, 82].

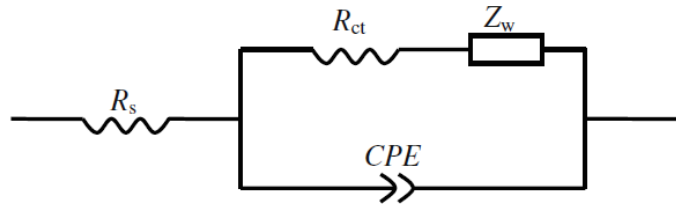


Figure 70: Example equivalent circuit for battery EIS data [82].

Warburg impedance appears in the low frequency region of the battery EIS response, which is the straight or nearly straight tail end seen in Figure 60. Otherwise, the circuit topology is the same as the Thévenin ECM. In addition, extra RC pairs may be included in the generalized Randles ECM, as well as in the Thévenin ECM.

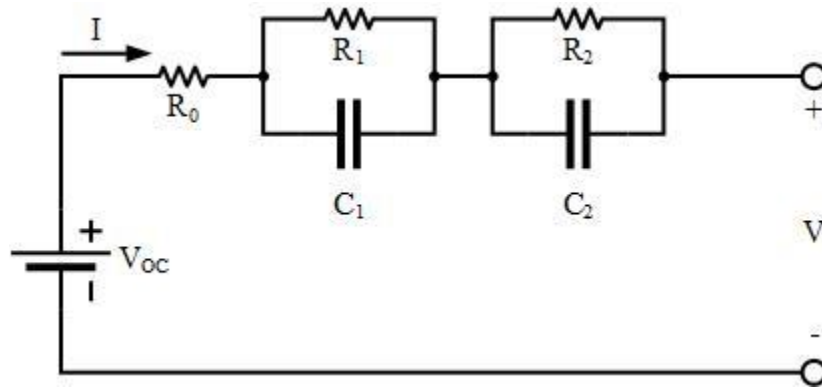


Figure 71: Dual Polarization ECM showing the inclusion of a second resistor/capacitor pair [50, 83].

Subsequently, the Dual Polarization (DP) model in Figure 71 extrapolates on the idea of the Thévenin model by including a second RC pair. Generally, inserting capacitors in ECM models adds time dependencies to compensate for transient behaviors. Hence, each resistor/capacitor pair have separate time constants; thus, representing different polarizations. For the DP model, often one pair is attributed to the diffusion polarization while the other represents the concentration polarization. Though, without directly measuring the reactions within the cell, it is unknown whether the model is truly representative of those behaviors.

Within the DP ECM, the rate of change of the voltage (\dot{V}_{C_2}) of the second RC pair is calculated as:

$\dot{V}_{C_2} = -\frac{V_{C_2}}{R_2 C_2} + \frac{I}{C_2}$	(34)
--	------

and is added to the first pair in Eqn. (33) resulting in the overall voltage of the battery. In addition, the terminal voltage in the DP ECM is characterized as:

$V = V_{OC} - V_{C_1} - V_{C_2} - I \cdot R_0$	(35)
--	------

It is important to note that the results of parameterization do not guarantee that the resistance and capacitance values match what are measured from the cell, only that the behavior of the circuit approximates battery behavior based on the measured values used to inform the circuit. Moreover, just as this model extrapolates on the Thévenin model, any number of resistor/capacitor pairs can be added for enhanced fidelity. However, when working with the discretized form of these equations, a larger number of pairs will lead to a greater sensitivity, which may then allow experimental data noise to throw off the model more easily (i.e., generation of non-physically dependent parameters) [79, 83]. Furthermore, self-discharge in ECMs like the generalized Randles and Thévenin versions is modeled by inserting a resistor in parallel with the bulk capacitor or OCV where it is not in series with RC pairs or other components [65, 76, 84]. The self-discharge resistor should have a relatively high resistance and be a function of temperature because self-discharge is slow in lithium-ion batteries while varying with temperature.

4.4.5.5 *Saft-NREL RC ECM*

Similar to the generalized Randles' ECM, the Saft-NREL RC model no longer has an OCV component of the circuit. Instead, the voltage supply aspect of the circuit is now controlled by

the capacitors rather than by a specified V_{OC} . As a result, the majority of the charge is stored in the bulk capacitor (C_b) while the charge stored in the surface capacitor (C_s) is more easily drained. Furthermore, the resistance in the bulk of the cell (R_b) is larger than the resistance to charge transfer at the surface of the cell [85]. Moreover, the internal resistance (R_0) represents the resistance in the charge collector and terminal connections. In addition, this model, shown in Figure 72, is relatively similar to the single-particle model. However, a slight difference between the single-particle model and the Saft-NREL RC ECM is that all current must go through the surface of the single particle before entering the bulk; whereas, current can enter the bulk and surface capacitors in this ECM.

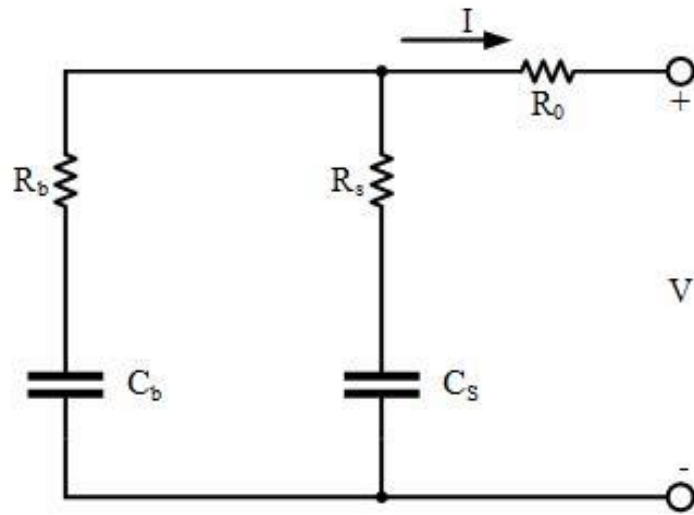


Figure 72: This resistance-capacitance (RC) ECM, developed by Saft and revised by NREL, uses capacitors to store charge in the cell [78, 83, 86].

The voltage across the terminals is still affected by the voltage drop across the resistance that is proportional to the current. As stated, the OCV is not determined in the Saft-NREL RC ECM; thus, it needs to be characterized separately. In addition, the voltage across the smaller capacitor is closer to the terminal voltage because it has a lower series resistance.

$V = \begin{bmatrix} \frac{R_s}{R_b + R_s} & \frac{R_b}{R_b + R_s} \end{bmatrix} \begin{bmatrix} V_b \\ V_s \end{bmatrix} + \left[-R_0 - \frac{R_b R_s}{R_b + R_s} \right] I$	(36)
--	------

The rate of change of the voltage across the capacitors depends on the present voltage at that point and the current, whether drawn from or pushed into the battery. Since the bulk capacitance and resistance of the circuit are larger, this impedes current flow and reduces the rate of change of the bulk voltage.

$\begin{bmatrix} \dot{V}_b \\ \dot{V}_s \end{bmatrix} = \begin{bmatrix} \frac{-1}{C_b(R_b + R_s)} & \frac{1}{C_b(R_b + R_s)} \\ \frac{1}{C_s(R_b + R_s)} & \frac{-1}{C_s(R_b + R_s)} \end{bmatrix} \begin{bmatrix} V_b \\ V_s \end{bmatrix} + \begin{bmatrix} \frac{-R_s}{C_b(R_b + R_s)} \\ \frac{-R_b}{C_s(R_b + R_s)} \end{bmatrix} I$	(37)
---	------

Overall, the accuracy of the developed circuits can be improved through a number of adjustments. One such modification is temperature dependency for the discrete circuit components. For example, the open circuit voltage may change with the internal temperature of the cell. Another consideration is hysteresis, a phenomena where the voltage at a state of charge differs when the cell is being charged or discharged [66].

4.5 Continuing Mathematical Models

4.5.1 Voltage Hysteresis

4.5.1.1 Zero-State OCV Hysteresis

The zero-state hysteresis term when appended to the simple model is shown as [51]:

$V = V_{OC} - R_0 I - sM$	(38)
---------------------------	------

The final term is the product of s , which is the direction of the current at each step, and M , which is the level of hysteresis at that time step. The sign of s only changes if the current is great enough to cause hysteresis, else the value remains the same as the previous step. For the sake of simplicity, s is unity for discharging and negative unity for charging. Since the hysteresis term is not a state, it remains constant. Thus, the zero-state hysteresis does not compensate for the impacts of temperature and current rate on hysteresis.

4.5.1.2 One-State OCV Hysteresis

Improving upon the zero-state hysteresis model, the one-state hysteresis model sets the hysteresis voltage, h , to a function of both SOC and time. Hysteresis is positive while charging and negative while discharging. The maximum hysteresis as a function of SOC and the rate of change of SOC is denoted as M with the voltage calculated through:

$\frac{dh(SOC, t)}{dSOC} = \gamma * sgn\left(\frac{dSOC}{dt}\right) * M\left(SOC, \frac{dSOC}{dt}\right) - h(SOC, t)$	(39)
---	------

The new term, γ , is used to scale the rate of voltage decay in respect to a normal hysteresis value. Before the equation can be applied to a battery model, it needs to be rearranged to be a function of time, instead of SOC. By multiplying both sides by the time rate of change of SOC, and recalling that the time rate of change of SOC multiplied by the sign of the time rate of change of SOC is simply the absolute value of the time rate of change of SOC, the hysteresis function is as follows:

$\frac{dh}{dt} = \left[M\left(SOC, \frac{dSOC}{dt}\right) - h(t) \right] * \left \frac{\eta_i i(t) \gamma}{C_n} \right $	(40)
--	------

This OCV hysteresis calculated in Eqns. (38) and (40) were originally built to be used in the R_{int} ECM. However, it is still the case that determining SOC based on voltage is still a less reliable method for LFP cells due to the mostly flat region of the (dis)charge curve [65]. Moreover, in consideration of the errors accumulated through coulomb counting for determining SOC, another approach was introduced to find agreement between OCV-SOC relationships and coulomb counting. Additionally, this method utilizes a Kalman Filter (KF) to compensate for measurement and process noise.

4.5.2 Determination of Other States

4.5.2.1 SOH

The SOH attempts to relay how much the battery has aged or broken down, usually by comparing the current maximum capacity to the rated maximum capacity of a cell. There are many issues that arise as cells age and permanent modes of capacity loss include SEI formation at both the cathode and anode, gas formation, irreversible lithium plating, and delamination or reduced contact area. Cell performance is further reduced by cracking of the electrode, dissolution of positive electrode metals followed by accumulation of these metals on the separator, reduction of metals from the positive electrode at the negative electrode in SEI formation, delamination between electrode and current collector, reduced porosity, and reversible lithium deposition on the negative electrode. While all of these have negative impact on cell health, some may degrade cell health faster than others. Measuring internal resistance and impedance is correlated to worsening cell health, but the underlying cause may remain unknown. Treatment of the cell considering these cells changes depending on the issues being faced. Cell life is often measured in time and in cycles because some causes of damage keep degrading the

cell despite it no longer being cycled. Models used to determine SOH are nearly as diverse as those to determine SOC. One model fits an equation like the Arrhenius equation to aging data [32]. Many others simply determine the reduction of capacity as an empirical model determined by testing the aging of similar cells.

A simple and general method of defining SOH is the following equation:

$SOH(t) = \frac{C_t}{C_0} \cdot 100\%$	(41)
--	------

where C_t is the current full capacity of the cell and C_0 is the full capacity of the cell when it was new [87]. A trend line fit to the SOH data for a cell can be used to predict SOH moving forward but does not consider the actual factors of declining health. Abnormal use, where the cell was perhaps charged while too cold or has been cycled many more times than usual between measurements, will skew the trend.

4.5.3 Methods

The models are constructed to output terminal voltage and SOC based on prior conditions and the current being drawn from the battery. Here, SOC is determined using coulomb counting via Eqn. (18). Three different ECMs are used: R_{int} , Thévenin, and DP. These were chosen because their circuits have OCV components. Furthermore, OCV was determined using the combined OCV-SOC model as defined by Eqn. (28). Since OCV measurements were not taken, and this method of parameterization assumes that each variable remains constant, the OCV-SOC models ensure that the model OCV is not constant for all SOC (experimentally shown [51, 52]). Here, the combined OCV-SOC model has more parameters that can fit the OCV-SOC equation

ensuring better accuracy. Each of the models were calibrated for seven separate batteries. Since the R_{int} model is the simplest, it was parameterized using the least square method. However, both Thévenin and DP ECMs were parameterized by minimizing the coefficient of determination (R_{SQ}) using the MATLAB function *fmincon*. Determination of parameters through solving a linear set of equations is expressly used for models where the parameters are considered constant and are directly proportional. While battery model parameters are dynamic, changes in respect to SOC, temperature, SOH, and rate of current are assumed small and occur slowly. Similarly, parameters are considered constant by the error minimization method, though this method is applied to linear and non-linear models the same.

Data for the A123 ANR26650M1A LFP and Panasonic NCR18650B cells were extracted from their discharge characteristics graphs on their respective specification datasheets and then linearly extrapolated to a voltage value every 0.1% SOC. Discharge data for the LG ICR18650B4 NMC, LG ICR18650C2 LCO, Panasonic NCR18650A NCA, LG LMN18650-2000 LMN, and A123 APR18650M1-A LFP cells were recorded by O'Malley at every 0.1% SOC increment [69]. Each cell underwent multiple discharge cycles at different discharge rates. The A123 ANR26650M1-B LFP cell was the only cell not discharged at constant current, but still at constant temperature of 23 °C. Instead, this cell was discharged at constant power rates of 20 W, 60 W, 100 W, 140 W, and 180 W. All cells discharged based on C-rate were tested at an ambient temperature of 26 °C and current is presumably based on the typical capacity expected of the cell. The Panasonic NCR18650B cell was discharged at 0.2, 0.5, 1, and 2 C-rates. Model ICR18650C2, produced by LG Electronics, was tested thrice at both 0.5 and 1 C-rates. NCR18650A produced by Panasonic was tested thrice at 0.5 C-rate, twice at 1 and 1.25 C-rate,

and finally once at 0.9 C-rate. The NMC cell model ICR18650B4 was discharged thrice at each 0.5, 1, and 1.25 C-rates. Cell model LMN18650-2000 was tested twice at each 0.5, 0.75, and 1 C-rates. Finally, the A123 cell model APR18650M1-A was tested thrice at each 0.5, 1, and 1.25 C-rates. Cell model and key characteristics are provided in Table 8 where the model names listed are shortened to fit data tables better.

Table 8: Cell models and corresponding characteristics [69].

Model	Shortened Name	Cell Chemistry	Nominal Capacity [Ah]	Nominal Voltage [VDC]
A123 ANR26650M1B	ANR M1B	LFP	2.5	3.3
Panasonic NCR18650B	NCR B	NCA	3.2	3.6
LG ICR18650B4	ICR B4	NMC	2.6	3.6
LG ICR18650C2	ICR C2	LCO	2.8	3.7
Panasonic NCR18650A	NCR A	NCA	3.1	3.6
LG LMN18650- 2000	LMN 2000	LMN	2.0	3.6
A123 APR18650M1A	APR M1A	LFP	1.1	3.3

4.5.4 Linear Least Squares Regression of R_{int} with Combined OCV-SOC Relationship

Since O'Malley recorded the battery discharge terminal voltage (V) at increments of 0.1% SOC (Z), there are 1001 data points (k) such that $V = [v_1 \ \dots \ v_k]^T$ and $Z = [z_1 \ \dots \ z_k]^T$, where $z_1 \approx 1$ [69]. Here, the discharge current (I) remains constant for each test so $I = [i_1 \ \dots \ i_k]^T$ and $i_1 = i_2 = \dots i_k$. Each test is parameterized separately, allowing comparison of parameters of the same battery across each discharge test, and parameterized as a concatenated column matrix.

The matrix of linear equations (G) multiplied by the column vector of desired unknowns (X) results in the column vector of terminal voltages.

$$\begin{bmatrix} v_1 \\ \vdots \\ v_k \end{bmatrix} = \begin{bmatrix} 1 & \frac{1}{z_1} & z_1 & \ln(z_1) & \ln(1-z_1) & i_1 \\ \vdots & \vdots & \vdots & \vdots & \vdots & \vdots \\ 1 & \frac{1}{z_k} & z_k & \ln(z_k) & \ln(1-z_k) & i_k \end{bmatrix} \begin{bmatrix} K_0 \\ K_1 \\ K_2 \\ K_3 \\ K_4 \\ R_0 \end{bmatrix} \quad (42)$$

The unknowns are solved for:

$$X = (G^T G)^{-1} G^T V \quad (43)$$

Relative accuracy of the resulting voltage (V_{res}) is determined for each cycle using the coefficient of determination (R_{SQ}). The total R_{SQ} for the battery model is the square root of the sum of each cycle's squared R_{SQ} .

$$R_{SQ} = \sqrt{\sum_{n=1}^k (V_n - V_{res,n})^2} \quad (44)$$

4.5.5 Iterative Parameterization Using MATLAB function *fmincon*

Each of the ECMs were then parameterized through an iterative optimization process where the goal was to minimize the coefficient of determination. Parameters are initialized as random integers that are then scaled to a logical order of magnitude. For the first run through for a battery, the order of magnitude was set as zero for all parameters besides K_0 and η_i . Since K_0 should be within the voltage range of the cell, based on the premise that it is an ideal voltage unaffected by SOC, its order of magnitude is assumed zero. Assuming that the coulombic

efficiency of the cells is above 90%, η_i has an order of magnitude of negative one and is allowed to range between nine and ten [15, 37]. Based on the randomized starting parameters, the program will work towards a solution with the lowest coefficient of determination that is within the bounds. Results were exported from MATLAB to Microsoft Office Excel. Once the prescribed tolerance was attained, the program would display the final values, subsequently the magnitude of the initial parameters would be changed, or the program would automatically choose another set of random values and rerun the process. Using the parameters that the program returns, the order of magnitude of the initial parameters are changed but the boundary remains the same until consecutive repetitions have approximately the same solution. Then, the bounds and termination tolerances are narrowed to find a better solution.

4.5.6 Modeling Results

When the linear least squares regression (LLSR) method was applied to the entire set of data, the results were significantly better than if any single discharge data set were used to parameterize the model. The parameters for the R_{int} and combined models for each battery were concatenated before solving, and are shown in Table 9. Pleasantly, parameterizing the model with all runs simultaneously removed scaling issues while inverting the matrix, a step in equation (43).

Table 9: Parameters for R_{int} and combined models solved through linear least squares regression.

	ANR M1B	NCR B	ICR B4	ICR C2	NCR A	LMN 2000	APR M1A
K_0	3.467E+00	3.440E+00	3.336E+00	3.412E+00	3.168E+00	3.361E+00	3.532E+00
K_1	-6.872E-05	-4.513E-05	1.280E-05	2.572E-06	-1.870E-05	8.921E-06	-3.799E-05
K_2	4.083E-01	-5.524E-01	-5.490E-01	-4.599E-01	-6.499E-01	-4.673E-01	2.832E-01
K_3	1.831E-01	1.285E-01	5.672E-04	6.845E-03	4.913E-02	3.307E-04	1.696E-01
K_4	-5.403E-02	-3.974E-02	-5.504E-02	-3.832E-02	3.998E-03	-5.410E-02	-1.862E-02
R_0	8.927E-03	7.058E-02	1.994E-01	1.581E-01	1.482E-01	1.907E-01	3.543E-01
R_{SQ}	4.7407	2.1167	3.2391	3.0047	4.2960	2.0121	1.5022

Unexpectedly, the R_{SQ} for the LFP cells are both the largest and smallest for this parameterization approach. The model results are more evident in plots; the best results for the LLSR method are shown in Figure 73. The regions of highest error are at the beginning and end of discharge.

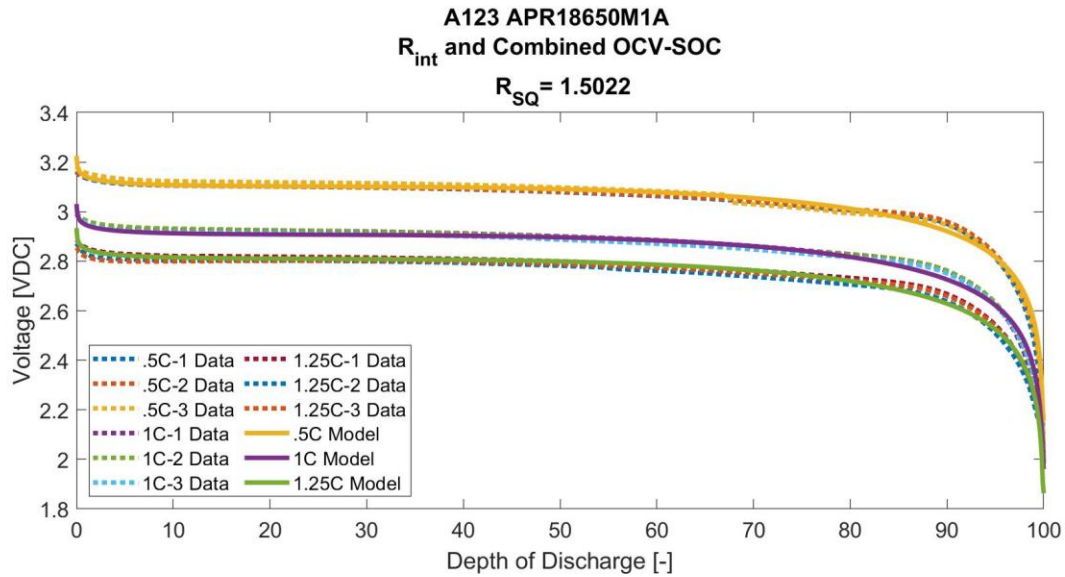


Figure 73: Plot of battery data and model results for the A123 APR18650M1A cell when parameterized for the R_{int} and Combined OCV-SOC models using LLSR.

As seen in Table 10, the APR M1A LFP cell again has the lowest error for the same model but parameterized in the iterative approach. Parameterizing the R_{int} model with the iterative approach produced slightly different results than LLSR. Outcomes also differ because coulombic efficiency was incorporated in the iterative method but not LLSR method. Originally, the iterative approach produced only positive parameter values because the upper and lower bounds were both positive. Since there are several terms in the combined OCV-SOC expression, the coefficients are adjusted to compensate for positive terms that would otherwise be negative. Thus, the error when using only positive parameters can also attain suitable accuracy. However, this suggests that multiple solutions exist for the same level of accuracy.

Table 10: Parameters for the R_{int} and combined models solved with MATLAB function `fmincon`.

	ANR M1B	NCR B	ICR B4	ICR C2	NCR A	LMN 2000	APR M1A
K_0	3.48E+00	3.42E+00	3.31E+00	3.40E+00	3.17E+00	3.34E+00	3.53E+00
K_1	-1.62E-04	1.07E-06	1.48E-04	5.23E-05	-7.75E-05	1.11E-04	-7.16E-05
K_2	4.19E-01	-5.87E-01	-5.86E-01	-4.77E-01	-6.42E-01	-4.99E-01	2.85E-01
K_3	1.87E-01	1.19E-01	-9.97E-03	2.46E-03	5.19E-02	-8.08E-03	1.71E-01
K_4	-5.47E-02	-3.65E-02	-5.15E-02	-3.66E-02	3.41E-03	-5.09E-02	-1.86E-02
R_0	8.93E-03	7.06E-02	1.99E-01	1.58E-01	1.48E-01	1.91E-01	3.54E-01
η_i	9.49E-01	9.50E-01	9.50E-01	9.50E-01	9.55E-01	9.50E-01	9.50E-01
R_{SQ}	4.71	2.17	3.20	3.00	4.29	2.00	1.50

The results in Table 10 reflect positive and negative coefficients; here, only K_1 , K_2 , K_3 , and K_4 were permitted to be negative since the other terms are assumed positive per the battery attribute they represent. For example, the internal resistance coefficient is positive since the R_{int} equation subtracts the term from the terminal voltage, which is the case in actuality. While a cell does not contain an ideal resistor, part of the cell voltage response is proportional to current as if there was an ideal resistor because the materials inside the cell have an equivalent electrical resistance.

Coefficients shown in Table 11 are for the Thévenin and combined OCV-SOC models, which were determined in the same manner as for the R_{int} model.

Table 11: Cell parameters and coefficient of determination for the Thévenin and combined OCV-SOC.

	ANR M1B	NCR B	ICR B4	ICR C2	NCR A	LMN 2000	APR M1A
K_0	3.26E+00	3.47E+00	3.65E+00	3.55E+00	3.22E+00	3.70E+00	3.08E+00
K_1	-1.13E-04	-1.77E-04	9.28E-05	-5.27E-05	-1.64E-04	-2.77E-06	-5.97E-05
K_2	5.39E-02	-4.93E-01	3.48E-02	5.01E-02	9.25E-02	3.06E-02	2.70E-01
K_3	1.73E-01	1.39E-01	7.73E-03	3.44E-02	7.45E-02	2.82E-02	1.68E-01
K_4	-5.08E-02	-5.27E-02	-1.33E-02	-4.52E-03	-3.12E-03	-8.97E-03	-1.07E-02
C_1	5.29E+05	9.83E+05	1.85E+05	5.73E+06	2.04E+05	7.90E+04	1.38E+07
R_1	2.96E-04	2.23E-05	3.27E-02	8.00E-04	6.77E-02	4.34E-02	8.25E-02
R_0	1.75E-03	7.03E-02	5.75E-01	2.99E-01	6.92E-01	4.24E-01	3.88E+00
η_i	9.50E-01	9.49E-01	9.48E-01	9.47E-01	9.36E-01	9.58E-01	9.48E-01
R_{SQ}	4.13	2.07	3.17	1.95	3.81	1.74	1.61

The final model being investigated that uses an OCV circuit component, the dual polarization model, has more constants to calibrate; thus, presumably should be the most accurate model.

Following the logic asserted in developing the dual polarization model, the two RC pairs each represent electrochemical processes occurring at different rates. Thus, the dual polarization model should better represent the interplay between current and voltage while current is changing. However, most of the battery data were taken at constant current so the model is parameterized without those dynamics. The parameterization results are shown in Table 12.

Table 12: Cell parameters and coefficient of determination for the DP and combined OCV-SOC.

	ANR M1B	NCR B	ICR B4	ICR C2	NCR A	LMN 2000	APR M1A
K_0	3.48E+00	3.45E+00	3.31E+00	3.40E+00	3.18E+00	3.34E+00	3.53E+00
K_1	-1.61E-04	-1.59E-04	1.48E-04	5.54E-05	-8.17E-05	1.09E-04	-7.20E-05
K_2	4.19E-01	-5.39E-01	-5.86E-01	-4.79E-01	-6.33E-01	-4.97E-01	2.85E-01
K_3	1.87E-01	1.34E-01	-1.00E-02	1.94E-03	5.27E-02	-7.73E-03	1.71E-01
K_4	-5.46E-02	-4.02E-02	-5.15E-02	-3.63E-02	3.14E-03	-5.12E-02	-1.85E-02
C_1	1.29E+01	1.68E+02	3.25E+07	6.65E+07	1.96E+06	1.00E+08	5.98E+07
R_1	7.17E-08	2.34E-07	6.38E-02	4.01E-02	5.09E-02	7.40E-01	4.42E-01

C_2	1.47E+02	2.22E+03	4.55E+08	2.40E+08	7.62E+07	8.29E+07	1.01E+08
R_2	7.17E-08	1.39E-07	4.80E-02	5.03E-02	4.87E-02	7.28E-01	4.26E-01
R_0	8.93E-03	7.05E-02	1.99E-01	1.58E-01	1.48E-01	1.90E-01	3.54E-01
η_i	9.51E-01	9.50E-01	9.50E-01	9.50E-01	9.49E-01	9.54E-01	9.53E-01
R_{SQ}	4.71	2.11	3.20	3.00	4.29	2.00	1.50

The R_{int} and combined model, parameterized through LLSR, only produced the best R_{SQ} result for the APR M1A cell. The Thévenin and combined models had the lowest R_{SQ} for the other six cells. Overall, the R_{SQ} for the R_{int} and combined model using LLSR for the APR M1A cell was the lowest across all models and cells. The coefficient of determination was generally larger when the coefficients were forced to be positive. There was some concern that the R_{SQ} value would favor cells with fewer data points since there would be fewer error points to sum.

However, this does not appear to be the case since the cells that were tested a greater number of times consistently have lower R_{SQ} and the cell tested the least number of times consistently has the highest R_{SQ} . The number of data points does not change between models, only different cells. Therefore, the number of data points should not impact comparisons between model results.

While the number of data points has a minimal impact, some aspect of the cell does have a considerable effect on the results since the order of cells with least to greatest R_{SQ} is identical across the three models with one exception: ICR C2 has the third least error for the Thévenin model while it has the fourth least in both of the other models. Parameters and associated R_{SQ} for each model and parameterization method are collected for each cell—this includes the positive coefficient models—and are displayed in the Appendix, starting with Table 14.

The accuracy of each model can be better appreciated through plotting the data and the model voltage prediction for the same load. For the ANR M1B cell, the R_{int} results are seen in Figure 74, the Thévenin results are in Figure 75, and the DP results are in Figure 76.

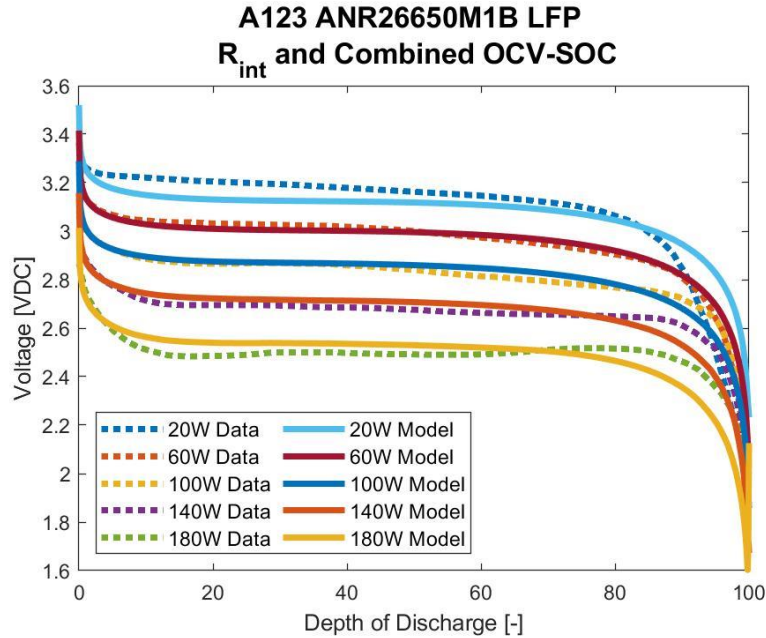


Figure 74: Battery data alongside R_{int} and combined OCV-SOC model results plot for the A123 M1B cell with an overall R_{SQ} of 4.71.

Despite the close approximation shown in Figure 74, the R_{int} model results in a larger error than the Thévenin model in Figure 75, which appears to have difficulty following the trend of the discharge curve. Both the R_{int} and DP models diverge from the data most significantly at the end of discharge, briefly exceeding one volt. There is a difference between R_{SQ} and the actual error of the model approximation; the coefficient of determination is more affected by larger errors than by small errors while the actual error is simply the difference between the data and the model. Since the error is squared as part of calculating R_{SQ} , two models with the same average error may have different R_{SQ} .

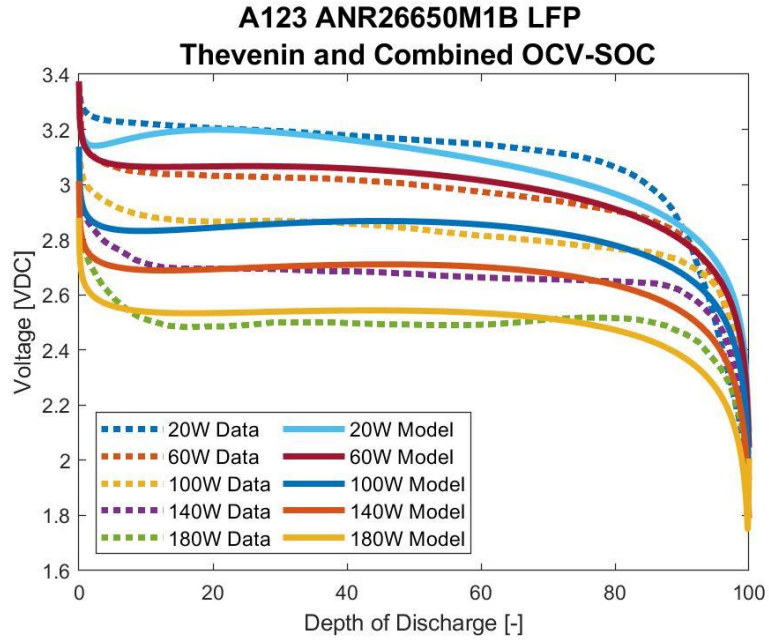


Figure 75: Battery data plotted alongside Thévenin and combined OCV-SOC model results for the A123 M1B cell with an overall R_{SQ} of 4.13.

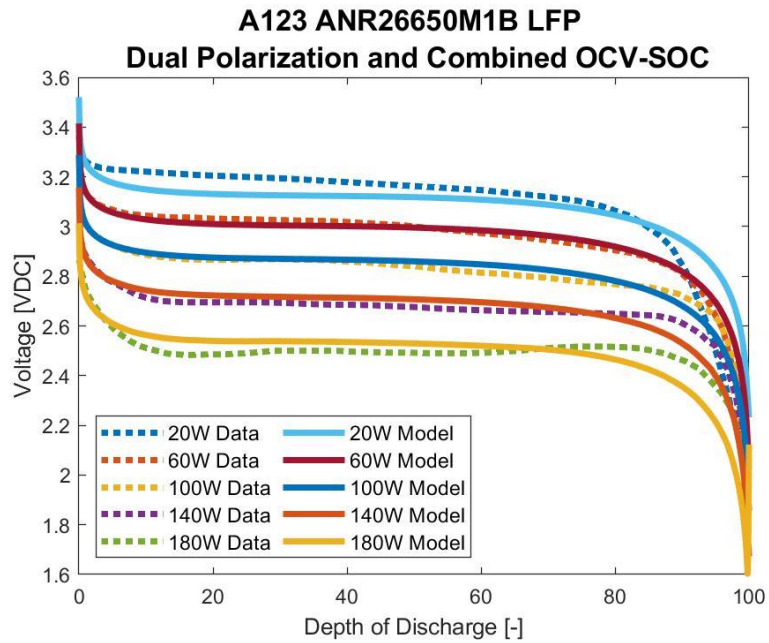


Figure 76: Dual polarization and combined OCV-SOC with an R_{SQ} of 4.71 for the A123 M1B cell.

Table 13: Total voltage error for each cell and model.

	ANR M1B	NCR B	ICR B4	ICR C2	NCR A	LMN 2000	APR M1A
R_{int}	203.3	96.5	218.5	180.6	298.5	124.3	105.4
Thévenin	209.9	96.2	220.4	115.6	252.9	102.8	106.5
DP	203.3	98.4	218.4	180.7	298.5	124.3	105.6

The distinction between error and R_{SQ} is important because the separate perspectives improve understanding of model performance. For instance, the voltage error for the ANR M1B cell in Table 13 shows that both the R_{int} and DP models have lower error than the Thévenin model, but, the R_{SQ} results are lowest for the Thévenin model. Average voltage error for the ANR M1B cell is slightly higher for the Thévenin model but its maximum voltage error is lower than the two other models. For the ANR M1B cell, the Thévenin model voltage error never exceeds one volt at any time but approaches it at both the beginning and end of discharge. In terms of R_{SQ} , results of the DP and combined model are slightly worse than the Thévenin and combined model. Besides ANR M1B results, the lowest R_{SQ} corresponds with lowest error for every model.

A commonality shared between all three models is that the largest errors tend to occur at the beginning and end of the discharge cycles. That is not to say that the models are always perfect during the majority of the discharge cycle. From all the cell discharge cycles, the Thévenin and combined OCV-SOC model has the lowest voltage error for just over 51% of the DOD. DP and combined OCV-SOC model provided the lowest voltage error for nearly 20% of the DOD. However, the DP and combined OCV-SOC model provided better results than the Thévenin model for just above 45% of the DOD.

Overall, the results appear to be contrary to findings in the literature, which suggest that the two polarization RC model is more accurate [66, 76]. In most cases, the DP model performed nearly as well as Thévenin model, and nearly identically to the R_{int} model. It seems unlikely that for all

seven batteries, the DP results are nearly identical to the R_{int} results by both error and R_{SQ} assessments. No changes were made to the methodology or optimization settings while parameterizing battery models. However, the upper and lower bounds may have prevented the process from finding a more suitable answer outside the bounds; alternatively, running the program from too few sets of initial randomized parameters may risk missing a global minimum R_{SQ} in favor of local minima. Each additional set of starting values increases the time spent determining parameters. While more time may improve the likelihood of finding a better solution, oftentimes large variations in starting parameters still reach the same result, this is a case of diminishing returns.

Moreover, adjustments are made to the lower and upper bounds once the program has determined a local minimum within the initial boundaries. Since there are no apparent precedents of the values and orders of magnitude of the combined OCV-SOC coefficients, the boundaries of the coefficients K_1, K_2, K_3 , and K_4 are adjusted whenever its resultant value is near a boundary. Simply, the bounds for the coefficients that are not emulating physically measurable battery behavior are re-centered on the updated coefficient value. However, the other parameters' bounds stay within reasonable values for the phenomena they represent; i.e., internal resistance should not exceed one $k\Omega$, which is an understatement considering cell internal resistance is frequently measured in $m\Omega$ [56, 88].

Increasing the number of sets random initial parameters might allow the iterative approach to find a lower error, but there are still different methods in the literature that may improve results. The accuracy of the results and capability of these models are likely reduced by not having OCV data available. In this application, the OCV-SOC relation must be discerned concomitantly with

the circuit parameters. Similarly, the approach of separating the parameterization task could be applied manually, provided the data is similar to HPPC so the transient voltages are apparent.

Presuming that the parameterization methods are functioning appropriately, then the next aspect to question is the capability of the data to inform the model. Without dynamic battery discharge data for comparison and for model characterization, it is unknown whether this is an issue regarding the model, the parameterization method, or insufficient data. Though an ECM is supposed to be more capable of imitating battery charge and discharge behavior, the model still relies on proper parameters to make approximations. When the data used to inform the model does not demonstrate transient behavior, the ECM is unlikely to show that behavior.

4.6 Conclusion

While battery models each have relatively good approximations of the battery data, there are several ECMs and parameterization methods that have not yet been attempted that might yield better results. Several variations and extensions exist for the ECMs hence covered, some of which involve variable parameters, temperature, voltage hysteresis, and states beyond SOC. Besides alternative models, it warrants investigating if parameterization using HPPC data leads to the same results as the constant current discharge for the same cells. Parameters cannot necessarily be linked to physical attributes of the cell, thereby evincing the heuristic nature of ECMs. Parameters that should be similar between cells of the same active chemistry differ, which is manageable, but does not permit using the model to represent another similar cell.

For many applications, coulomb counting as a means of determining state of charge is sufficiently accurate, provided the conditions are met. Coulomb counting is more reliable for LFP batteries than OCV-SOC relationships because the cell voltage remains nearly constant for

much of the charge and discharge cycle. Hence, error in voltage measurements will result in even greater SOC inaccuracies. However, the combination of the two methods, presuming utilizing an accurate model, will provide the best results since one has to verify with the other.

Several ECMs were parameterized to simulate the behavior of a corresponding battery for a variety of discharge rates. Resultant models predict state of charge and terminal voltage based on discharge current, once parameterized. Since the load remains constant across the entire discharge, it is likely that time-dependent behaviors will not be adequately represented by in the models. However, for that same reason these data can demonstrate the need for dynamic discharge profiles when testing.

5 Conclusion

Battery technology has been evolving to meet ever more stringent demands for broader applications. Despite large improvements in battery technology, EVs still lag ICEVs in range and convenience. However, efforts to reduce emissions, or at least displace them from population centers, remain steadfast. Increased battery performance in EVs involves simultaneously increasing charge storage while decreasing the volume and mass of the storage device. Meanwhile, there have been efforts to palliate range anxiety—often through increasing charging speed and expanding the network of vehicle chargers. However, an alternative via incorporating a swappable battery pack is explored in chapter two. The subject vehicle, a 2007 GEM eS, was converted from lead-acid batteries to LFP cells to reduce vehicle weight; thereby, reducing the energy needed to drive the vehicle. Concomitantly, the battery pack is light enough for two persons to remove it from the vehicle, whereby enabling the quick removal of an exhausted battery pack with a fully charged battery pack so that the vehicle can resume use. Chapter 2 documents the vehicle modifications facilitating the swappable battery pack concept, including construction of the 40 Ah battery pack and the initial interface between the GEM and battery support electronics.

The second round of modifications is prompted after the GEM is returned with many of the 40 Ah cells no longer functioning. Combined with testimony, the potential cause of damage is determined. A new battery pack with greater storage capacity (60 Ah) was constructed to replace the 40 Ah battery pack. Unfortunately, even after the battery pack was replaced and the BMS reprogrammed to prevent the probable cause of the first issue, the vehicle would no longer drive.

Many different possible causes for the error are examined and the actions taken to resolve the issue are described. Items that were not functioning according to the manual—which was provided with the vehicle—were replaced or repaired. There were significant delays and setbacks because information regarding the vehicle was scarce: the 2007 GEM eS was manufactured for a company which no longer owned the brand, the vehicle had never been especially popular, the current company carrying the brand had discontinued service for that year, and there were no licensed technicians within the state of Kansas. Furthermore, information provided from online resources, while similar to the aforementioned manual, had discrepancies with the manual. Since there was little documentation of the wiring changes to the GEM in the first round of modifications and during the period when being used by the Center for Sustainability, wiring inconsistencies with the manual and between other resources were frequent. Though the vehicle will not drive, all accessory systems are functional. Additionally, the battery charger and the BMS controls work, at least in laboratory conditions. Since the vehicle was not capable of driving, the BMS controls and settings primarily focus on maintaining the battery pack.

Battery management practices result from understanding how batteries function, both electrically and chemically. Chapter 3 begins with a cursory explanation of battery composition and functionality before moving onto how batteries break down. The difference in electrical potential of the anodes, which drives current through an external circuit, also increases the favorability of side reactions. One result of side reactions, the SEI, is helpful to some extent as it slows down electrode decomposition. However, SEI growth reduces the capacity of the cell. Other reactions may produce flammable gases. The likelihood of certain undesirable behaviors occurring are

temperature dependent but can be mitigated to some extent by binding materials in the electrodes and the electrolyte composition. Once manufactured, the cell's longevity is primarily dependent on the conditions of use. Besides preventing physical and electrical damage to the cell, battery management seeks to minimize the harm to a cell by regulating cell voltage limits and voltage differences between cells, charge and discharge current, and cell temperature. While cell voltage, external temperature, and current are measurable, several other useful indicators such as SOC and SOH must be approximated. Chapter 4 expounds on the purpose of such indicators and methods of determining these values.

Specifically, Chapter 4 details battery models; which are employed to estimate battery states while the battery is use because they are simpler to implement and do not interrupt using the battery. Since lumped-parameter models are not necessarily directly linked to actual battery processes, they will never attain the degree of accuracy required when designing new batteries based on model results. However, these battery models are capable of reasonable accuracy for battery management, electric vehicle models, and other applications for a specific battery. By utilizing numerous battery models and repeated tests across various temperatures, battery chemistries, etc. ideally these battery models will reveal general trends. Such trends would allow battery behavior to be approximated based on more readily available data and battery attributes.

While the results of the battery model parameterization demonstrate a relatively good approximation, there are problematic regions where the error is excessive which require alternative methods of state determination to improve results. Realization of generalities would be improved by a more robust and automated testing and parameterization procedure that can more quickly assess more batteries and battery models. Future battery modeling efforts would be

improved with the additions of the other battery states that were mentioned, beyond SOC. SOH in cells becomes increasingly important with the growing emphasis on sustainability but also as more powerful and longer lasting cells are introduced. Generally, as cells can store more energy, more caution should be rendered to avoid harm. Though sustainability has not overtaken economic concerns in engineering, considerations of environmental impact are becoming more common. In that regard, simply replacing batteries is less favorable; thus, there is more concern towards maintaining cells. Specifically, ensuring longer cycle lives of cells must emphasize avoiding critical sources of damage and minimizing damage altogether.

Appendix

Supplementary Material for Chapter 2

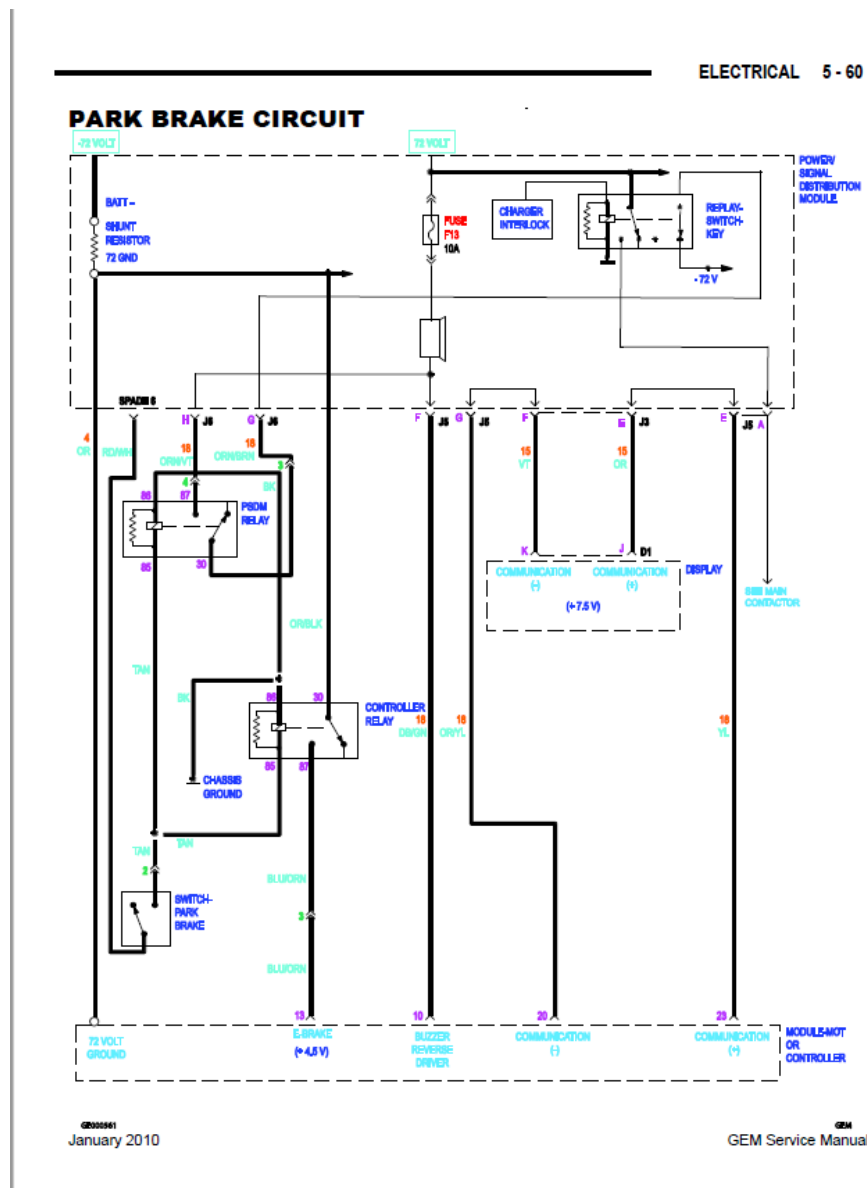


Figure 77: Parking brake circuit diagram in the 2010 GEM Service Manual that better matches the GEM parking brake wiring than the service manual donated by KU Facilities Services.

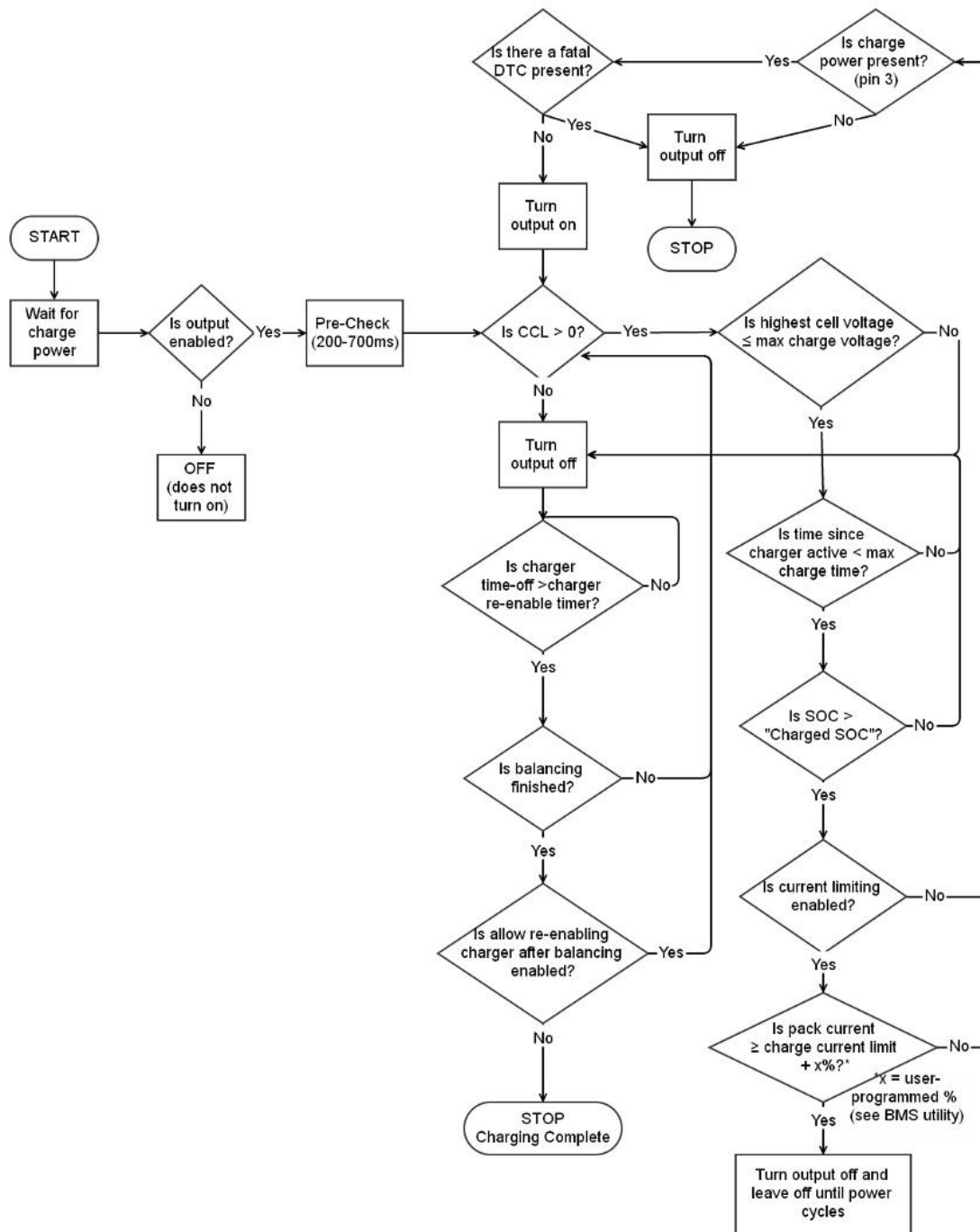


Figure 78: “Charger Safety Functional Flowchart” provided in the Orion BMS Utility Manual [29]. These are the steps taken to determine if the Charger Safety relay is engaged or disengaged.

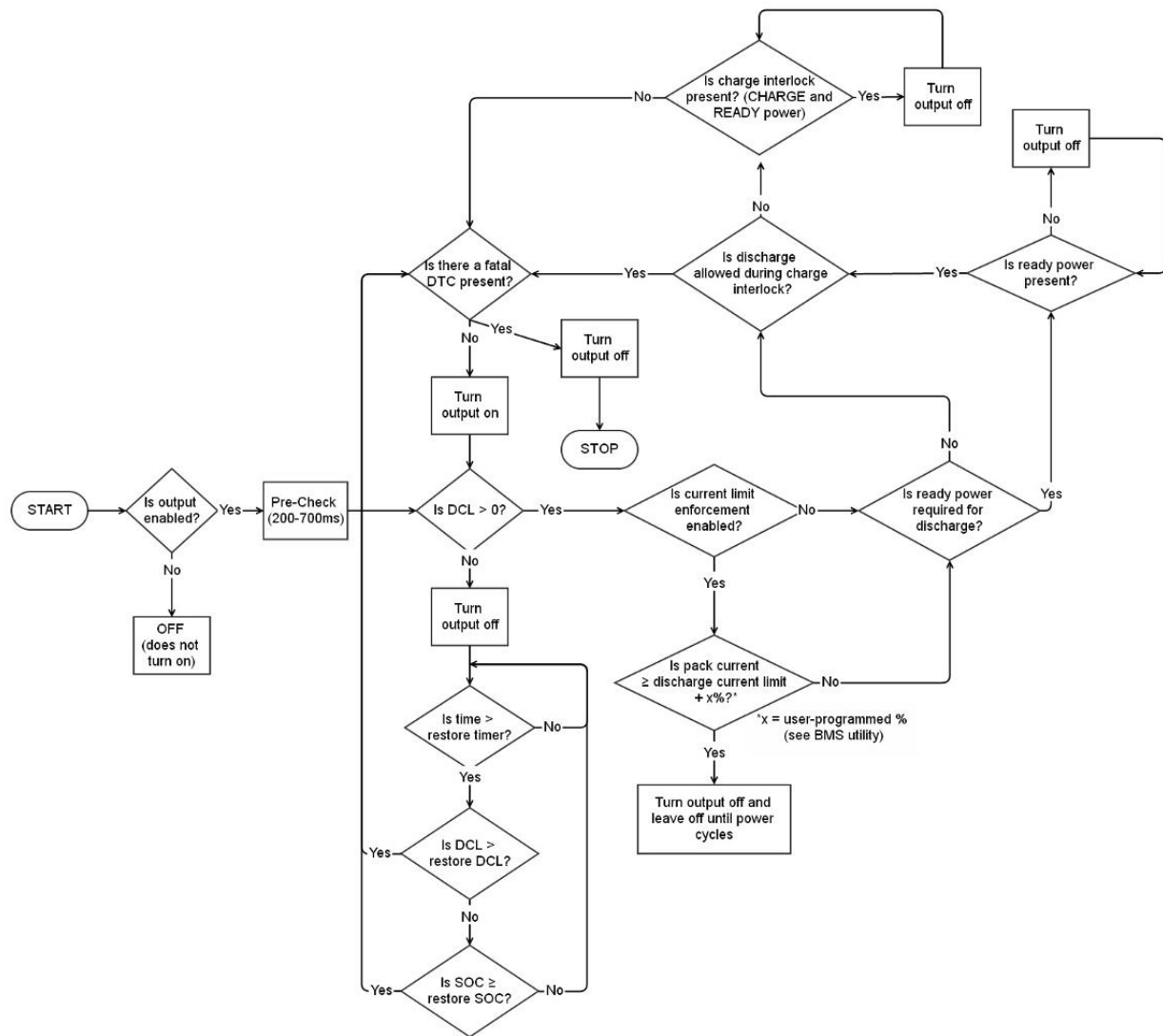


Figure 79: “Discharge Enable Functional Flowchart” outlining the conditions that determine whether the BMS allows discharge [29].

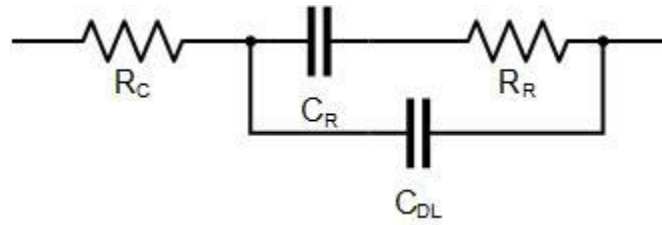


Figure 80: Original Randles equivalent circuit battery model representing electrode reactions. Resistance and capacitance of the electrode reaction are R_R and C_R , respectively. Resistance of the electrolyte is R_C and capacitance of double layer effect at the electrode surface is C_{DL} [80].

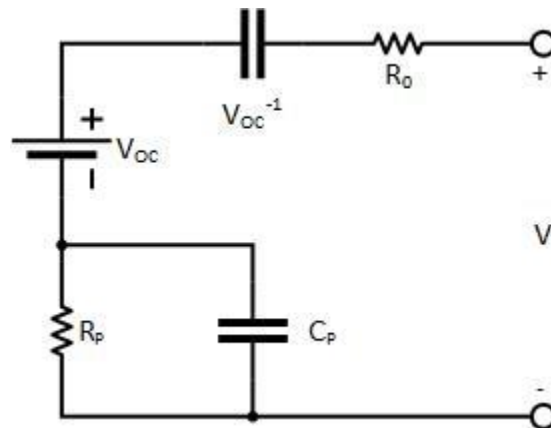


Figure 81 Equivalent circuit model utilized by the Partnership for a New Generation of Vehicles (PNGV) to predict terminal voltage [89]. Model parameters are to be found through Hybrid Pulse Power Characterization (HPPC) tests. The RC pair models polarizations, hence the subscripts.

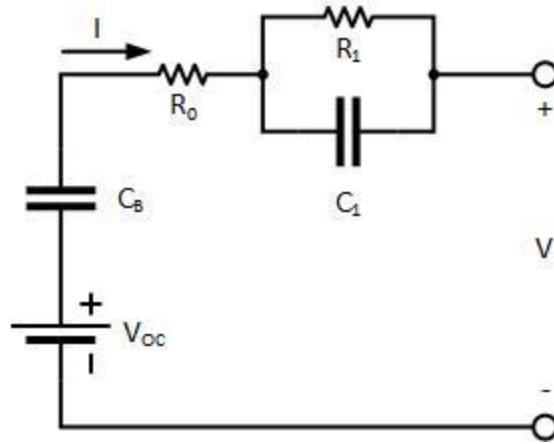


Figure 82 One variation of the PNGV ECM. The RC pair and other circuit components are in a different order compared to the original PNGV EMC in Figure 81 [83, 90].

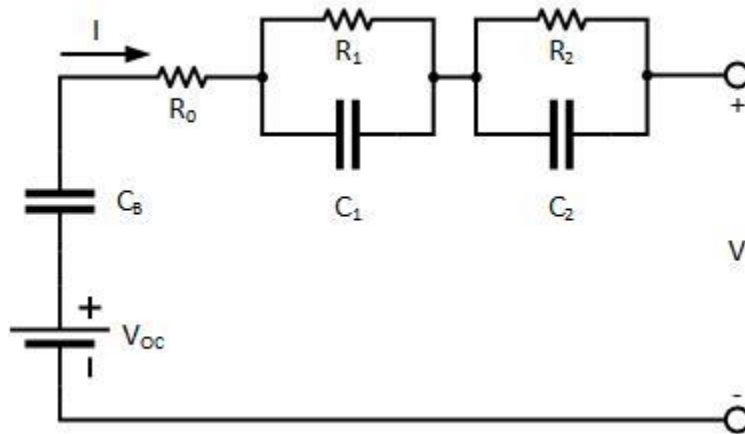


Figure 83 This equivalent circuit model is named the General Non-Linear (GNL) model or otherwise known as an improved PNGV model [90, 91].

Table 14: Calibration results for the ANR M1B cell. The notation in the second row indicates if the parameters were constrained to be positive or if positive and negative values were allowed.

	Dual Polarization		Thévenin		R _{int} fmincon		R _{int} LLSR
	+	±	+	±	+	±	±
K_0	3.419E+00	3.475E+00	3.402E+00	3.256E+00	3.353E+00	3.475E+00	3.467E+00
K_1	1.216E-07	-1.614E-04	5.401E-07	-1.135E-04	2.484E-07	-1.619E-04	-6.872E-05
K_2	2.175E-01	4.189E-01	2.059E-01	5.391E-02	1.412E-01	4.194E-01	4.083E-01
K_3	1.562E-01	1.866E-01	1.622E-01	1.726E-01	1.465E-01	1.867E-01	1.831E-01
K_4	1.975E-04	-5.462E-02	1.032E-04	-5.080E-02	2.569E-06	-5.467E-02	-5.403E-02
C_2	2.797E+05	1.293E+01	4.418E+02	5.295E+05			
R_2	2.714E-01	7.171E-08	9.057E-03	2.962E-04			
C_1	5.510E+02	1.470E+02					
R_1	5.400E-03	7.169E-08					
R_0	3.684E-03	8.929E-03	6.082E-05	1.749E-03	8.941E-03	8.929E-03	8.927E-03
η_i	9.442E-01	9.506E-01	9.541E-01	9.502E-01	9.495E-01	9.487E-01	
R_{SQ}	4.9399	4.7108	4.8282	4.1300	5.1423	4.7108	4.7407

References

1. Bahree, M. *India Goes Electric With Battery-Swapping Rickshaws*. 2019.
2. Service, P.B. *Timeline: History of the Electric Car*. 2009.
3. Egbue, O. and S. Long, *Barriers to widespread adoption of electric vehicles: An analysis of consumer attitudes and perceptions*. *Energy Policy*, 2012. **48**: p. 717-729.
4. Energy, D.o. *EV Everywhere Grand Challenge Blueprint*. 2013.
5. Budde Christensen, T., P. Wells, and L. Cipcigan, *Can innovative business models overcome resistance to electric vehicles? Better Place and battery electric cars in Denmark*. *Energy Policy*, 2012. **48**: p. 498-505.
6. Hausmann, A.J., *Advances in Electric Drive Vehicle Modeling with Subsequent Experimentation and Analysis*. 2012, University of Kansas: Ann Arbor. p. 171.
7. Collins, P.G., *Second Generation Electric Vehicle Development at the University of Kansas*, C. Depcik, B. Yimer, and H. Fang, Editors. 2015, University of Kansas.
8. Polaris Industries, I. *GEM History*. 2018; Available from: <https://gem.polaris.com/en-us/history/>.
9. Standards, F.M.V.S., *Federal Register Volume 63, Issue 116 (June 17, 1998)*, in *Federal Register Vol. 63, No. 116*, D. National Highway Safety Administration, Editor. 1998, Office of the Federal Register, National Archives and Records Administration: Federal Register. p. 24.
10. Applications, E.T., *2005 Global Electric Motorcars eS Short Bed Utility*, in *NEV America: US DOE Advanced Vehicle Testing Activity*. 2005: Idaho National Laboratories: Advanced Vehicles Library.
11. Global Electric Motorcars, L., *GEM Owner's Manual*. 2006: DaimlerChrysler. 118.
12. Global Electric Motorcars, L., *2007 Model Year Parts Catalog*. 2007, DaimlerChrysler Company.
13. Company, G.E., *Separately Excited (SX) Transistorized Motor Controllers for Neighborhood Electric Vehicle Applications Installation and Operation Manual GE Model IC3645SR7A353T3*. Installation and Operation Manual. 2003, GE Technical Manuals, Flight Systems Industrial Products. 35.
14. Choate, M., et al., *A Swappable Battery Pack for Short-Range Electric Vehicles*. 2014(46613): p. V012T15A009.

15. Reddy, T.B., *Linden's Handbook of Batteries, Fourth Edition*. 4 ed. 2011: McGraw-Hill Education.
16. University, B. *BU-301a: Types of Battery Cells*. Packaging and Safety, 2017.
17. Nitta, N., et al., *Li-ion battery materials: present and future*. *Materials Today*, 2015. **18**(5): p. 252-264.
18. Doughty, D.H., *A General Discussion of Li Ion Battery Safety*. The Electrochemical Society interface, 2012. **21**(2): p. 37-44.
19. Depcik, C., *Vehicle Modeling*, in *Hybrid and Electric Vehicles*. 2016.
20. L. E. Unnewehr, S.A.N., *Electric Vehicle Technology*. 1982: John Wiley & Sons, Inc.
21. Vetter, J., et al., *Ageing mechanisms in lithium-ion batteries*. *Journal of Power Sources*, 2005. **147**(1): p. 269-281.
22. Global Electric Motorcars, L., *Service Manual*. 2007: DaimlerChrysler. 142.
23. Co., C.A.L.B., *Product User Manual*, C.A.L.B. Co., Editor.: <http://www.calbusainc.com/additional-information/>.
24. Omar, N., et al., *Rechargeable Energy Storage Systems for Plug-in Hybrid Electric Vehicles—Assessment of Electrical Characteristics*. *Energies*, 2012. **5**(8).
25. Andrea, D., *Battery Management Systems for Large Lithium Ion Battery Packs*. 2010, Norwood, UNITED STATES: Artech House.
26. Tanim, T.R., et al. *The implications of fast charge in lithium ion battery performance and life: cell vs. pack*. 2018. United States.
27. Frieske, B., M. Kloetzke, and F. Mauser. *Trends in vehicle concept and key technology development for hybrid and battery electric vehicles*. in *2013 World Electric Vehicle Symposium and Exhibition (EVS27)*. 2013.
28. Applications, E.V., *2005 Global Electric Motorcars e2 2-Passenger*, in *NEV America: US DOE Advanced Vehicle Testing Activity*. 2005: Idaho National Laboratory: Advanced Vehicles Library.
29. BMS, O., *Wiring and Installation Manual*. 4.1 ed. 2018: Ewert Energy Systems, Inc.
30. Corp., D.-Q.T., *QuiQ Charger - GEM Product Manual*, D.-Q.T. Corp., Editor. 2014.
31. Max, *Specification of LiFePO4 Prismatic Module: 3.2V 60 Ah*, A.P.P. Corp., Editor. 09/20/2010: <http://www.batteryspace.com>.

32. Lu, L., et al., *A review on the key issues for lithium-ion battery management in electric vehicles*. Journal of Power Sources, 2013. **226**: p. 272-288.
33. Global Electric Motorcars, L., *Park Brake Circuit*. 2010, Polaris GEM: GEM Service Manual.
34. www.recom-power.com, *RP20-FR Series Datasheet*, in *RECOM DC/DC Converter*, RECOM, Editor. 2017: digikey.com.
35. Crydom, *I-DC Series*, in *Panel Mount 4th Generation*, Crydom, Editor. 2017: digikey.com.
36. Wang, S., et al., *Aluminum Chloride-Graphite Batteries with Flexible Current Collectors Prepared from Earth-Abundant Elements*. Advanced Science, 2018. **5**(4): p. 1700712.
37. Cheruvally, G., *Lithium Iron Phosphate : A Promising Cathode-Active Material for Lithium Secondary Batteries*. 2008, Zurich, SWITZERLAND: Trans Tech Publications, Limited.
38. Chen, Z., et al., *Titanium-Based Anode Materials for Safe Lithium-Ion Batteries*. Advanced Functional Materials, 2013. **23**(8): p. 959-969.
39. Wang, Q., et al., *Thermal Behavior of Lithiated Graphite with Electrolyte in Lithium-Ion Batteries*. Journal of The Electrochemical Society, 2006. **153**(2): p. A329-A333.
40. Arora, P., R.E. White, and M. Doyle, *Capacity Fade Mechanisms and Side Reactions in Lithium-Ion Batteries*. Journal of The Electrochemical Society, 1998. **145**(10): p. 3647-3667.
41. Ren, D., et al., *Investigation of Lithium Plating-Stripping Process in Li-Ion Batteries at Low Temperature Using an Electrochemical Model*. Journal of The Electrochemical Society, 2018. **165**(10): p. A2167-A2178.
42. Uhlmann, C., et al., *In situ detection of lithium metal plating on graphite in experimental cells*. Journal of Power Sources, 2015. **279**: p. 428-438.
43. Lin, H.p., et al., *Low-Temperature Behavior of Li-Ion Cells*. Electrochemical and Solid-State Letters, 2001. **4**(6): p. A71-A73.
44. Liu, Q., et al., *Understanding undesirable anode lithium plating issues in lithium-ion batteries*. RSC Advances, 2016. **6**(91): p. 88683-88700.
45. Zhan, C., et al., *Dissolution, migration, and deposition of transition metal ions in Li-ion batteries exemplified by Mn-based cathodes – a critical review*. Energy & Environmental Science, 2018. **11**(2): p. 243-257.

46. Li, J., et al., *Unravelling the Impact of Reaction Paths on Mechanical Degradation of Intercalation Cathodes for Lithium-Ion Batteries*. Journal of the American Chemical Society, 2015. **137**(43): p. 13732-13735.
47. He, H., et al., *Failure Investigation of LiFePO₄ Cells in Over-Discharge Conditions*. Journal of The Electrochemical Society, 2013. **160**(6): p. A793-A804.
48. BMS, O., *Orion BMS (Original) Software Utility*. Ewert Energy Systems: Orion BMS Software Downloads.
49. Waag, W., C. Fleischer, and D.U. Sauer, *Critical review of the methods for monitoring of lithium-ion batteries in electric and hybrid vehicles*. Journal of Power Sources, 2014. **258**: p. 321-339.
50. Xia, B., et al., *Accurate Lithium-ion battery parameter estimation with continuous-time system identification methods*. Applied Energy, 2016. **179**(Supplement C): p. 426-436.
51. Plett, G.L., *Extended Kalman filtering for battery management systems of LiPB-based HEV battery packs: Part 2. Modeling and identification*. Journal of Power Sources, 2004. **134**(2): p. 262-276.
52. Christophersen, J.P., *Battery Test Manual For Electric Vehicles, Revision 3*. 2015: United States.
53. Tippmann, S., et al., *Low-temperature charging of lithium-ion cells part I: Electrochemical modeling and experimental investigation of degradation behavior*. Journal of Power Sources, 2014. **252**: p. 305-316.
54. Yi, J., et al., *Modeling the temperature dependence of the discharge behavior of a lithium-ion battery in low environmental temperature*. Journal of Power Sources, 2013. **244**: p. 143-148.
55. Energy, S., *Panasonic NCR18650B*, Panasonic, Editor. 2012.
56. Zhu, X. and G. Shibin. *State of charge estimation based on improved LiFePO₄ battery model and Kalman filtering*. in *2016 IEEE 8th International Power Electronics and Motion Control Conference (IPEMC-ECCE Asia)*. 2016.
57. Eichi, H.R. and M. Chow. *Modeling and analysis of battery hysteresis effects*. in *2012 IEEE Energy Conversion Congress and Exposition (ECCE)*. 2012.
58. Srinivasan, V., J.W. Weidner, and J. Newman, *Hysteresis during Cycling of Nickel Hydroxide Active Material*. Journal of The Electrochemical Society, 2001. **148**(9): p. A969-A980.

59. Gerschler, J. and D. Sauer, *Investigation of open-circuit-voltage behaviour of lithium-ion batteries with various cathode materials under special consideration of voltage equalisation phenomena*. Vol. 3. 2009. 1550-1563.
60. Roscher, M.A., O. Bohlen, and J. Vetter, *OCV Hysteresis in Li-Ion Batteries including Two-Phase Transition Materials*. International Journal of Electrochemistry, 2011. **2011**.
61. Rahimi-Eichi, H., et al., *Battery Management System: An Overview of Its Application in the Smart Grid and Electric Vehicles*. IEEE Industrial Electronics Magazine, 2013. **7**(2): p. 4-16.
62. Birkel, C. and D. Howey. *Model identification and parameter estimation for LiFePO₄ batteries*. in *IET Hybrid and Electric Vehicles Conference 2013 (HEVC 2013)*. 2013.
63. Dai, H., B. Jiang, and X. Wei, *Impedance Characterization and Modeling of Lithium-Ion Batteries Considering the Internal Temperature Gradient*. Energies, 2018. **11**(1).
64. Tröltzsch, U., O. Kanoun, and H.-R. Tränkler, *Characterizing aging effects of lithium ion batteries by impedance spectroscopy*. Electrochimica Acta, 2006. **51**(8): p. 1664-1672.
65. Huria, T., G. Ludovici, and G. Lutzemberger, *State of charge estimation of high power lithium iron phosphate cells*. Journal of Power Sources, 2014. **249**: p. 92-102.
66. Nejad, S., D.T. Gladwin, and D.A. Stone, *A systematic review of lumped-parameter equivalent circuit models for real-time estimation of lithium-ion battery states*. Journal of Power Sources, 2016. **316**(Supplement C): p. 183-196.
67. Ramadesigan, V., et al., *Modeling and Simulation of Lithium-Ion Batteries from a Systems Engineering Perspective*. Journal of The Electrochemical Society, 2012. **159**(3): p. R31-R45.
68. Hausmann, A. and C. Depcik, *Expanding the Peukert equation for battery capacity modeling through inclusion of a temperature dependency*. Journal of Power Sources, 2013. **235**: p. 148-158.
69. O'Malley, R., L. Liu, and C. Depcik, *Comparative study of various cathodes for lithium ion batteries using an enhanced Peukert capacity model*. Journal of Power Sources, 2018. **396**: p. 621-631.
70. Chang, W.-Y., *The State of Charge Estimating Methods for Battery: A Review*. ISRN Applied Mathematics, 2013. **2013**: p. 7.
71. Marongiu, A., et al., *Comprehensive study of the influence of aging on the hysteresis behavior of a lithium iron phosphate cathode-based lithium ion battery – An experimental investigation of the hysteresis*. Applied Energy, 2016. **171**: p. 629-645.

72. Shepherd, C.M., *Design of Primary and Secondary Cells: II . An Equation Describing Battery Discharge*. Journal of The Electrochemical Society, 1965. **112**(7): p. 657-664.
73. Hu, X., S. Li, and H. Peng, *A comparative study of equivalent circuit models for Li-ion batteries*. Journal of Power Sources, 2012. **198**(Supplement C): p. 359-367.
74. Pattipati, B., et al., *Open circuit voltage characterization of lithium-ion batteries*. Journal of Power Sources, 2014. **269**: p. 317-333.
75. Plett, G.L., *Extended Kalman filtering for battery management systems of LiPB-based HEV battery packs: Part 3. State and parameter estimation*. Journal of Power Sources, 2004. **134**(2): p. 277-292.
76. Jackey, R., et al., *Battery Model Parameter Estimation Using a Layered Technique: An Example Using a Lithium Iron Phosphate Cell*. 2013, SAE International.
77. Alavi, S.M.M., C.R. Birkl, and D.A. Howey, *Time-domain fitting of battery electrochemical impedance models*. Journal of Power Sources, 2015. **288**(Supplement C): p. 345-352.
78. Johnson, V.H., A.A. Pesaran, and T. Sack. *Temperature-Dependent Battery Models for High-Power Lithium-Ion Batteries*. 2001. United States.
79. Alavi, S.M.M., et al., *Identifiability of Generalized Randles Circuit Models*. IEEE Transactions on Control Systems Technology, 2017. **25**(6): p. 2112-2120.
80. Randles, J.E.B., *Kinetics of rapid electrode reactions*. Discussions of the Faraday Society, 1947. **1**(0): p. 11-19.
81. Zheng, Y., et al., *Effects of state of charge on the degradation of LiFePO₄/graphite batteries during accelerated storage test*. Journal of Alloys and Compounds, 2015. **639**(Supplement C): p. 406-414.
82. Liao, X., J. Yu, and L. Gao, *Electrochemical study on lithium iron phosphate/hard carbon lithium-ion batteries*. Journal of Solid State Electrochemistry, 2012. **16**(2): p. 423-428.
83. He, H., R. Xiong, and J. Fan, *Evaluation of Lithium-Ion Battery Equivalent Circuit Models for State of Charge Estimation by an Experimental Approach*. Energies, 2011. **4**(4).
84. Mousavi G, S.M. and M. Nikdel, *Various battery models for various simulation studies and applications*. Renewable and Sustainable Energy Reviews, 2014. **32**: p. 477-485.
85. Valerie H. Johnson, A.A.P., Thomas Sack, *Temperature-Dependent Battery Models for High-Power Lithium-Ion Batteries*, in *Annual Electric Vehicle Symposium*. 2001, National Renewable Energy Laboratory: Montreal, Canada.

86. Feng, F., et al., *Online Estimation of Model Parameters and State of Charge of LiFePO₄ Batteries Using a Novel Open-Circuit Voltage at Various Ambient Temperatures*. Energies, 2015. **8**(4).
87. Tao, L., et al., *A review of stochastic battery models and health management*. Renewable and Sustainable Energy Reviews, 2017. **80**(Supplement C): p. 716-732.
88. Barsoukov, E., et al., *Universal battery parameterization to yield a non-linear equivalent circuit valid for battery simulation at arbitrary load*. Journal of Power Sources, 1999. **83**(1): p. 61-70.
89. None, *PNGV battery test manual*. 1997: United States.
90. Meng, J., et al., *Overview of Lithium-Ion Battery Modeling Methods for State-of-Charge Estimation in Electrical Vehicles*. Applied Sciences, 2018. **8**(5).
91. Feng Jin, H.Y., Wang Guofu, *Comparison Study of Equivalent Circuit Model of Li-Ion Battery for Electric Vehicles*. Research Journal of Applied Sciences, Engineering, and Technology, 2013. **6**(20): p. 3756-3759.